



Università degli Studi di Cagliari

## **DOTTORATO DI RICERCA**

Scienze e Tecnologie Chimiche

Ciclo XXIII

### **TITOLO TESI**

Redox Switchable Chromophores based on Metal (Ni, Pd, Pt) Mixed-Ligand Dithiolene Complexes Showing Molecular Second-order NLO Activity

Settore/i scientifico disciplinari di afferenza

CHIM/03

Presentata da:	Davide Espa
Coordinatore Dottorato	Prof. Mariano Casu
Tutor	Prof.essa Paola Deplano

Esame finale anno accademico 2009 – 2010



---

## Table of Contents

Chart 1	II
Chapter 1	
Introduction	
1.1 Introduction	2
1.2 Aim of the work	4
Chapter 2	
Background	
2.1 Dithiolene Ligands and d8 Metal Dithiolene Complexes	8
2.2.1 Symmetric complexes	12
2.2.2 Asymmetric complexes	13
2.2 $d^8$ Metal Diimine Dithiolato Complexes	14
Chapter 3	
Experimentals methods	
3.1 Introduction	18
3.2 M(R <sub>2</sub> pipdt)(L') synthesis and characterisation	23
3.2.1 Synthesis	23

## Table of Contents

---

3.3 [M(R <sub>2</sub> pipdt)(dmit)] (M(II) = Ni, Pd, Pt)	25
3.3.1 Structural characterization	25
3.3.2 Vibrational Spectroscopy	30
3.3.3 Electrochemistry	32
3.3.4 Structural characterization of [Pt(Bz <sub>2</sub> pipdt)(dcbdt)]	34
3.4 [M(L)(mnt)] synthesis and characterisation	37
3.4.1 Synthesis of [M(Bz <sub>2</sub> pipdt)(mnt)] (M(II) = Ni, Pd, Pt)	37
3.4.2 Structural characterization	38
3.4.3 Synthesis of [M(Et <sub>2</sub> dazdt)(mnt)] (M(II) = Ni, Pd, Pt)	46
3.4.4 Structural characterization	47
3.4.5 Electrochemistry	53
3.5 Experimental details	55

## Chapter 4

### Optical Properties

4.1 Introduction to second-order NLO materials	62
4.1.2 Techniques for measuring SHG in molecular materials	66
4.2 Optical studies	68
4.3 Spectroelectrochemistry	84

## Chapter 5

### Perspectives

5.1 Introduction	90
5.2 Synthesis	92

---

5.2.1 Structural characterisation	93
5.2.2 Coordination ability of Me <sub>2</sub> pipto	97
5.3 Synthesis of [M(R <sub>2</sub> pipdt)(dsit)] (M=Pd, Pt; R= Bz, <sup>i</sup> Pr)	100
5.3.1 Structural characterization of [Pt(Bz <sub>2</sub> pipdt)(dsit)]	100
5.4 Experimental Details	104

## Chapter 6

### Conclusions

7.1 Conclusions	109
-----------------	-----

### Appendices

A.1 Vibrational spectra of M(Bz <sub>2</sub> pipdt)(dmit)	116
A.2 Crystallographic data for [Pt(Bz <sub>2</sub> pipdt)(dcbdt)]	117
A.3 Crystallographic data for [Pt(Et <sub>2</sub> dazdt) <sub>2</sub> ][Pt(mnt) <sub>2</sub> ]	118
A.4 Schematic diagram of the setup for an EFISH experiment	120
A.5 Solvatochromic studies	121
A.6 DFT calculation for [M(Bz <sub>2</sub> pipdt)(mnt)] (M = Ni, Pd, Pt)	123
A.7 Optically Transparent Thin-Layer Cell (OTTLE)	131
A.8 Coordination ability of Me <sub>2</sub> pipto with Fe ion	135
A.9 Photoluminescence studies	143

Bibliography	146
--------------	-----

*Table of Contents*

---

List of publications

Acknowledgement

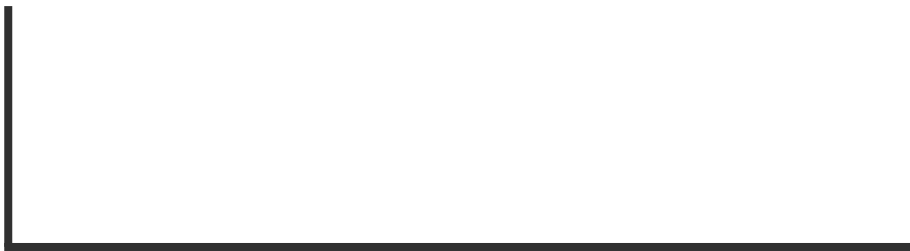




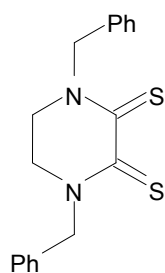




*Chart 1*



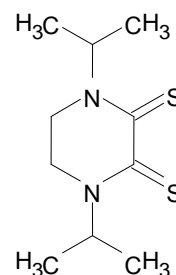
Structures with acronymus of  $d^8$  metal mixed-ligand dithiolene complexes synthesized for studies under discussion in this thesis.



Bz<sub>2</sub>pipdt

1,4-dibenzyl-piperazine-  
3,2-dithione

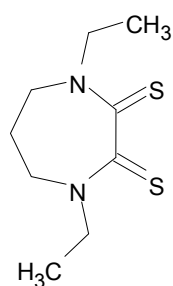
(1a)



iPr<sub>2</sub>pipdt

1,4-diisopropyl-piperazine-  
3,2-dithione

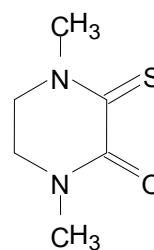
(1b)



Et<sub>2</sub>dazdt

1,4 -dimethyl-perhydrodiazepine-2,3-  
dithione

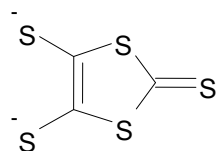
(1c)



Me<sub>2</sub>pipto

1,4-dimethyl-piperazine-3-oxo-2-  
thione

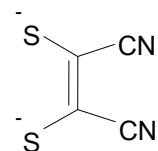
(1d)



dmit

2-thioxo-1,3-dithiole-4,5-dithiolato

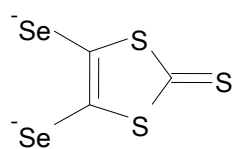
(1e)



mnt

maleonitriledithiolato

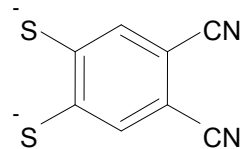
(1f)



dsit

2-thioxo-1,3-dithiole-4,5-diselenolato

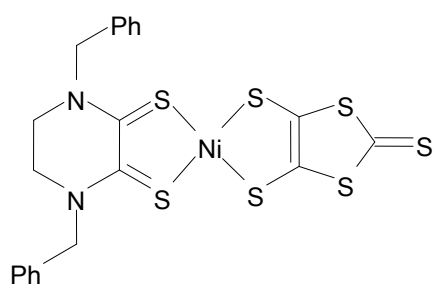
(1g)



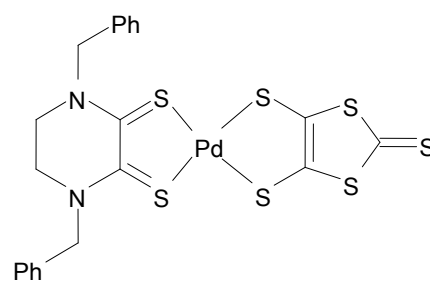
dcbdt

4,5-dicyanobenzene-1,2-dithiolato

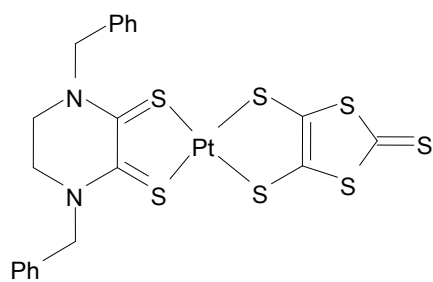
(1h)



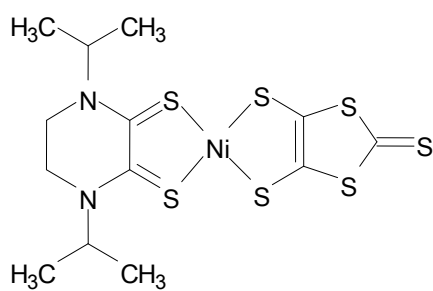
[Ni(Bz<sub>2</sub>pipdt)(dmit)] (2a)



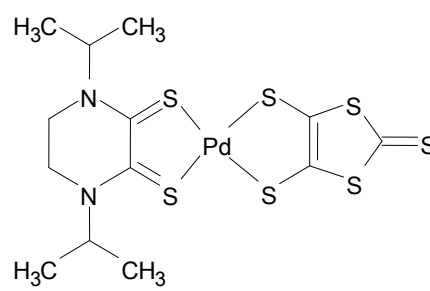
[Pd(Bz<sub>2</sub>pipdt)(dmit)] (2b)



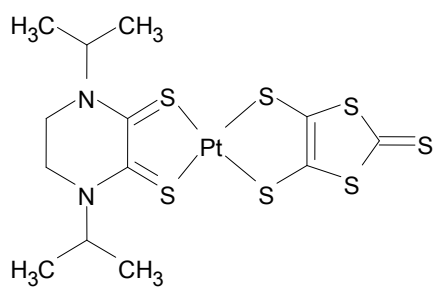
[Pt(Bz<sub>2</sub>pipdt)(dmit)] (**2c**)



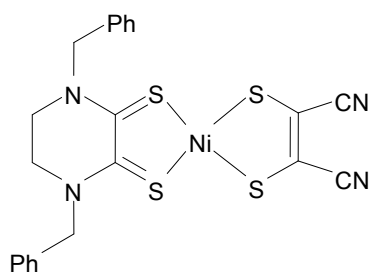
[Ni(iPr<sub>2</sub>pipdt)(dmit)] (**3a**)



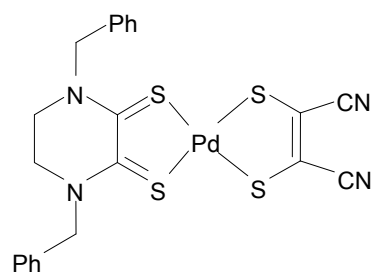
[Pd(iPr<sub>2</sub>pipdt)(dmit)] (**3b**)



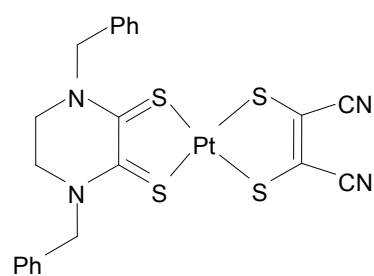
[Pt(iPr<sub>2</sub>pipdt)(dmit)] (**3c**)



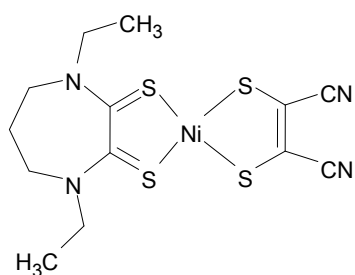
[Ni(Bz<sub>2</sub>pipdt)(mnt)] (**4a**)



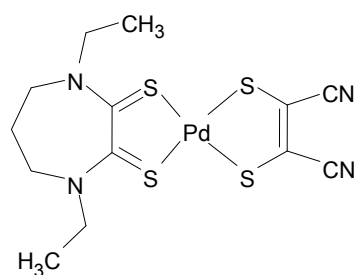
[Pd(Bz<sub>2</sub>pipdt)(mnt)] (**4b**)



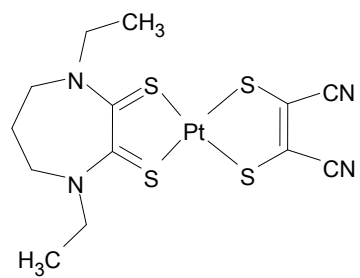
[Pt(Bz<sub>2</sub>pipdt)(mnt)] (**4c**)



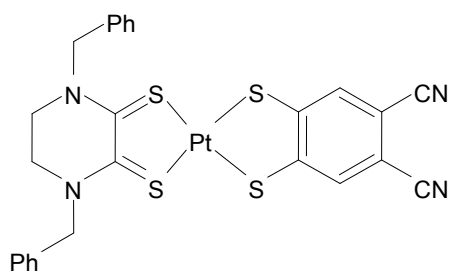
[Ni(Et<sub>2</sub>dazdt)(mnt)] (**5a**)



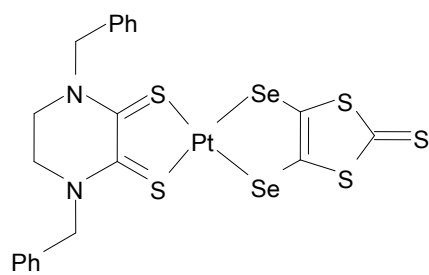
[Pd(Et<sub>2</sub>dazdt)(mnt)] (**5b**)



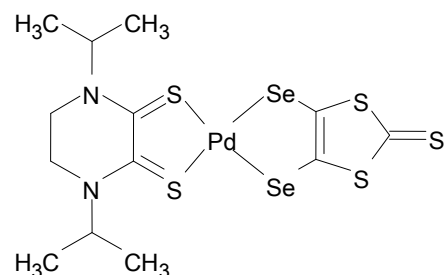
[Pt(Et<sub>2</sub>dazdt)(mnt)] (**5c**)



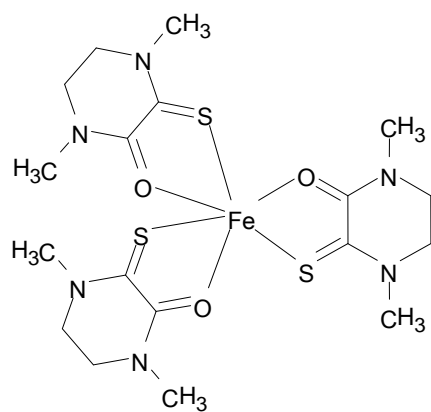
[Pt(Bz<sub>2</sub>pipdt)(dcbdt)] (**6**)



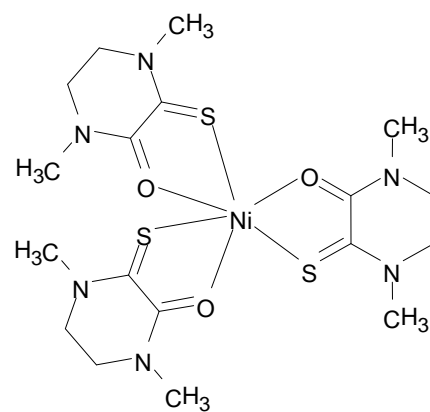
[Pt(Bz<sub>2</sub>pipdt)(dsit)] (**7a**)



[Pd(iPr<sub>2</sub>pipdt)(dsit)] (**7b**)



[Fe(Me<sub>2</sub>pipto)](BF<sub>4</sub>)<sub>2</sub> (**8a**)



[Ni(Me<sub>2</sub>pipto)<sub>3</sub>](BF<sub>4</sub>)<sub>2</sub> (**8a**)

*Chart 1*

---



---

# Chapter 1

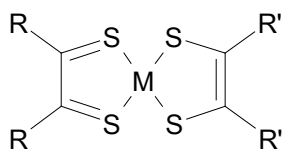
*Introduction*

An L-shaped decorative line consisting of a vertical line on the left and a horizontal line on the bottom, both starting from the same point on the left and extending to the right.

## 1.1 Introduction

Metal-dithiolene complexes are object of extensive studies since their initial synthesis to current years both for their intrinsic interest and for their applications as molecular materials with conducting<sup>[1]</sup>, magnetic<sup>[2]</sup> and optical<sup>[3,4]</sup> properties, as well as their involvement in bioinorganic processes at the catalytic centers of Mo and W oxotransferases<sup>[5]</sup>.

In particular, square planar metal bis-dithiolenes are attractive targets for electronic and optical applications because they display a high degree of communication between the ligands, through the metal center. This allows for a large degree of delocalisation of electron density in the frontier orbitals [both the highest occupied, and lowest unoccupied molecular orbitals (HOMO and LUMO, respectively)], promoting extensive intermolecular interaction. Consequently, these systems often display interesting peculiar magnetic, electronic and optical properties<sup>[6]</sup>.



Scheme 1.1

The magnetic properties of this class of compounds have been widely investigated, and a thorough account can be found in reference<sup>[7]</sup>.

Conductive properties have been tuned to develop semiconductors<sup>[1, 8]</sup>, molecular metals<sup>[9]</sup> and superconductors<sup>[10]</sup>. Optical properties have been harnessed to develop stable dyes that are active in the near infrared (NIR) region of the electromagnetic spectrum<sup>[11]</sup>.

Some metal dithiolenes show intense absorption in the NIR region of the electromagnetic spectrum (see Chapter 4), and they have found large application in Q-switching (NIR) lasers<sup>[11, 12]</sup>, where the NIR absorption can be reversibly quenched at high light intensities (as all dye molecules are in the excited state), resulting in temporary bleaching of the dye, and subsequent release of a short laser pulse. To be suitable for this application, the absorption maximum of the dyes is required to be as closely as possible to the laser wavelength and also an appropriate excited state life, good solubility (the dye is used in solution solvent) and high and photochemical stability to the laser wavelength are required.

Dithiolenes show highly tuneable absorption profiles, as well as sufficiently long excited state lifetimes ( $\tau \approx 1$  ns) upon light absorption to be investigated for their incorporation into photovoltaic devices<sup>[13]</sup>. In recent years, a great deal of interest has been focussed on the development of multi-functional materials based on metal dithiolene complexes and other components carriers of additional functionalities, where the individual properties on component can interact to perform a novel function<sup>[14]</sup>. Beyond being of intrinsic interest, an interplay between their optical, magnetic and conductive properties might lead to the development of optoelectronic or magneto-optic materials for novel device construction.

Optical properties, in particular nonlinear properties are of interest for a number of photonic applications, including high speed optical switching, telecommunication, optical data processing and storage. Nonlinear optical properties arise when the interaction of radiation with the matter, which at small fields induces an instantaneous displacement (the linear polarizability) of the electronic density away from nucleus (linear optics), involves linear high fields (laser light). In this case the polarizability of the molecule can be driven beyond the linear regime and a nonlinear polarization is induced (NLO):  $P_m = \alpha E + \beta E^2 + \gamma E^3 + \dots$  and for order hyperpolarizabilities ( $\beta > \gamma > \dots$ ) and  $\chi_1$  and  $\chi_2$  are the first and second order NLO susceptibilities (second and third order effects, respectively). Most often molecules with extensive p-delocalized system are required to promote NLO properties. Among these, symmetric and asymmetric square-planar  $d^8$  metal-dithiolene complexes can be suitable to generate third order NLO properties, but only asymmetric complexes as the molecular level, such as mixed-ligand complexes with push/pull ligands, and a non-centrosymmetric crystal packing for a bulk material, are required to generate second order NLO properties<sup>[6,15]</sup>.

## 1.2 Aim of the work

This thesis is addressed to: i) study the potential of the class of square-planar  $d^8$  metal mixed-ligand complexes in generating second order NLO activity properties as a consequence of the different electron-

withdrawing capability of the two ligands (donor/Acceptor ligands connected by the metal, as  $\pi$ -bridge) to investigate the influence of the metal and of the ligands in affecting the properties of complexes; ii) reach a deep understanding on the nature of the bonding useful to provide a structure/properties relationship which can be useful for tailoring suitable complexes to generate the desired properties; iii) compare the nature of the bonding in these and in  $d^8$  metal diimine–dithiolate complexes, a class of mixed-ligand dithiolene compounds

In Chapter 2, a background of the main chemical, electrochemical and spectral properties of the class of mixed-ligand metal  $d^8$ -dithiolene complexes, is given.

Chapter 3 describes the synthesis and full characterisation, including spectroscopic, structural and electrochemical studies of mixed-ligand metal  $d^8$ -dithiolene complexes;

Chapter 4 deals with the optical properties, mainly focusing on the generation of the second-order NLO properties. Spectroelectrochemical experiments (SCE) have been performed to point out the potential of these redox-active complexes to work as redox switchable NLO chromophores.

Chapter 5 reports the concluding remarks on this work and perspectives on future work including first results on new ligands bearing a different chalcogen atom in spite of the S one at the dithiolene core.

The electronic properties and preliminary results on coordinative properties of Me<sub>2</sub>pipto ligand are discussed and compared with those of Me<sub>2</sub>pipto. Moreover synthesis and characterisation of new [M(dithione)(diselenolate)] complexes are reported.

---

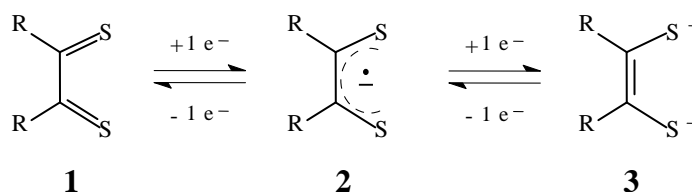
## Chapter 2

*Background*

An L-shaped decorative line consisting of a vertical line on the left and a horizontal line on the bottom, both extending from the left margin towards the right margin.

## 2.1 Dithiolene Ligands and $d^8$ Metal Dithiolene Complexes

Dithiolenes are redox-active ligands (see Scheme 2.1), capable to coordinate a variety of metals as neutral dithioketones, (1), as ene-1,2-dithiolate dianions (3), as mixed-valence thioketone-radical thiolate monoanions (2).



Scheme 2.1

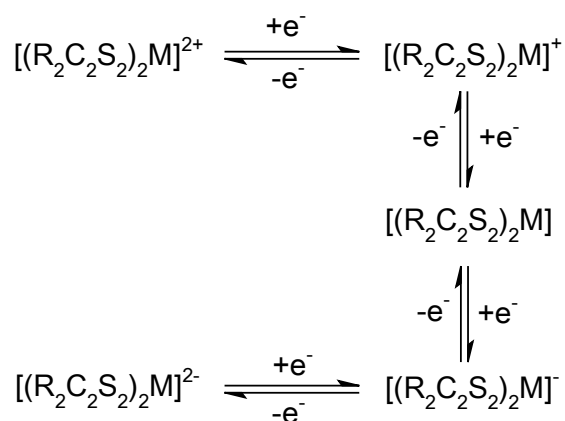
The term dithiolene is used independently of the formal oxidation state of ligands to reflect their non innocent character in several metal complexes<sup>[16]</sup>. According the Jørgeson<sup>[17]</sup>, “ligands are innocent when they allow oxidation states of the central atoms to be defined”.

More recently Ward and McCleverty<sup>[18]</sup> have pointed out that the term “noninnocent” is applied properly when it is referred to a particular combination of the metal and the ligand rather than to redox-active ligands alone. When metal-centered and ligand-centered orbitals lie at different energies, their redox potentials are separated and the related redox processes can be assigned to the metal or the ligand without ambiguity; on



the contrary, ambiguity is found where a significant mixing between the metal-centered and ligand-centered orbitals occurs. Thus the same ligand can behave as innocent or noninnocent depending on the metal involved in the complexes.

In the class of square-planar  $d^8$  metal–dithiolenes, the members of the series which may spread from the dianionic to the dicationic form<sup>[19]</sup>, can be connected through reversible one-electron redox steps as shown in Scheme 2.2.



**Scheme 2.2**

The 2+ and 2- limits are due to the fairly isolated frontier  $\pi$ -MOs, shown in Figure 2.1, which can be either empty or populated.

## Chapter 2

---

These MOs are the *in phase* (*i.p.*) and *out-of phase* (*o.o.p.*) combinations of a  $C_2S_2$  orbital, and are at high energy due to the C-S and S••S antibonding interactions within one ligand and between the two ligands<sup>[20]</sup>.

These orbitals are stabilized and destabilized by one high lying  $p_\pi$  and a lower  $d_\pi$  metal orbital, respectively. In a “Normal Bonding Scheme” the d-orbitals are destabilized relative to the ligand orbitals whereas in the  $d^8$  metal dithiolene the stabilization of d-metal orbitals relative to ligand orbitals leads to an “Inverted Bonding Scheme”<sup>[21]</sup> (see Fig. 2.1). The entity of mixing between the metal-centered and ligand-centered orbitals provides the “non-innocent/innocent” character to the ligands.

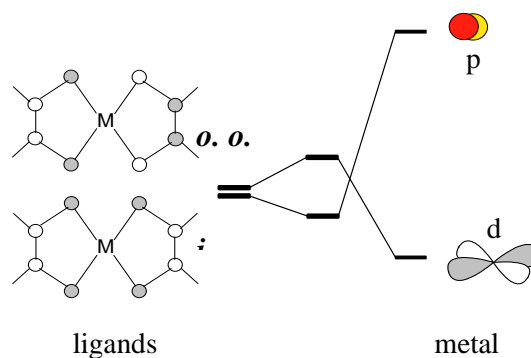
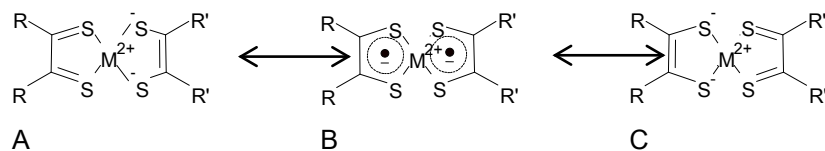


**Figure 2.1:** Frontier MOs in square-planar  $d^8$  metal-dithiolene complexes formed by the *in phase* (*i.p.*) and *out-of phase* (*o.o.p.*) combinations of  $C_2S_2$  orbitals perturbed by the metal (normal bonding scheme, see text).

Various substituents at the dithiolene core have different electronic effect on the frontier orbitals<sup>[20,22]</sup>. In general, C<sub>2</sub>S<sub>2</sub> π donor substituents (*push*) raise the energy of the HOMO (Highest Occupied Molecular Orbital) and the LUMO (Lowest Unoccupied Molecular Orbital), whose gap is lowered by a lowered interaction of the ligands orbitals with the low lying metal orbitals.

Whether the HOMO is pushed up at too high energy, an induced increased reactivity leads to the loss of one ([M(II)L<sub>2</sub>]<sup>+</sup>) or two electrons (M(II)L<sub>2</sub>)<sup>2+</sup> so that this orbital is preferentially depopulated.

In contrast, π acceptor substituents (*pull*) lower the energy of both the MOs and favour the dianionic state. Following the Lewis formalism to summarize the bonding in these systems, classical structures involving the metal in the 2+ oxidation state and the ligands in the 1,2-dithione and 1,2-enedithiolate form respectively can be applied only to the diamagnetic dicationic and dianionic members of the series. For the neutral diamagnetic complex two bonding descriptions are required: one involves a resonance hybrid among the limiting forms where the M(II) is coordinated to one neutral dithione molecule and one dithiolate dianion (see form **A** and **C** in Scheme 2.3). The other nonclassical Lewis description involves the M(II) coordinated to two ligands in radical form where the spins are antiferromagnetically coupled<sup>[23]</sup>.



### Scheme 2.3

The monocationic and monoanionic forms are also described with nonclassical Lewis formulation where the M(II) is coordinated respectively to one dithione ligand and one ligand in radical form, and to one dithiolato ligand and one ligand in radical form with the spin ( $S = 1/2$ ) highly delocalized over the molecule.

#### 2.1.1 Symmetric complexes

In neutral symmetric complexes where  $R = R'$ , (see Scheme 2.3), the overall  $\pi$  electron delocalization (form **B**) implies the equivalence of resonance structures **A** and **C**. As stated above only the low lying orbital is populated and the HOMO-LUMO dipole allowed transition ( $b_{1u} \rightarrow b_{2g}$  in  $D_{2h}$  symmetry) gives rise to the typical intense electronic transition which falls at low energies (NIR region)<sup>[22]</sup>. Complexes absorbing at approximately 1000 nm, are dyes suitable for Q-switching neodymium lasers. High thermal and photochemical stability of the dye at the laser wavelength in addition to high absorptivity of the NIR transition is required for practical use<sup>[22a]</sup>. In the monoanionic paramagnetic derivative the LUMO becomes the half-filled SOMO (Singly Occupied Molecular Orbital) and the related HOMO-SOMO transition undergoes a bathochromic shift and a decrease in intensity, while in the dianionic derivatives a bleaching is observed because the former

LUMO becomes doubly occupied. The distinct NIR absorption spectra of the redox-active members of the series make these complexes polyelectrochromic NIR dyes.

### 2.1.2 Asymmetric complexes

In neutral asymmetric complexes, different terminal groups attached to the dithiolene core ( $R \neq R'$ ) may cause a redistribution of the  $\pi$  electrons. When the differences in the push-pull character of the two ligands are small, mixed-ligand complexes show ground states describable with the limiting form **B** ( $\pi$ -delocalized systems) and optical features typical of symmetrical complexes (NIR dyes, no second order NLO activity) are predictable<sup>[24]</sup>.

When the pull ligand gives a prevailing contribution to the HOMO, and the push one to the LUMO the ground states is best described by one of the limiting  $\pi$ -localized forms, **A** or **C** where one ligand coordinates as neutral dithione and the other as dithiolate dianion<sup>[20]</sup>.

In this case the HOMO-LUMO transition has ligand to ligand charge-transfer (CT) character with some metal contribution and gives rise to an absorption band which undergoes solvatochromic shift. Therefore mixed-ligand bis-dithiolene complexes may behave as potential second-order chromophores often exhibiting non-null molecular first hyperpolarizability  $\beta$  (see Chapter 4 )<sup>[25,26]</sup>.



Most of the complexes reported in literature, are describable as  $\pi$ -localized systems and are characterized by absorptions in the visible region with medium to low molar extinction coefficients (in the 6000 to 13000 M<sup>-1</sup>cm<sup>-1</sup> range) and large negative solvatochromism<sup>[27a,32]</sup>. The HOMO-LUMO transition, where the HOMO is formed by a mixture of metal and dithiolate orbitals while the diimine orbitals give a predominant contribution to the LUMO, has considerable CT character<sup>[27a,29,32]</sup>. Accordingly, this transition is termed MMLL'CT: mixed metal-ligand to ligand charge-transfer. The negative solvatochromism of this peak and the value of  $\beta$  (*the vector part of the quadratic hyperpolarizability tensor*) is determined by the fact that the charge-transfer axis is collinear but antiparallel to the ground state dipole of the molecule (see Scheme 2.4, where **A** and **B** represent the ground and excited CT state respectively).

By virtue of all these features metal diimine dithiolates often show second order nonlinear activity. In particular, the magnitude of the molecular first hyperpolarizability of several complexes, determined from electric field induced second harmonic generation experiments (EFISH) at 1.9  $\mu\text{m}$ , ranges from 0 to  $-39 \times 10^{-30}$  esu<sup>[33]</sup>. Such results can be interpreted by taking into account that substituents on the diimine affect mainly the LUMO, and substituents on the dithiolato affect the HOMO, while the contribution of the metal to the HOMO depends on the metal-dithiolato overlap, and thus on the nature of both of them. Frequently the Ni > Pt > Pd  $\lambda_{max}$  sequence of the long wavelength has been found. In the series [M(bpy)(bdt)] (bpy= 2,2'-bipyridine) the observed Pt > Ni > Pd  $\lambda_{max}$  sequence has been

## *Chapter 2*

---

explained by taking into account a better metal-ligand overlap of Pt and bdt orbitals<sup>[29b]</sup>.

Moreover it has been shown that Pt-complexes have the highest value of the oscillator strengths suggesting that they are optimal candidates for NLO-applications.



---

# Chapter 3

*Synthesis and characterisation*



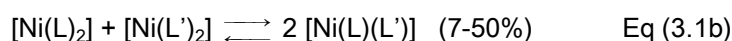
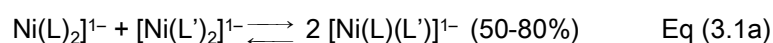
### 3.1 Introduction

As already mentioned in the first Chapter of the thesis, the square-planar  $d^8$  metal mixed-ligand dithiolene complexes of interest as potential second order NLO-chromophores are characterized by an asymmetric distribution of the charge at the  $C_2S_2MC_2S_2$  core<sup>[11]</sup>. Relatively fewer examples of  $d^8$  metal dithiolenes  $[(R_2C_2S_2)M(S_2C_2R'_2)]$  with  $R \neq R'$  than with  $R = R'$  have been reported so far. Preparative methods based on symmetrical precursors (where  $L = R_2C_2S_2$ ,  $L' = R'_2C_2S_2$  and  $R \neq R'$ ) as reagents are summarized for nickel in equations 3.1-3.3. These reactions are often reported to work similarly for the other  $d^8$  divalent metals, but well documented examples of such compounds are rare. The study of these triads is suitable to investigate the role of the metal in affecting the properties of the complexes. In particular the availability of platinum complexes will allow to investigate whether or not these complexes show similarities with the peculiar properties exhibited by platinum diimine-dithiolates, such as optimal second-order NLO activity and also photoluminescence in solution as well as large excited-state potentials<sup>[31]</sup>.

These reactions (Eq. 3.1a and 3.1b) involve ligand scrambling complicated in some instances by competing redox reactions of the symmetrical precursors and/or ligand substitutions reactions.

McCleverty and co-workers in their pioneering work on mixed-ligand metal dithiolenes<sup>[34]</sup> have recognized these complications, and were able to isolate, with satisfactory yields, mixed ligand complexes by mixing the symmetrical

monoanionic complexes. In the following examples (where L = phdt, L' = tfd and L' = mnt) through reaction in equation 3.1a and equation 3.1b.



More recently, several complexes have been obtained in 50-80% yields by applying the method described in equation 3.1<sup>[24]</sup>.

The products have been purified by reversed phase column chromatography, using aqueous acetonitrile as eluent. In this case no back reaction yielding symmetrical complexes has been observed.

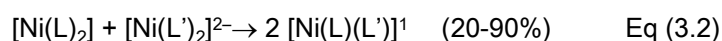
The obtained mixed-ligand compounds exhibit properties which are intermediate between those of symmetrical precursor.

Accordingly to the tuning of the electrochemical properties, some of these derivatives, as in the case  $[\text{Ni(dmit)(mnt)}]^{1-}$  and  $[\text{Ni(tdas)(dmit)}]^{1-}$ , have been selected as suitable counterions to prepare CT salts based on tetrathiafulvalene-cations (TTF) derivatives. The obtained salts exhibit metallic behaviour down to low temperature<sup>[35]</sup>.

Neutral mixed-ligand complexes have been prepared in refluxing DCE through the scrambling reaction (3.1b) in low to moderate yield, with the view to tailoring electrochemical properties and solubilities to prepare radical-cation salts, which are interesting for their electroconducting properties. An equilibrium mixture between reagents and product is formed,

and, as cited above, this leads complications in the isolation of pure mixed-ligand complexes.

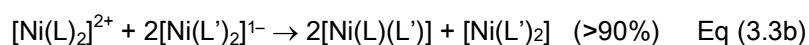
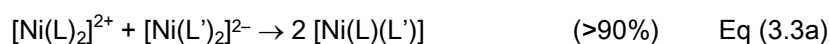
Through equation 3.2 these mixed ligand complexes have been combined



for different ligand (L = phdt and L' = mnt) obtaining satisfactorily pure salts of the  $[\text{Ni}(\text{phdt})(\text{mnt})]^{1-}$  and  $[\text{Ni}(\text{phdt})(\text{tfd})]^{1-}$  anionic complexes. Fast isolation and purification of the mixed-ligand complexes was recommended to avoid formation of an equilibrium mixture of asymmetrical and symmetrical complexes<sup>[34]</sup>.

The method of equation 3.2 may work either as a two step reaction implying a preliminary redox step with subsequent scrambling of the ligands, or simply as a metathesis<sup>[24]</sup>.

Equation 3.3a and 3.3b requires dicationic and dianionic complexes.



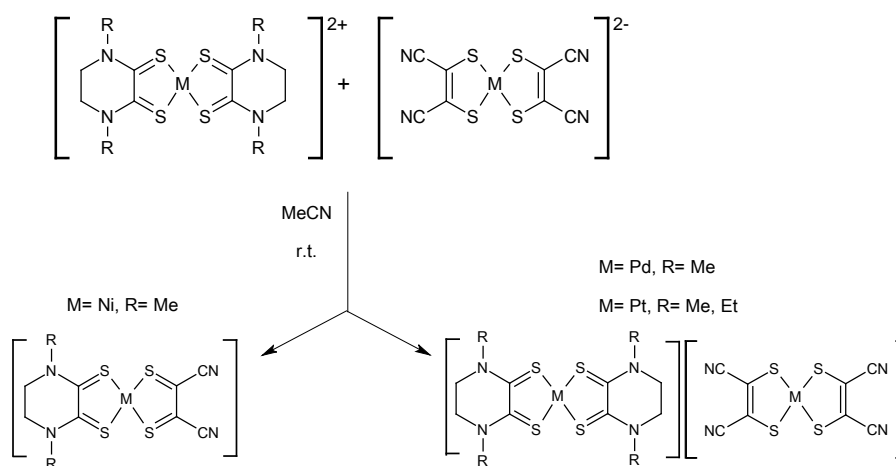
Methods 3.3a and 3.3b are very effective, giving almost quantitative yields of the mixed-ligand complexes, and can be employed where cationic and anionic complexes are available. While several stable anionic complexes are known, the cationic dithiolenes are uncommon. Among these the class of  $[\text{M}(\text{L})_n]^{2+}$  (n = 2, M= Ni, Pd, Pt, L = R<sub>2</sub>pipdt; n=3, M=Ni, L=R<sub>2</sub>dazdt) have

### Chapter 3

---

proved to be suitable precursors to prepare in almost quantitative yields mixed-ligand derivatives ( $L = R_2\text{pipdt}$ )<sup>[6,25,36,37]</sup> ( $L=R_2\text{dazdt}$ )<sup>[38]</sup> by reacting with Ni-dianionic dithiolenes. This reaction can work also by using monoanionic complexes, when the complexes are more easily available in this state, but the isolation of the mixed ligand complex requires further purification steps due to the formation of the symmetric complexes.

As shown in Scheme 3.1, the corresponding reaction by using the palladium or platinum corresponding complexes afforded instead  $[\text{M}(R_2\text{pipdt})_2][\text{M}(\text{mnt})_2]$  ( $M = \text{Pd}$  and  $\text{Pt}$ ) CT double salts. These complexes exhibit interesting solid state properties related to ion-pair charge-transfer transitions.



**Scheme 3.1:** Synthetic route

## Synthesis and characterisation

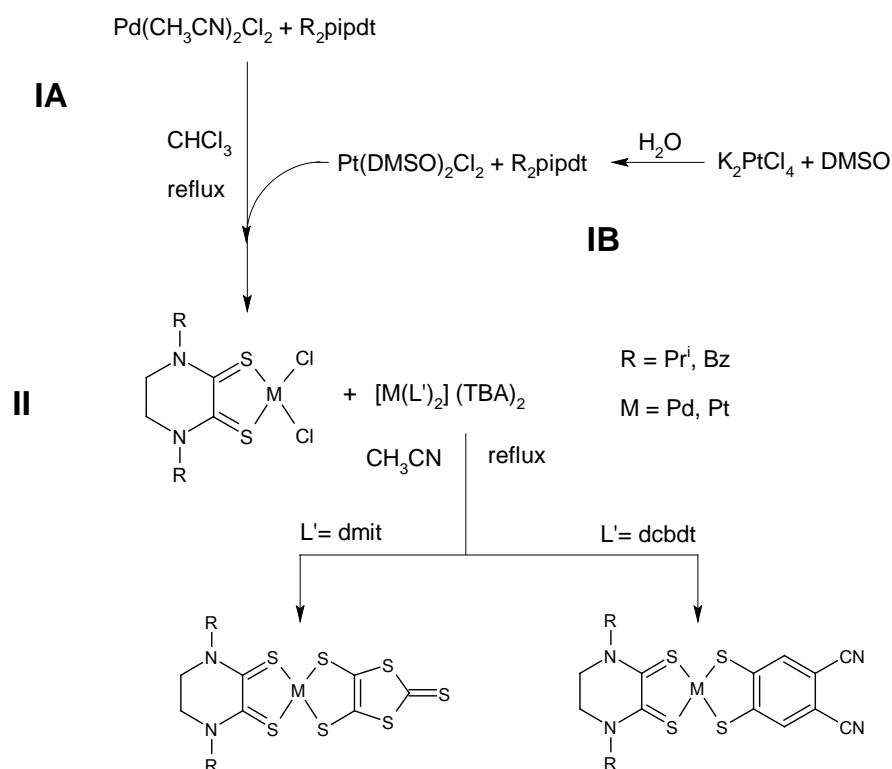
---

After several attempts during my thesis, a suitable procedure to obtain in high yields several metal dithiolene complexes of the Ni triad (Ni, Pd and Pt) has been designed and successfully applied.

### 3.2 M(R<sub>2</sub>pipdt)(L') synthesis and characterisation

#### 3.2.1 Synthesis

In Scheme 3.2 a summary of the synthetic procedures used to obtain mixed ligand dithiolene complexes is reported.



**Scheme 3.2:** Reaction pathways for  $[\text{M}(\text{R}_2\text{pipdt})(\text{L}')]$

As shown in the Scheme 3.2:

I) Methods IA and IB are used to obtain dichloro complexes of Pd and Pt, respectively:

IA. This pathway follows a modification of the procedure reported to obtain the dicationic complexes  $[M(R_2\text{pipdt})^{2+}]$  using a metal to ligand molar ratio of 2:1<sup>[24]</sup>. Instead using a metal to ligand molar ratio 1:1 ( $R_2\text{pipdt} : [\text{Pd}(\text{CH}_3\text{CN})_2\text{Cl}_2]$ ) the dichloro compound of general formula  $[M(R_2\text{pipdt})\text{Cl}_2]$  is obtained. The reaction is carried out in chloroform under reflux for one day. The crude product precipitates as an air stable red/orange solid ( $[\text{Pd}(R_2\text{pipdt})\text{Cl}_2]$ ) which is collected by filtration and washed with ether.

IB. The second method used to synthesize the Pt-dichloro complexes involves an additional step leading to formation of  $[\text{Pt}(\text{DMSO})\text{Cl}_2]$  as starting material. Few drops of DMSO (ratio 1:2) are added to a  $\text{K}_2\text{PtCl}_4$  in  $\text{H}_2\text{O}$  mixture under mixing. After 30 min a precipitate of  $[\text{Pt}(\text{DMSO})\text{Cl}_2]$  is formed<sup>[38]</sup>. This precursor reacts with  $R_2\text{pipdt}$  in  $\text{CHCl}_3$  under reflux and  $[\text{Pt}(R_2\text{pipdt})\text{Cl}_2]$  is obtained.

II) The mixed ligand metal dithiolene complexes  $[M(R_2\text{pipdt})(\text{dmit})]$ , are obtained by mixing  $[M(R_2\text{pipdt})\text{Cl}_2]$  ( $M=\text{Pd}, \text{Pt}$ ) with  $(\text{Bu}_4\text{N})_2[M(L')_2]$ , ( $L' = \text{dmit}, \text{dcbdt}$ ). This reaction involves the facile displacement of two chloride ions by the chelating  $L'$  dianion.



### 3.3 [M(R<sub>2</sub>pipdt)(dmit)] (M(II) = Ni, Pd, Pt)

#### 3.3.1 Structural characterization

Crystals of [Pd(R<sub>2</sub>pipdt)(dmit)] and [Pt(R<sub>2</sub>pipdt)(dmit)], were grown by diffusion of diethyl ether into a concentrated solution of complexes in DMF. The obtained crystals are suitable for X-ray diffractometric characterization.

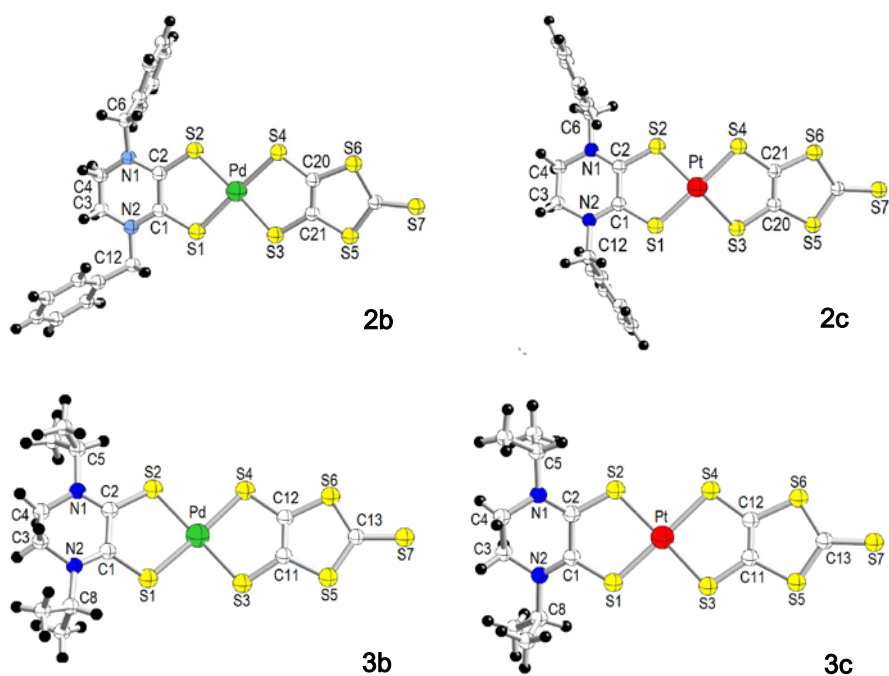


**Figure 3.1:** View of molecules in crystal of [M(R<sub>2</sub>pipdt)(dmit)].

In Fig. 3.1 a view of the molecules of complexes is reported.

As shown central atom (Pd, Pt) is coordinated by four S atoms in an approximately square planar environment, with M-S coordination bonds broadly similar on both sides of the complex. Within the central MS<sub>4</sub>C<sub>4</sub> core, the C-C bond on the dmit ligand is significantly shorter than that of the Bz<sub>2</sub>pipdt (1.450(1) Å for **2a** and 1.475(3) Å for **2b** and <sup>i</sup>Pr<sub>2</sub>pipdt (1.489(4) Å for **3a** and 1.490(6) Å for **3b**, while the C-S bonds are shorter on the R<sub>2</sub>pipdt than the dmit (see Table 3.3). These results are consistent with previous studies of push-pull complexes, and confirm the C-S  $\pi^*$  and C-C  $\pi$  nature of the frontier MOs on the dmit ligands<sup>[20]</sup>. A comparison of the C-S bond lengths with those reported for free ligand analogues of R<sub>2</sub>pipdt<sup>[6]</sup>, and dmit, shows good agreement, which confirms the [M(dithione)(dithiolate)] nature of both complexes (see Fig. 3.1; see Table 3.4.).

The molecules are approximately planar, in case of the complexes with the isopropyl substituent the torsion angle is 9,6° around N1, C3, C4, N2 for Pd. This suggests that the Np $_{\pi}$ -lone pair is almost parallel to the C<sub>2</sub>S<sub>2</sub>  $\pi$ -system as previously reported<sup>[20]</sup>.

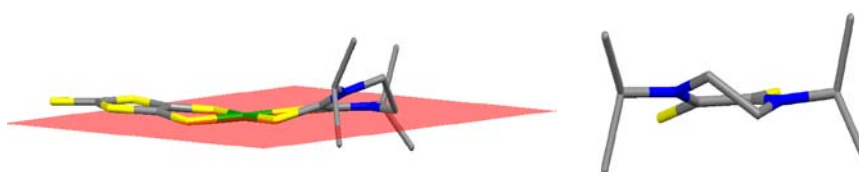


**Figure 3.2:** Torsion angle of [Pd(<sup>i</sup>Pr<sub>2</sub>pipdt)(dmit)]

Chapter 3

Crystallographic data for [Pd(Bz <sub>2</sub> pipdt)(dmit)] and [Pt(Bz <sub>2</sub> pipdt)(dmit)]		
Empirical formula	C <sub>21</sub> H <sub>18</sub> N <sub>2</sub> PdS <sub>7</sub>	C <sub>21</sub> H <sub>18</sub> N <sub>2</sub> PtS <sub>7</sub>
Formula weight	629.23	717.88
Crystal size (mm)	0.18 x 0.07 x 0.05	0.35 x 0.08 x 0.08
Crystal system	Triclinic	Triclinic
Space group	<i>P</i> -1	<i>P</i> -1
a, b, c (Å)	7.828(3), 12.132(4), 13.872(5)	7.969(1), 12.082(1), 13.983(1)
α, β, γ (deg.)	95.191(6), 106.113(5), 104.301(6)	75.645(1), 75.462(2), 72.984(1)
V (Å <sup>3</sup> )	1208.4(8)	1223.81(18)
Z	1	2
T (K)	293	293
ρ(calc) (Mg/m <sup>3</sup> )	1.729	1.948
μ (mm <sup>-1</sup> )	1.386	6.343
θ range (deg.)	1.76 to 24.85	1.53 to 30.00
No. of rflcn/obsv >4σ(F)	12926 / 4163	9442 / 7106
Goof	1.002	1.010
R1 [a]	0.0714	0.0246
wR2 [b]	0.1079	0.0481

**Table 3.1:** Summary of X-ray crystallographic data for **2b** and **2c**. [a] R1 =  $\sum ||F_o| - |F_c|| / \sum |F_o|$ ; [b] wR2 =  $[\sum [w(F_o^2 - F_c^2)^2] / \sum [w(F_o^2)^2]]^{1/2}$ , w =  $1 / [\sigma^2(F_o^2) + (aP)^2 + bP]$ , where P =  $[\max(F_o^2, 0) + 2F_c^2] / 3$ .

Synthesis and characterisation

Crystallographic data for [Pd( <sup>i</sup> Pr <sub>2</sub> pipdt)(dmit)] and [Pt( <sup>i</sup> Pr <sub>2</sub> pipdt)(dmit)]		
Empirical formula	C <sub>13</sub> H <sub>18</sub> N <sub>4</sub> Pd <sub>2</sub> S <sub>7</sub>	C <sub>13</sub> H <sub>18</sub> N <sub>2</sub> PtS <sub>7</sub>
Formula weight	533.11	621.80
Crystal size (mm)	0.20 x 0.15 x 0.10	0.32 x 0.12 x 0.10
Crystal system	Monoclinic	Orthorhombic
Space group	P2 <sub>1</sub> /n	Pbca
a, b, c (Å)	9.687(2), 17.320(5), 12.544(3)	14.578(1), 16.218(1), 16.257(1)
α, β, γ (deg.)	90, 108.034(7), 90	90, 90, 90
V (Å <sup>3</sup> )	2001.2(9)	3843.6(4)
Z	4	8
T (K)	293 (2)	200 (2)
ρ(calc) (Mg/m <sup>3</sup> )	1.769	2.149
μ (mm <sup>-1</sup> )	1.656	8.060
θ range (deg.)	2.07 to 28.03	2.26 to 27.03
No. of rflcn/obsv >4σ(F)	24254 / 4810	41982 / 4218
Goof	1.005	1.009
R1 [a]	0.0475	0.0582
wR2 [b]	0.0673	0.0738

**Table 3.2:** Summary of X-ray crystallographic data for **3b** and **3c**. [a]  $R1 = \sum ||F_o| - |F_c|| / \sum |F_o|$ ; [b]  $wR2 = [\sum [w(F_o^2 - F_c^2)^2] / \sum [w(F_o^2)^2]]^{1/2}$ ,  $w = 1 / [\sigma^2(F_o^2) + (aP)^2 + bP]$ , where  $P = [\max(F_o^2, 0) + 2F_c^2] / 3$ .

Selected bond of dithiolene core lengths are reported in Table 3.3.

Bond lengths (Å) of [M(Bz <sub>2</sub> pipdt)(dmit)]				Bond lengths (Å) of [M( <sup>i</sup> Pr <sub>2</sub> pipdt)(dmit)]			
Pd-S(1)	2.3084(17)	Pt-S(1)	2.2720(7)	Pd-S(1)	2.2714(9)	Pt-S(1)	2.2749(13)
Pd-S(2)	2.2706(15)	Pt-S(2)	2.2706(7)	Pd-S(2)	2.2837(8)	Pt-S(2)	2.2746(13)
Pd-S(3)	2.3165(15)	Pt-S(3)	2.2898(7)	Pd-S(3)	2.2959(10)	Pt-S(3)	2.2841(13)
Pd-S(4)	2.2916(16)	Pt-S(4)	2.2904(7)	Pd-S(4)	2.2842(8)	Pt-S(4)	2.2790(13)

**Table 3.3:** Selected bond for [M(Bz<sub>2</sub>pipdt)(dmit)] and [M(<sup>i</sup>Pr<sub>2</sub>pipdt)(dmit)]

Chapter 3

Selected bond distances and angles are given in Tables 3.4 and 3.5.

Bond lengths (Å) of [M(Bz <sub>2</sub> pipdt)(dmit)]			Bond lengths (Å) of [M( <sup>i</sup> Pr <sub>2</sub> pipdt)(dmit)]		
	Pd	Pt		Pd	Pt
S(1)-C(1)	1.690(5)	1.700(3)	S(1)-C(1)	1.685(3)	1.702(5)
S(2)-C(2)	1.693(5)	1.691(2)	S(2)-C(2)	1.696(3)	1.701(5)
C(1)-C(2)	1.450(1)	1.475(3)	C(1)-C(2)	1.489(4)	1.490(6)
S(3)-C(20)	1.744(6)	1.739(6)	S(3)-C(12)	1.743(3)	1.713(5)
S(4)-C(21)	1.741(5)	1.741(3)	S(4)-C(11)	1.729(3)	1.730(5)
C(20)-C(21)	1.349(7)	1.339(3)	C(11)-C(12)	1.343(4)	1.287(7)

**Table 3.4:** Selected bond [M(Bz<sub>2</sub>pipdt)(dmit)] and [M(<sup>i</sup>Pr<sub>2</sub>pipdt)(dmit)]

Angle (deg.) of [M(Bz <sub>2</sub> pipdt)(dmit)]			Angle (deg.) of [M( <sup>i</sup> Pr <sub>2</sub> pipdt)(dmit)]		
	Pd	Pt		Pd	Pt
S(1)-M-S(2)	88.76(5)	87.86(2)	S(1)-M-S(2)	87.96(3)	87.74(5)
S(3)-M-S(4)	91.08(7)	90.78(2)	S(1)-M-S(3)	179.85(5)	90.72(5)
S(1)-M-S(3)	93.86(5)	90.76(2)	S(1)-M-S(4)	89.39(3)	177.90(5)
S(2)-M-S(4)	173.98(1)	176.14(3)	S(2)-M-S(3)	91.48(3)	178.40(5)
S(2)-M-S(3)	175.83(6)	178.02(2)	S(2)-M-S(4)	176.85(3)	90.41(4)
S(2)-M-S(4)	173.98(1)	176.14(3)	S(3)-M-S(4)	91.14(3)	91.13(5)
S(2)-M-S(3)	175.83(6)	178.02(2)	C(1)-S(1)-M	106.38(10)	106.48(17)
S(2)-M-S(4)	86.52(5)	90.69(2)	C(2)-S(2)-M	105.29(10)	106.22(16)
C(1)-S(1)-M	103.39(18)	106.35(9)	C(12)-S(3)-M	100.21(9)	99.75(18)
C(2)-S(2)-M	105.43(18)	106.35(9)	C(11)-S(4)-M	100.83(9)	99.23(18)
C(20)-S(3)-M	100.23(19)	101.19(9)	S(1)-M-S(2)	87.96(3)	87.74(5)
C(21)-S(4)-M	100.97(19)	100.86(9)	S(1)-M-S(3)	179.85(5)	90.72(5)

**Table 3.5:** Selected angles for [M(Bz<sub>2</sub>pipdt)(dmit)] and [M(<sup>i</sup>Pr<sub>2</sub>pipdt)(dmit)]

Figure 3.3 shows that, in the crystal lattice, the complex units are almost parallel and head-to-tail with respect to each other.

View of the crystal lattice of [Pd(Bz<sub>2</sub>pipdt)(dmit)] and [Pt(Bz<sub>2</sub>pipdt)(dmit)]

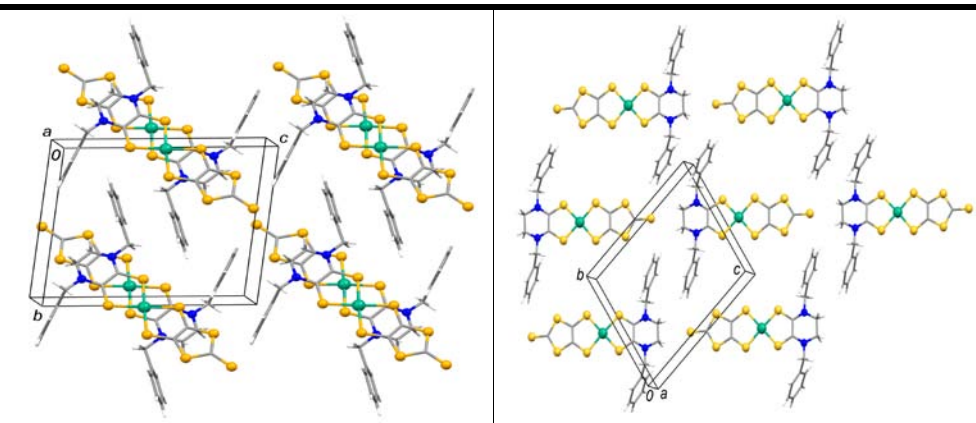
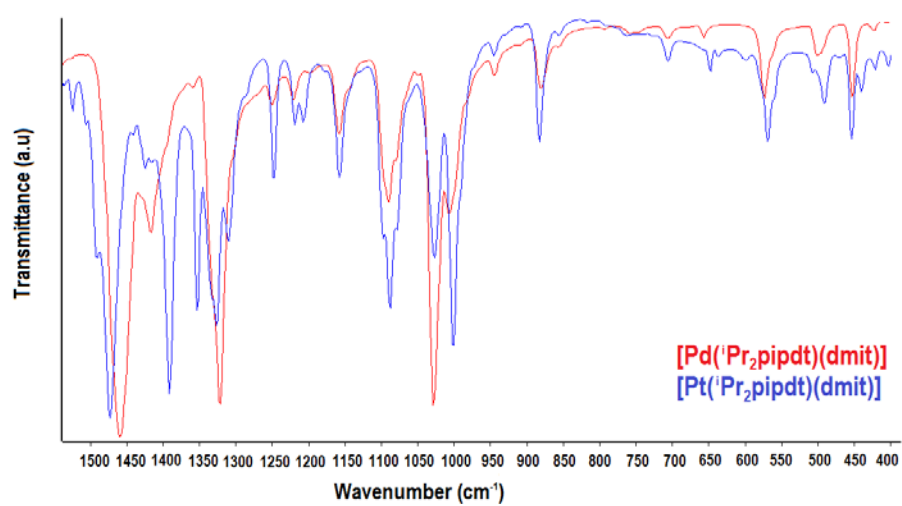


**Figure 3.3:** Single crystal X-ray data showing: (a) packing structure of **2b** in a herringbone packing arrangement; (b) packing structure of **2c** in a head-to-tail puckered sheet arrangement.

### 3.3.2 Vibrational Spectroscopy

The FT-IR spectra of the complexes under discussion are shown in Figures 3.4, where the spectra of compound **3b** and **3c** are reported for comparison. (The spectra of compounds **2b** and **2c** are reported in the Appendix Section). It is possible to assign the following common features: the CH vibrations near 2900 cm<sup>-1</sup>, the M-S vibrations which fall in the range of 402-382 cm<sup>-1</sup>, the C=C stretching peaks at 1470 cm<sup>-1</sup> for Pd and 1457 cm<sup>-1</sup> for Pt

complexes. In the IR spectrum of **2b** and **2c** the  $\nu(\text{CN})$  vibration of the pipdt ring falls near  $1510\text{ cm}^{-1}$ .



---

**Figure 3.4:** Vibrational spectrum of **3b** and **3c** in the  $1550\text{--}400\text{ cm}^{-1}$  spectral region.

### 3.3.3 Electrochemistry

Cyclic voltammetric data for the triads are collected in Table 3.6. Complexes based on R<sub>2</sub>pipdt as push ligands and dmit as pull ligand show two reversible reduction waves and one irreversible oxidation wave.

Cyclic Voltammetric data of [M(X)(Y)] (X= Bz <sub>2</sub> pipdt, Pr <sub>2</sub> pipdt; Y=dmit) complexes			
Complex	E <sub>a</sub> (V) <sup>a</sup>	E <sup>1/2</sup> (V)	E <sup>2/2</sup> (V)
	M(X)(Y) <sup>0</sup> ↔ M(X)(Y) <sup>+</sup> + e <sup>-</sup>	M(X)(Y) <sup>0</sup> + e <sup>-</sup> ↔ M(X)(Y) <sup>-</sup>	M(X)(Y) <sup>-</sup> + e <sup>-</sup> ↔ M(X)(Y) <sup>2-</sup>
[Ni(Bz <sub>2</sub> pipdt)(dmit)]	+0.69	-0.41	-0.91
[Pd(Bz <sub>2</sub> pipdt)(dmit)]	+0.84	-0.36	-0.81
[Pt(Bz <sub>2</sub> pipdt)(dmit)]	+0.86	-0.39	-0.84
[Ni(Pr <sub>2</sub> pipdt)(dmit)]	+1.01	-0.49	-1.04
[Pd(Pr <sub>2</sub> pipdt)(dmit)]	+0.84	-0.38	-0.93
[Pt(Pr <sub>2</sub> pipdt)(dmit)]	+0.71	-0.42	-0.96

**Table 3.6:** Cyclic Voltammetric data of [M(R<sub>2</sub>pipdt)(dmit)] complexes performed on a solution of 0.1 M TBABF<sub>4</sub> in DMF. <sup>a</sup> Irreversible.

The two processes at negative potentials can be assigned to the sequential reduction of the complexes, [MLL']<sup>0/1-</sup>, [MLL']<sup>1-/2-</sup>, as zero current (I) was observed at applied potential E = 0, suggesting this to be the neutral form for both complexes. The irreversible process at positive potentials for complexes is assigned to their oxidation, [MLL']<sup>0/1+</sup>, indicating the formation of a cation under cyclic voltammetric conditions.



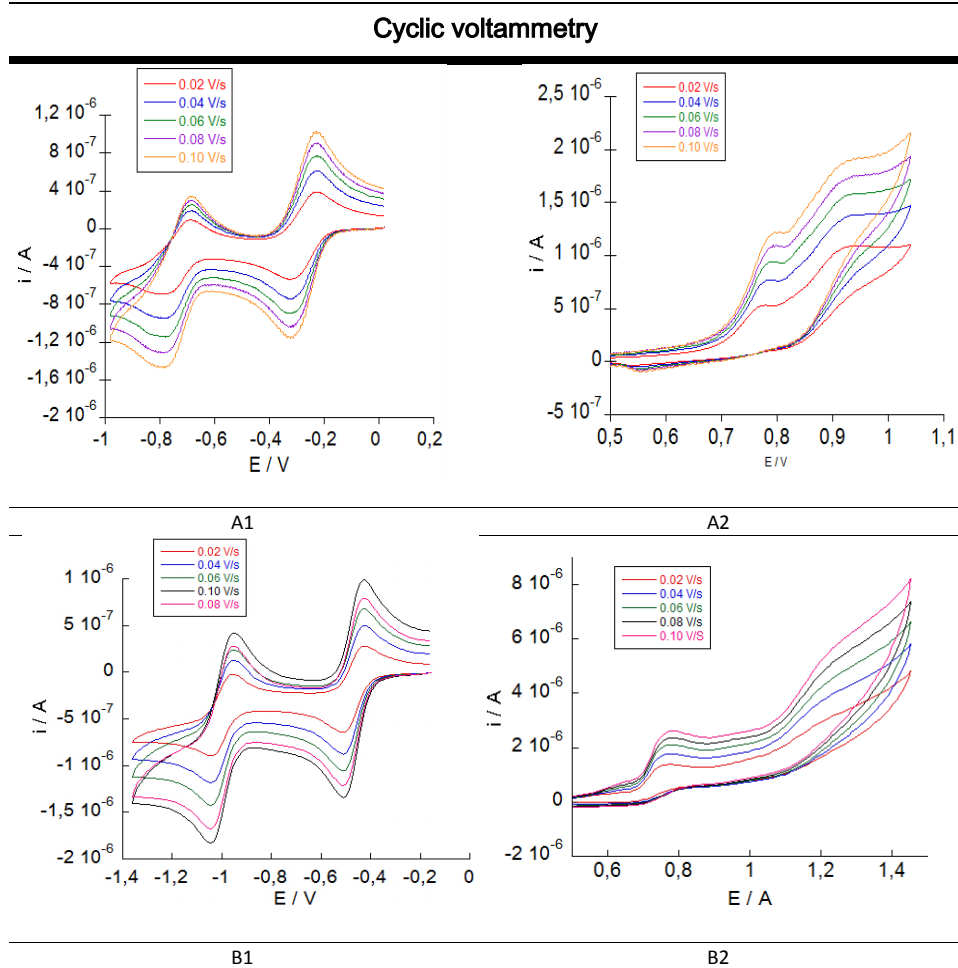


**Figure 3.5:** Cyclic voltammetry in 0.1 M TBABF<sub>4</sub>/DMF, measuring current ( $i$ ), in response to an applied potential ( $E$ ): (A1-B1) several scan (different scan rate mVs<sup>-1</sup>) of **2c** and **3c**, showing two reversible redox reduction processes; (A2-B2) several scan (different scan rate mVs<sup>-1</sup>) of **2c** and **3c**, showing one irreversible redox oxidation processes.

### 3.3.4 Structural characterization of [Pt(Bz<sub>2</sub>pipdt)(dcbdt)]

Crystals of [Pt(Bz<sub>2</sub>pipdt)(dcbdt)] were grown by slow diffusion of diethyl ether into a concentrated solution of the complex in DMF.

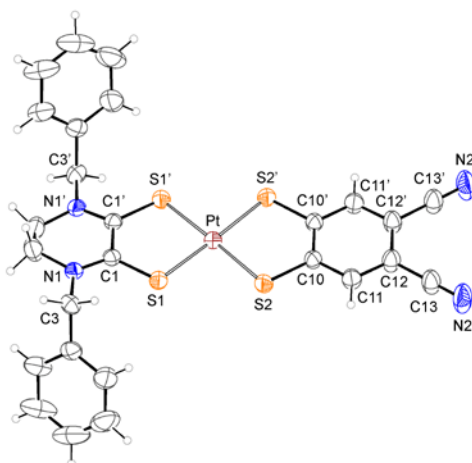


**Figure 3.6:** ORTEP drawing of **6a** with thermal ellipsoids drawn at the 30% probability level.

As shown the platinum is coordinated by four S atoms in an approximately square planar environment, with M-S coordination bonds broadly similar on both sides of the complex (see Table 3.7). Figure 3.7 shows that, in the crystal lattice for both complexes, the complex units are almost parallel and head-to-tail with respect to each other.

The Pt atoms are located between two hexaatomic rings of the (Bz<sub>2</sub>pipdt) ligand. The distance between the centroid of the ligand and the Pt atom is of about 4 Å.

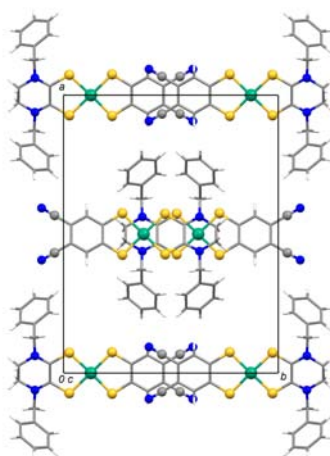


**Figure 3.7:** Single crystal X-ray data showing: crystal packing of **6** projected along the *c*.

A summary of X-ray crystallographic parameters and selected bond of dithiolene core lengths are reported in Tables 3.7 and 3.8.

Bond lengths (Å) of [Pt(Bz <sub>2</sub> pipdt)(dcbdt)]	
Pt-S1	2.2784(10)
Pt-S1'	2.2784(10)
Pt-S2	2.2734(10)
Pt-S2'	2.2734(10)

**Table 3.7:** Selected bond of the core for [Pt(Bz<sub>2</sub>pipdt)(dcbdt)]

## Synthesis and characterisation

Crystallographic data for [Pt(Bz <sub>2</sub> pipdt)(dcbdt)]	
Empirical formula	C <sub>26</sub> H <sub>20</sub> N <sub>4</sub> PtS <sub>4</sub>
Formula weight	711.79
Crystal size (mm)	0.25 x 0.10 x 0.07
Crystal system	Orthorhombic
Space group	<i>F</i> bcn
a, b, c (Å)	21.151(2), 16.300(1), 7.921(1)
α, β, γ (deg.)	90,90,90
V (Å <sup>3</sup> )	2730.9(5)
Z	4
T (K)	293(2)
ρ(calc) (Mg/m <sup>3</sup> )	1.731
μ (mm <sup>-1</sup> )	5.466
θ range (deg.)	1.58 to 28.63
No. of rflcn/obsv >4σ(F)	36999 / 3513
Goof	1.004
R1 [a]	0.0610
wR2 [b]	0.0656

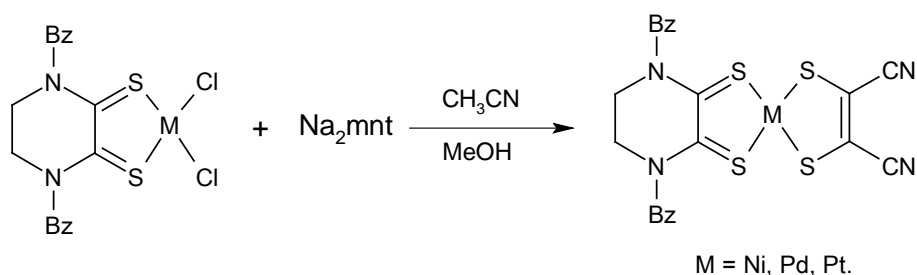
**Table 3.8:** Summary of X-ray crystallographic data for 3a and 3b. [a]  $R1 = \sum ||F_o| - |F_c|| / \sum |F_o|$ ; [b]  $wR2 = [\sum [w(F_o^2 - F_c^2)^2] / \sum [w(F_o^2)^2]]^{1/2}$ ,  $w = 1 / [\sigma^2(F_o^2) + (aP)^2 + bP]$ , where  $P = [\max(F_o^2, 0) + 2F_c^2] / 3$ .

In Appendix A2, another selected bond distances and angles are given.

### 3.4 [M(L)(mnt)] synthesis and characterisation

#### 3.4.1 Synthesis of [M(Bz<sub>2</sub>pipdt)(mnt)] (M(II) = Ni, Pd, Pt)

The synthesis of M(Bz<sub>2</sub>pipdt)(mnt) is described in details in paragraph 3.5.



**Scheme 3.3:** Synthetic route for [M(Bz<sub>2</sub>pipdt)(mnt)] (M(II) = Ni, Pd, Pt).

In scheme 3.3, the reaction pathway for the [M(Bz<sub>2</sub>pipdt)(mnt)] complexes is shown.

[M(II)(Bz<sub>2</sub>pipdt)(mnt)] are prepared through a one-step procedure by mixing [M(Bz<sub>2</sub>pipdt)Cl<sub>2</sub>] and Na<sub>2</sub>mnt, (1:1 molar ratio), in CH<sub>3</sub>CN/MeOH (1:1 v/v) mixture under stirring for the Ni complex and under reflux for one day for Pd and Pt. The obtained products are dark-green air stable solid. Crystals are formed after slow solvent evaporation of diethyl ether, these solids are collected and recrystallised from a solution of complexes in DMF.

### 3.4.2 Structural characterization

Figure 3.8 shows the molecules of  $[\text{Ni}(\text{Bz}_2\text{pipdt})(\text{mnt})]$ ,  $[\text{Pd}(\text{Bz}_2\text{pipdt})(\text{mnt})]$ , and  $[\text{Pt}(\text{Bz}_2\text{pipdt})(\text{mnt})]$ .

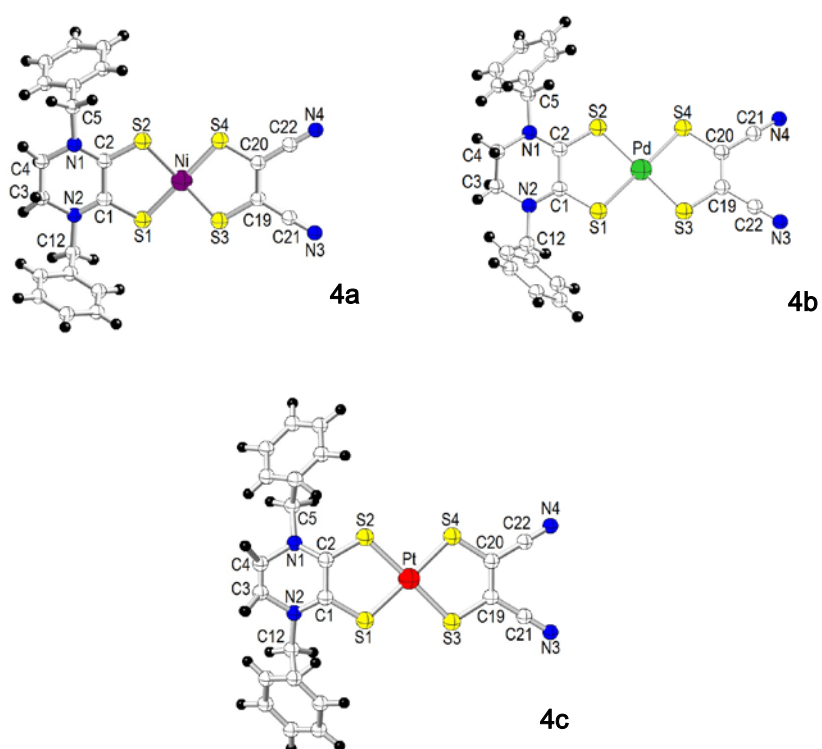


**Figure 3.8:** Crystal structure of  $[\text{M}(\text{Bz}_2\text{pipdt})(\text{mnt})]$  ( $\text{M}(\text{II}) = \text{Ni}, \text{Pd}, \text{Pt}$ ).

## Chapter 3

---

Ni derivative crystallizes in the monoclinic  $C2/c$  space group, instead the two compounds of Pd and Pt are isostructural and crystallize in the orthorhombic  $Fbcn$  space group.

Bond lengths (Å) of [Ni(Bz <sub>2</sub> pipdt)(mnt)], [Pd(Bz <sub>2</sub> pipdt)(mnt)] and [Pt(Bz <sub>2</sub> pipdt)(mnt)]					
<b>Ni-S(1)</b>	2.156(2)	<b>Pd-S(1)</b>	2.2747(9)	<b>Pt-S(1)</b>	2.2689(9)
<b>Ni-S(2)</b>	2.156(2)	<b>Pd-S(2)</b>	2.2747(9)	<b>Pt-S(2)</b>	2.2689(9)
<b>Ni-S(3)</b>	2.134(2)	<b>Pd-S(3)</b>	2.2893(9)	<b>Pt-S(3)</b>	2.2780(9)
<b>Ni-S(4)</b>	2.134(2)	<b>Pd-S(4)</b>	2.2893(9)	<b>Pt-S(4)</b>	2.2780(9)

**Table 3.9:** Selected bond of the dithiolene core of [M(Bz<sub>2</sub>pipdt)(mnt)] (M(II) = Ni, Pd, Pt).

In all complexes, four sulfur atoms from two different ligands define the coordination environment of the metals, which are in a slightly distorted square planar geometry since the donor systems of the two ligands are not exactly coplanar. The distortion is more pronounced for the Ni(II) complex (dihedral angle between the two donor-sets planes of 8°) than the Pd(II) or Pt(II) complexes (dihedral angle of 5°). A summary of X-ray crystallographic parameters and another selected bond lengths and angles for all complexes are reported in Tables 3.9, 3.10 and 3.11.

Synthesis and characterisation

Crystallographic data for [Pd(Bz <sub>2</sub> pipdt)(mnt)], [Pd(Bz <sub>2</sub> pipdt)(mnt)] and [Pt(Bz <sub>2</sub> pipdt)(mnt)]			
Empirical formula	C <sub>22</sub> H <sub>18</sub> N <sub>4</sub> NiS <sub>4</sub>	C <sub>22</sub> H <sub>18</sub> N <sub>4</sub> PdS <sub>4</sub>	C <sub>22</sub> H <sub>18</sub> N <sub>4</sub> PtS <sub>4</sub>
Formula weight	525.35	573.04	661.73
Crystal size (mm)	0.25 x 0.10 x 0.05	0.45 x 0.15 x 0.10	0.45 x 0.10 x 0.05
Crystal system	Monoclinic	Orthorhombic	Orthorhombic
Space group	C2/c	Pbcn	Pbcn
a, b, c (Å)	22.154(7), 13.529(5), 7.962(3)	21.414(2), 13.705(1), 8.073(1)	21.37467), 13.712(4), 8.097(1)
α, β, γ (deg.)	90, 106.73(2), 90	90, 90, 90	90, 90, 90
V (Å <sup>3</sup> )	2285.4(14)	2369.3(4)	2373(10)
Z	4	4	4
T (K)	293(2)	293(2)	293(2)
ρ(calc) (Mg/m <sup>3</sup> )	1.527	1.607	1.852
μ (mm <sup>-1</sup> )	1.232	1.153	6.282
θ range (deg.)	1.79 to 26.00	1.76 to 27.03	1.76 to 27.08
No. of rflcn/obsv >4σ(F)	12224/2242	25679/2600	25801/2616
Goof	1.008	1.013	1.003
R1 [a]	0.1460	0.0584	0.0407
wR2 [b]	0.1371	0.1010	0.0417

**Table 3.10:** Summary of X-ray crystallographic data for **4a**, **4b** and **4c** [a]  $R1 = \sum ||F_o| - |F_c|| / \sum |F_o|$ ; [b]  $wR2 = [\sum [w(F_o^2 - F_c^2)^2] / \sum [w(F_o^2)^2]]^{1/2}$ ,  $w = 1 / [\sigma^2(F_o^2) + (aP)^2 + bP]$ , where  $P = [\max(F_o^2, 0) + 2F_c^2] / 3$ .



Chapter 3

Bond lengths (Å) of [Ni(Bz <sub>2</sub> pipdt)(mnt)], [Pd(Bz <sub>2</sub> pipdt)(mnt)] and [Pt(Bz <sub>2</sub> pipdt)(mnt)]					
	Ni		Pd		Pt
S(1)- C(1)	1.690(6)	S(1)- C(1)	1.688(3)	S(1)- C(1)	1.691(3)
S(2)- C(2)	1.690(6)	S(2)- C(2)	1.688(3)	S(2)- C(2)	1.691(3)
C(1)- C(2)	1.491(12)	C(1)- C(2)	1.499(7)	C(1)- C(2)	1.490(6)
S(3)- C(12)	1.716(7)	S(3)- C(12)	1.734(4)	S(3)- C(12)	1.735(3)
S(4)- C(11)	1.716(7)	S(4)- C(11)	1.734(4)	S(4)- C(11)	1.735(3)
C(11)- C(12)	1.391(13)	C(11)- C(12)	1.354(7)	C(11)- C(12)	1.343(6)

Table 3.11: Selected bond of [M(Bz<sub>2</sub>pipdt)(mnt)] (M(II) = Ni, Pd, Pt).

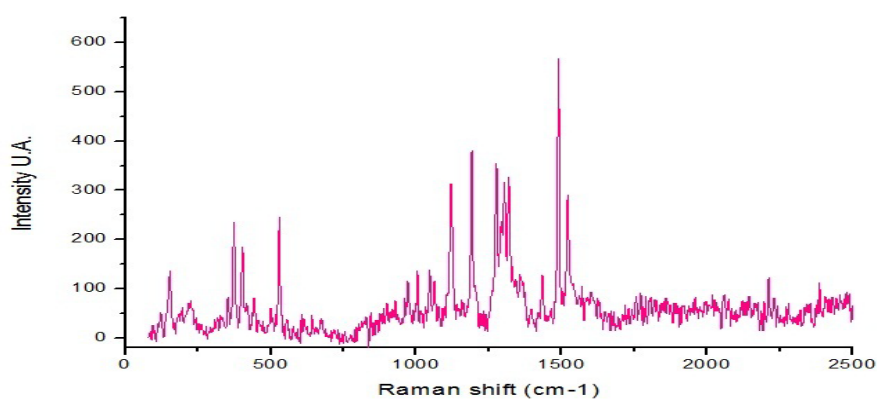
In table 3.12, another selected bond distances and angles are given.

Angle (deg.) of [Ni(Bz <sub>2</sub> pipdt)(mnt)], [Pd(Bz <sub>2</sub> pipdt)(mnt)] and [Pt(Bz <sub>2</sub> pipdt)(mnt)]					
	Ni		Pd		Pt
S(1)-Ni-S(2)	91.36(11)	S(1)-Pd-S(2)	88.62(5)	S(1)-Pt-S(2)	88.19(4)
S(3)-Ni-S(4)	92.99(11)	S(3)-Pd-S(4)	90.35(5)	S(3)-Pt-S(4)	90.32(5)
S(1)-Ni-S(3)	88.12(7)	S(1)-Pd-S(3)	90.64(3)	S(1)-Pt-S(3)	90.85(4)
S(1)-Ni-S(4)	174.14(7)	S(1)-Pd-S(4)	176.24(4)	S(2)-Pt-S(4)	90.85(4)
S(2)-Ni-S(3)	174.14(7)	S(2)-Pd-S(3)	176.24(4)	S(2)-Pt-S(3)	176.39(3)
S(2)-Ni-S(4)	88.12(7)	S(2)-Pd-S(4)	90.64(3)	S(1)-Pt-S(4)	176.39(3)
C(1)-S(1)-Ni	106.2(2)	C(1)-S(1)-Pd	105.15(12)	C(1)-S(1)-Pt	105.98(11)
C(2)-S(2)-Ni	106.2(2)	C(2)-S(2)-Pd	105.15(12)	C(2)-S(2)-Pt	105.98(11)
C(12)-S(3)-Ni	103.7(2)	C(12)-S(3)-Pd	102.15(12)	C(19)-S(3)-Pt	102.13(10)
C(11)-S(4)-Ni	103.7(2)	C(11)-S(4)-Pd	102.15(12)	C(20)-S(4)-Pt	102.13(10)

Table 3.12: Selected angles of [M(Bz<sub>2</sub>pipdt)(mnt)] (M(II) = Ni, Pd, Pt).

The benzyl residues of the Bz<sub>2</sub>pipdt ligand in the three complexes are oriented in an up-and-down fashion conferring to the molecules a propeller-like shape. As reported in Table 3.11, the M-S bond distances involving the mnt ligand are slightly shorter than those originating from Bz<sub>2</sub>pipdt whereas the C-S bond distances are longer as predictable according to the *push/pull* nature of the ligands.

In the Raman spectra the peaks relating to CC stretching vibrations of mnt are observed at 1472 cm<sup>-1</sup>, 1496 and 1489 cm<sup>-1</sup> for Ni, Pd and Pt respectively (See Figure 3.9) suggesting a prevailing dithiolate character for mnt increasing from Ni to Pd-Pt.



---

**Figure 3.9:** Raman spectra of [Pt(Bz<sub>2</sub>pipdt)(mnt)].

## Chapter 3

---

The crystal packing of [Ni(Bz<sub>2</sub>pipdt)(mnt)] shows that the molecules are stacked in an antiparallel arrangement and these stacks are approximately aligned along the *c* axis (see Figure 3.10).

The Ni(II) atoms are interposed between two nitrogen atoms of symmetry related ligands ( $d[\text{Ni-N}(1)] = 3.741(6) \text{ \AA}$ ), whereas the S(1) sulfur atom lies  $\sim 3.74 \text{ \AA}$  above the C(1)-C(1) bond. Within the stacks, the N(2) nitrogen atoms of the mnt ligands are oriented towards the C(2) carbon atoms of the ethylene fragment of the Bz<sub>2</sub>pipdt ligands, thus generating a layer that is parallel to the *bc* plane.

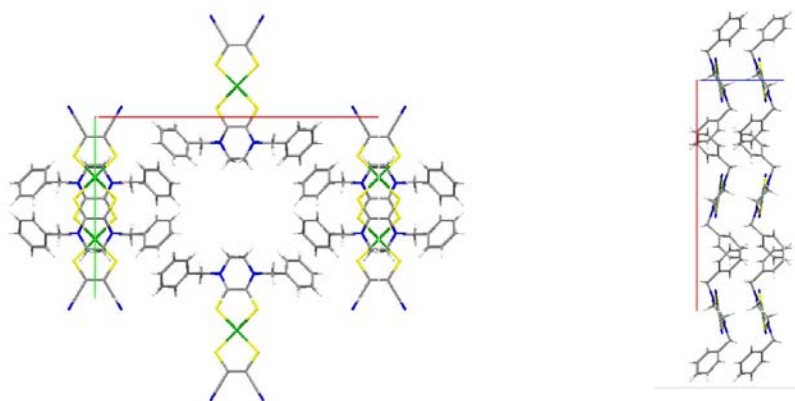
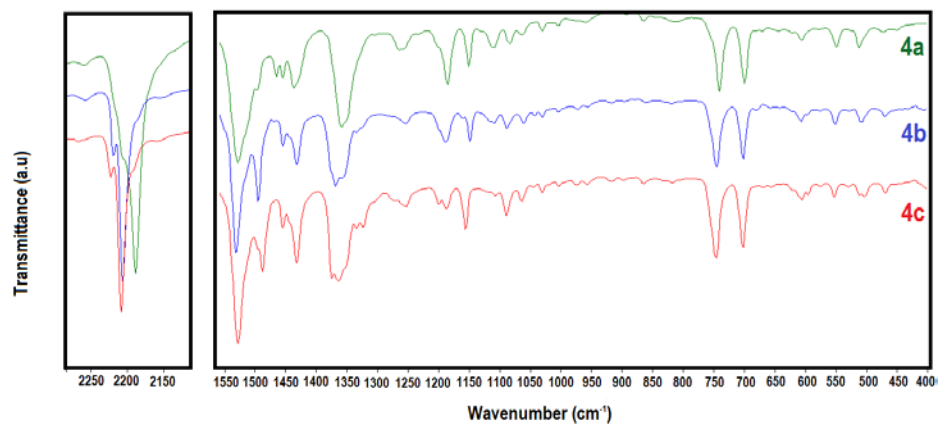


**Figure 3.10:** View of the crystal lattice of [Pd(Bz<sub>2</sub>pipdt)(mnt)].

The layers interact with each other by means of partial  $\pi$  interaction between the aromatic rings of the Bz<sub>2</sub>pipdt ligands. In fact, only the C(8) and C(9) carbon atoms are located at an interacting distance with symmetry related ones ( $\sim 3.68 \text{ \AA}$ ). Despite the fact that **4a** and **4c** crystallize in two different

space group, the crystal packing of both compounds are very similar. In fact also **4c** exhibits layers formed by antiparallel molecules stacked along the *c* axis. The Pt(II) atom is located between symmetry related N(1) nitrogen atoms ( $d[\text{Pt-N}(1)] = 3.788(3) \text{ \AA}$ ). The major difference between the two crystal packing resides in the orientation of the benzyl moieties of **4c** when compared to that of **4a**. In fact, in **4c**, adjacent layers present the aromatic rings that are roughly perpendicular to each other and showing the C(6)-H group that points toward the centroid of a symmetry related aromatic ring. In addition, within each layer, two antiparallel stacked complex molecules exchange two CH- $\pi$  interactions by means of the C(7) and C(9) carbon atoms ( $d[\text{C}(7)\text{-C}(9)] = 3.721(6) \text{ \AA}$ ).

The vibrational spectra of the complexes are in agreement with structural findings. Vibrations relating to the common Bz<sub>2</sub>pipdt group are found approximately at the same wavenumbers for the triad (the typical C-N vibrations of the thioamidic groups are observed as strong peaks in the IR at 1528 (Ni); 1531 (Pd) and 1528 (Pt) cm<sup>-1</sup>, while the most significant peaks relating to mnt show some differences between Ni, Pd and Pt. In particular  $\nu(\text{CN})$  and  $\nu(\text{CC})$  stretching vibrations are found at 2187 and 1464 cm<sup>-1</sup> (Ni) and at 2205 and 1495 cm<sup>-1</sup> (Pd) 2206 and 1487 cm<sup>-1</sup> (Pt) (see Figure 3.11).

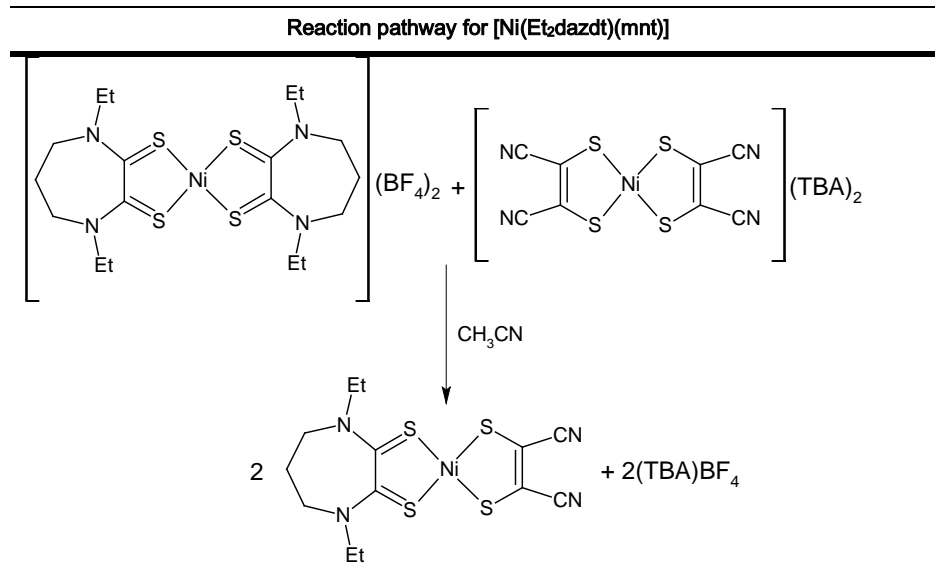


---

**Figure 3.11:** Vibrational spectra of [M(Bz<sub>2</sub>pipdt)(mnt)].

### 3.4.3 Synthesis of $M(\text{Et}_2\text{dazdt})(\text{mnt})$ ( $M(\text{II}) = \text{Ni}, \text{Pd}, \text{Pt}$ )

In the case of Ni both the cationic and anionic complexes are available as precursors. The dropwise addition of a  $\text{CH}_3\text{CN}$  solution of  $[\text{Ni}(\text{Et}_2\text{dazdt})_2](\text{BF}_4)_2$  to a  $\text{CH}_3\text{CN}$  solution of  $(\text{Bu}_4\text{N})_2[\text{Ni}(\text{mnt})_2]$  in 1:1 ratio, produces in an almost quantitative yield. On slow evaporation of the solvents, well formed green crystals precipitate.



**Scheme 3.4:** Synthetic route for  $[\text{Ni}(\text{Bz}_2\text{pipdt})(\text{mnt})]$ .

In the case of Pd and Pt the mixing of salts of the symmetrical precursors affords CT double salts (see supplementary A3 in Appendix). Instead mixed

## Chapter 3

---

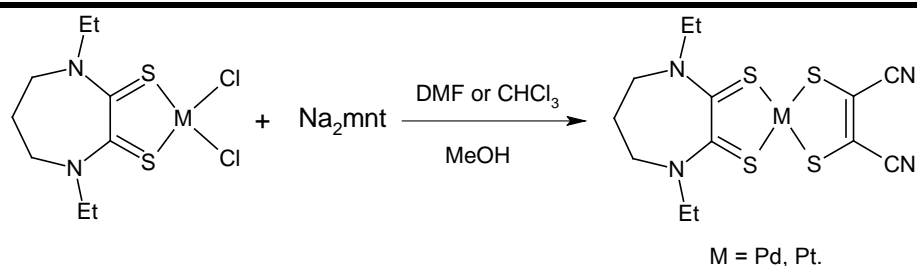
ligand Pd and Pt complexes are obtained reacting  $[M(\text{Et}_2\text{dazdt})\text{Cl}_2]$  with maleonitriledithiolato dianion.

$[M(\text{Et}_2\text{dazdt})\text{Cl}_2]$  is prepared following a modification of the pathway reported in paragraph 3.2.1.

---

### Reaction pathway for $[\text{Pd}(\text{Et}_2\text{dazdt})(\text{mnt})]$ and $[\text{Pt}(\text{Et}_2\text{dazdt})(\text{mnt})]$

---



---

**Scheme 3.5:** Synthetic route for **5b** and **5c**

Due to solubility reasons, reaction with  $[\text{Pd}(\text{Et}_2\text{dazdt})\text{Cl}_2]$  is carried out in  $\text{CH}_3\text{Cl}$ , whereas, in the case of  $[\text{Pt}(\text{Et}_2\text{dazdt})\text{Cl}_2]$ , DMF is used as solvent.

### 3.4.4 Structural characterization

Crystals of  $[\text{Pt}(\text{Et}_2\text{dazdt})(\text{mnt})]$  have been obtained as dark-green needles by slow diffusion of diethyl ether into a saturated solution of **5c** in DMF. X-ray diffractometric characterization of this crystal show that **5c** crystallizes in the monoclinic  $C2/c$  space group (see table 3.13).

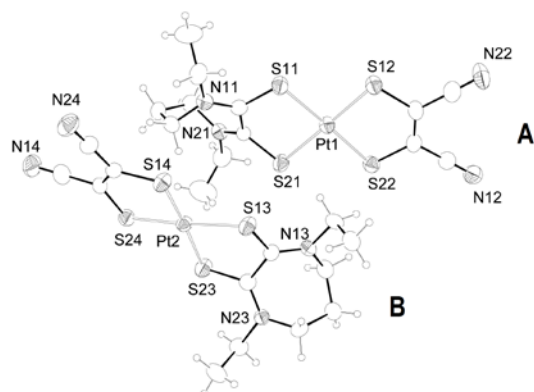


**Figure 3.12:** A projecting of [Pt(Et<sub>2</sub>dazdt)(mnt)].

In the unit cell, two independent molecular entities are present, which differ in the orientation of the ethyl substituents with respect to the epta-atomic ring. In one molecule (**A**) the ethyl groups are iso-oriented whereas in the other (**B**) they point in opposite directions (see Fig. 3.12).

Again the central Pt atom is coordinated by four S atoms in a square planar environment with Pt–S bonds ranging from 2.2635(19)–2.23078(19) Å (see Table 3.13).

The Pt–S bond lengths are similar in value to those previously published for other “push-pull” coordination complexes. Crystallographic parameters are reported in Tables 3.13.



Crystallographic data for [Pt(Et <sub>2</sub> dazdt)(mnt)]	
Empirical formula	C <sub>26</sub> H <sub>32</sub> N <sub>8</sub> Pt <sub>2</sub> S <sub>8</sub>
Formula weight	1103.26
Crystal size (mm)	0.45 x 0.20 x 0.08
Crystal system	Triclinic
Space group	P-1
a, b, c (Å)	8.994(2), 9.354(2), 22.146(6)
α, β, γ (deg.)	89.73(1), 87.22(2), 66.29(1)
V (Å <sup>3</sup> )	1857.5(7)
Z	2
T (K)	293(2)
ρ(calc) (Mg/m <sup>3</sup> )	1.973
μ (mm <sup>-1</sup> )	8.003
θ range (deg.)	0.84 to 27.20
No. of rflcn/obsv >4σ(F)	21833/8132
• GooF	1.004
• R1 [a]	0.0694
• wR2 [b]	0.0857

**Table 3.13:** Summary of X-ray crystallographic data for **5c**. [a] R1 =  $\sum ||F_o| - F_c| / \sum F_o$ ; [b] wR2 =  $[\sum [w(F_o^2 - F_c^2)^2] / \sum [w(F_o^2)^2]]^{1/2}$ ,  $w = 1 / [\sigma^2(F_o^2) + (aP)^2 + bP]$ , where  $P = [\max(F_o^2, 0) + 2F_c^2] / 3$ .

Selected bond distances and angles are given in Tables 3.14.

Bond lengths (Å) and Angle (deg.) of [Pt(Et <sub>2</sub> dazdt)(mnt)]			
Pt-S(22)	2.2990(2)	C(32)- N(12)	1.131(9)
Pt-S(12)	2.2635(19)	S(22)-Pt-S(12)	91.05(7)
Pt-S(11)	2.2688(18)	S(22)-Pt-S(11)	178.18(6)
Pt-S(21)	2.3078(19)	S(12)-Pt-S(11)	90.42(7)
S(11)- C(11)	1.709(7)	S(22)-Pt-S(21)	89.35(7)
S(21)- C(21)	1.704(7)	S(12)-Pt-S(21)	178.56(8)
C(11)- C(21)	1.477(9)	S(11)-Pt-S(21)	89.21(7)
S(12)- C(12)	1.756(7)	C(22)-S(22)-Pt	101.9(3)
S(22)- C(22)	1.746(7)	C(11)-S(11)-Pt	102.6(2)
C(11)- C(12)	1.343(9)	C(12)-S(12)-Pt	101.6(2)
C(42)- N(22)	1.135(9)	C(21)-S(21)-Pt	100.4(2)

Table 3.14: Selected bond and angle for 5c.

The seven membered ring of the ligand adopts a “twist” conformation with a pseudo two-fold axis passing through the middle point of the C(1)–C(2) bond and the C(3) atom. The torsion angle N(1)-C(11)-C(21)-N(2) of 43,8° confirm the nonplanarity of the ring. (see Figures 3.13 and 3.14)

## Chapter 3

---

### View of the crystal lattice of [Pt(Et<sub>2</sub>dazdt)(mnt)]

---

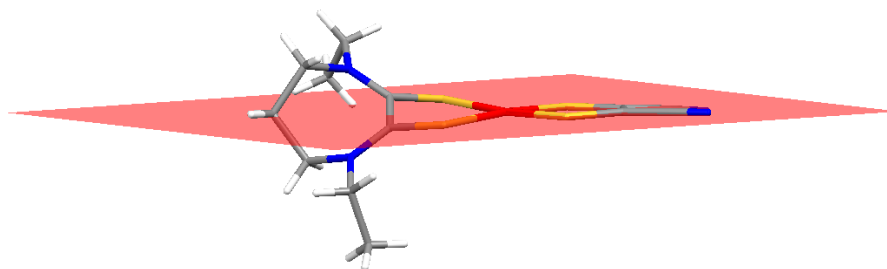


**Figure 3.13:** Torsion angle of [Pt(Et<sub>2</sub>dazdt)(mnt)]

The comparison between the seven member ring for the complex [Pt(Et<sub>2</sub>dazdt)(mnt)] and six member ring for the [Pt(iPr<sub>2</sub>pipdt)(mnt)] is shown in figure 3.14.

### View of the crystal lattice of [Pt(Et<sub>2</sub>dazdt)(mnt)]

---

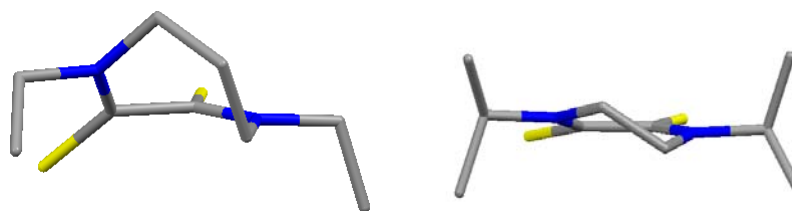


**Figure 3.14:** Comparison between (Et<sub>2</sub>dazdt) ring and (iPr<sub>2</sub>pipdt) ring.

Figure 3.15 shows that, in the crystal lattice, the complex units are almost parallel and head-to-tail with respect to each other. The complex molecules

form an irregular layer in the  $ac$  plane. The interaction between C-CN fragment of adjacent molecules is around 3.6 Å.

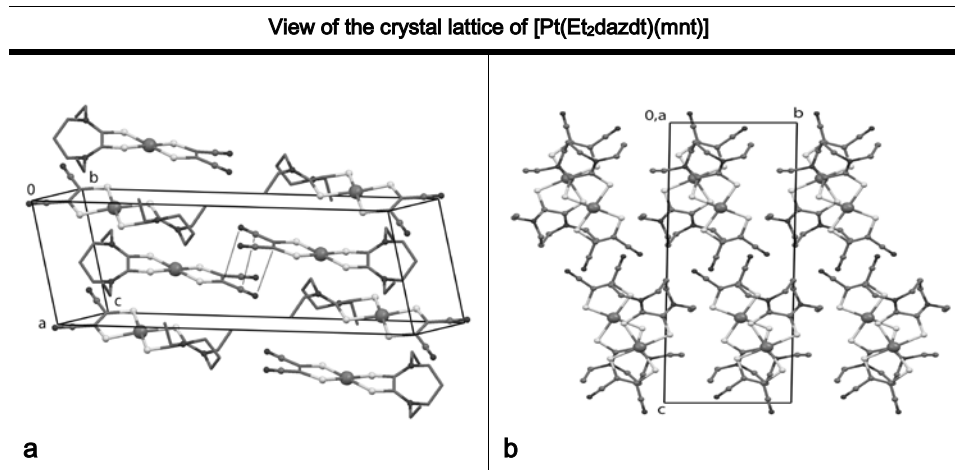


**Figure 3.15:** a) Crystal packing of [Pt(Et<sub>2</sub>dazdt)(mnt)] projected along the  $ac$  axis; b) Crystal packing of [Pt(Et<sub>2</sub>dazdt)(mnt)] projected along the  $a$  axis.

### 3.4.5 Electrochemistry

Cyclic voltammetric data for both  $[M(\text{Bz}_2\text{pipdt})(\text{mnt})]$  and  $[M(\text{Et}_2\text{dazdt})(\text{mnt})]$  complexes are presented in Table 3.15. Cyclic voltammetric experiments performed on DMF solutions of the complexes show that **4a**, **4b** and **4c** are redox active and exhibit two *quasi* reversible reduction waves and one irreversible oxidation wave at potentials. Since **5a** is not stable in DMF solutions, CV data are reported for **5b** and **5c** only. Also in this case two quasi-reversible reduction waves and one irreversible oxidation are found

Cyclic Voltammetric Data of  $[M(X)(Y)]$  ( $X = \text{Bz}_2\text{pipdt}$ ,  $\text{Et}_2\text{dazdt}$ ;  $Y = \text{mnt}$ ) complexes

Complex	$E_a$ (V) <sub>a</sub>	$E^{1/2}$ (V)	$E^{2/2}$ (V)
	$M(X)(Y)^0 \leftrightarrow M(X)(Y)^+ + e^-$	$M(X)(Y)^0 + e^- \leftrightarrow M(X)(Y)^-$	$M(X)(Y)^- + e^- \leftrightarrow M(X)(Y)^{2-}$
<b>[Ni(Bz<sub>2</sub>pipdt)(mnt)]</b>	+1.09	-0.39	-0.90
<b>[Pd(Bz<sub>2</sub>pipdt)(mnt)]</b>	+1.20	-0.35	-0.84
<b>[Pt(Bz<sub>2</sub>pipdt)(mnt)]</b>	+1.08	-0.37	-0.87
<b>[Ni(Et<sub>2</sub>dazdt)(mnt)]</b>	n.a	n.a	n.a
<b>[Pd(Et<sub>2</sub>dazdt)(mnt)]</b>	+1.04	-0.46	-0.78
<b>[Pt(Et<sub>2</sub>dazdt)(mnt)]</b>	+0.96	-0.42	-0.79

**Table 3.15:** Cyclic Voltammetric data  $[M(\text{Bz}_2\text{pipdt})(\text{mnt})]$  and  $[M(\text{Et}_2\text{dazdt})(\text{mnt})]$  complexes

[M(Bz<sub>2</sub>pipdt)(mnt)] and [M(Et<sub>2</sub>dazdt)(mnt)] were each studied by cyclic voltammetry in a solution of 0.1 M TBABF<sub>4</sub> in DMF (see Fig 3.16).

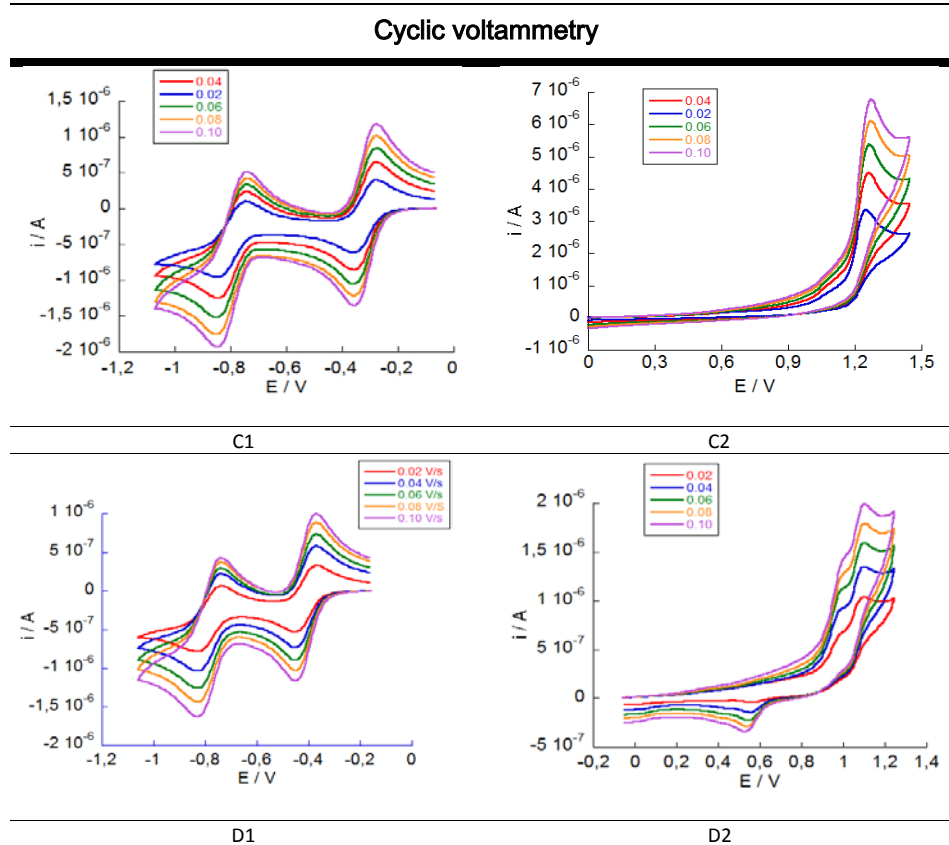


**Figure 3.16:** Cyclic voltammetry in 0.1 M TBABF<sub>4</sub>/DMF, measuring current ( $i$ ), in response to an applied potential ( $E$ ): (A1-B1) several scan (different scan rate  $\text{mVs}^{-1}$ ) of **4c** and **5c**, showing two reversible redox reduction processes; (A2-B2) several scan (different scan rate  $\text{mVs}^{-1}$ ) of **4c** and **5c**, showing one irreversible redox oxidation processes.

### 3.5 Experimental Details

*Chemicals.* All the reagents and solvents were purchased from Aldrich and used without further purification

**Pd(Bz<sub>2</sub>pipdt)(dmit)** (**2b**). (t-Bu<sub>4</sub>N)<sub>2</sub>[Pd(dmit)<sub>2</sub>] (50 mg) in 25cm<sup>3</sup> of CH<sub>3</sub>CN (green solution) was added drop-wise to a dark red suspension of [Pd(Bz<sub>2</sub>pipdt)](Cl)<sub>2</sub> (27 mg) in 25cm<sup>3</sup> CH<sub>3</sub>CN, under stirring and reflux. After one day a dark green solid was formed (28 mg ; yield: 85%). This solid was filtered, washed with diethyl ether and then dried. Well formed crystals suitable for X-ray crystallography have been obtained through re-crystallization from DMF/diethyl ether. **CHNS:** Found (Calcd for C<sub>21</sub>H<sub>18</sub>N<sub>2</sub>PdS<sub>7</sub>) C% 39.77 (40.09), H% 2.48 (2.88), N% 4.42 (4.45) S% 34.99 (35.67). **FT-IR spectrum** (cm<sup>-1</sup>) 3099w, 2921w, 2850w, 1616s, 1512m, 1455m, 1387m, 1357m, 1189m, 1156w, 1115m, 1065vs, 1028w, 900w, 732m, 695m, 611w, 513w, 470w.

**[Pt(Bz<sub>2</sub>pipdt)(dmit)]** (**2c**). Following a similar procedure (t-Bu<sub>4</sub>N)<sub>2</sub>[Pt(dmit)<sub>2</sub>] (80 mg) in 25cm<sup>3</sup> of CH<sub>3</sub>CN, green solution, was added dropwise to a dark red suspension of [Pt(Bz<sub>2</sub>pipdt)](Cl)<sub>2</sub> (51 mg) in 25 cm<sup>3</sup> CH<sub>3</sub>CN). The obtained crude dark green solid(55 mg ; yield: 90%) gave for recrystallization well formed crystals. **CHNS:** Found (Calcd for C<sub>21</sub>H<sub>18</sub>N<sub>2</sub>PtS<sub>7</sub>) C% 35.47 (35.14), H% 2.50 (2.53), N% 3.97 (3.90) S% 30.16 (31.26). **FT-IR spectrum** (KBr pellets; cm<sup>-1</sup>) 3021w, 2921w, 2853w, 1526vs, 1452m, 1420m, 1354vs, 1307w, 1257m, 1203w, 1179w, 1072vs, 1028w, 910w, 893w, 739m, 722w, 698m, 672w, 517w, 470w.

**[Pd(*i*Pr<sub>2</sub>pipdt)(dmit)] (3b).** (t-Bu<sub>4</sub>N)<sub>2</sub>[Pd(dmit)<sub>2</sub>] (48,32 mg) in 25cm<sup>3</sup> of CH<sub>3</sub>CN, green solution, was added dropwise to [Pd(*i*Pr<sub>2</sub>pipdt)](Cl)<sub>2</sub> (22,58 mg) in 25 cm<sup>3</sup> CH<sub>3</sub>CN, dark red suspension, under stirring. The solution became dark green after immediately. After refluxed for 24h, a precipitate formation was observed. The dark green precipitate was filtered, washed with diethyl ether and then dried. Recrystallization from DMF/ diethyl ether (yield: 87%) **CHNS:** Found (Calcd for C<sub>13</sub>H<sub>18</sub>N<sub>2</sub>PdS<sub>7</sub>) C% (29,28), H% (3,40), N% (5,25) S% (42,10). **FT-IR spectrum** (cm<sup>-1</sup>) 2928vw, 2206vs, 2187vw, 1635m, 1528vs, 1497vw, 1464w, 1454w, 1437m, 1357m, 1263w, 1184m, 1149w, 1109w, 1081w, 862vw, 738m, 698m, 605vw, 574w, 548w, 511w, 471w.

**[Pt(*i*Pr<sub>2</sub>pipdt)(dmit)] (3c).** (t-Bu<sub>4</sub>N)<sub>2</sub>[Pt(dmit)<sub>2</sub>] (109,29mg) in 25cm<sup>3</sup> of CH<sub>3</sub>CN, green solution, was added dropwise to [Pt(*i*Pr<sub>2</sub>pipdt)](Cl)<sub>2</sub> (69,27mg) in 25 cm<sup>3</sup> CH<sub>3</sub>CN, dark red suspension, under stirring. The solution became dark green after immediately. After refluxed for 24h, a precipitate formation was observed. The dark green precipitate was filtered, washed with diethyl ether and then dried. Recrystallization from DMF/ diethyl ether (yield: 94%) **CHNS:** Found (Calcd for C<sub>13</sub>H<sub>18</sub>N<sub>2</sub>PtS<sub>7</sub>) C% 25,39 (25.11); H% 2,46 (2,92); N% 4,50 (4,51); S% 39,14 (36,09). **FT-IR spectrum** (cm<sup>-1</sup>) 2967vw, 2927vw, 1645vs, 1508vs, 1428vs, 1378m, 1356m, 1276w, 1251w, 1240w, 1190w, 1108s, 1049s, 1024s, 904m, 720w, 587w, 511w, 475w.



**[Ni(Bz<sub>2</sub>pipdt)(mnt)] (4a)**: yellow MeOH solution of K<sub>2</sub>mnt (33.72 mg, 0.14 mmol in 25 cm<sup>3</sup>) was added drop-wise to a blue MeOH solution of [Ni(Bz<sub>2</sub>pipdt)Cl<sub>2</sub>] (62.40 mg, 0.14 mmol in 25 cm<sup>3</sup>) under stirring. The solution became dark-green and was allowed to react under reflux for 24 hours. A dark-green solid was formed, filtered, washed with diethyl ether and dried, obtaining 61.81 mg (94% yield). The obtained solid consisted in well formed crystals, which can be also obtained through recrystallisation from CH<sub>3</sub>CN/Et<sub>2</sub>O. Analytical results are in accordance with the formula [Ni(Bz<sub>2</sub>pipdt)(mnt)]. **CHNS**: Found (Calcd for C<sub>22</sub>H<sub>18</sub>N<sub>4</sub>NiS<sub>4</sub>) C% 50.25 (50.30); H% 3.57 (3.45); N% 10.46 (10.66); S% 22.81 (24.41). **FT-IR spectrum** (cm<sup>-1</sup>) 2928vw, 2206vs, 2187vw, 1635m, 1528vs, 1497vw, 1464w, 1454w, 1437m, 1357m, 1263w, 1184m, 1149w, 1109w, 1081w, 862vw, 738m, 698m, 605vw, 574w, 548w, 511w, 471w. **Raman spectra** (cm<sup>-1</sup>) 2192s, 1538w, 1472vs, 1305m, 1295w, 1296m, 1191s, 1120s, 511m, 346m, 337m.

**[Pd(Bz<sub>2</sub>pipdt)(mnt)] (4b)**: As described for **4a**, [Pd(Bz<sub>2</sub>pipdt)(mnt)] has been similarly obtained by reacting K<sub>2</sub>mnt (31.80, mg 0.13 mmol in MeOH 25 cm<sup>3</sup>) with [Pd(Bz<sub>2</sub>pipdt)Cl<sub>2</sub>] (66.10 mg 0.13 mmol in 25 cm<sup>3</sup> in DMF solution, obtaining 72.40 mg of a blue precipitate (yield 96%). The crude product was filtered, washed with Et<sub>2</sub>O and recrystallized from CH<sub>3</sub>CN/Et<sub>2</sub>O, following dissolution in CH<sub>3</sub>CN with a Soxhlet extractor. Analytical results are in accordance with the formula [Pd(Bz<sub>2</sub>pipdt)(mnt)]. **CHNS**: Found (Calcd for C<sub>22</sub>H<sub>18</sub>N<sub>4</sub>NiS<sub>4</sub>) C% 44.87 (46.11); H% 3.09 (3.17); N% 9.53 (9.78); S% 21.41 (22.38). **FT-IR spectrum** (cm<sup>-1</sup>) 2990vw, 2218vw, 2204vs, 1621m, 1531vs, 1494vw, 1454w, 1431m, 1367m, 1356m, 1253w, 1188m, 1147w, 1107w,

1087m, 860vw, 744m, 700m, 605vw, 574w, 549w, 507w, 468w. **Raman spectra** ( $\text{cm}^{-1}$ ) 2347vw, 2209w, 1940vw, 1524s, 1496vs, 1436vw, 1322w, 1275m, 1191m, 1115w, 1105w, 528m, 353s, 149m.

**[Pt(Bz<sub>2</sub>pipdt)(mnt)] (4c)**. 62.03 mg (0.10 mmol) of [Pt(Bz<sub>2</sub>pipdt)Cl<sub>2</sub>] in 25 cm<sup>3</sup> DMF and 25.80 mg 0.10 mmol of K<sub>2</sub>mnt in 25 cm<sup>3</sup> MeOH). A green-blue precipitate (56.13 mg) formation was observed immediately. The precipitate was filtered, washed with Et<sub>2</sub>O and recrystallised from CH<sub>3</sub>CN/Et<sub>2</sub>O. Yield: 94%; analytical results are in accordance with the formula [Pt(Bz<sub>2</sub>pipdt)(mnt)]. **CHNS**: Found (Calcd for C<sub>22</sub>H<sub>18</sub>N<sub>4</sub>PtS<sub>4</sub>) C% 39.71 (39.93); H% 2.64 (2.74); N% 8.34 (8.47); S% 19.20 (19.38). **FT-IR spectrum** ( $\text{cm}^{-1}$ ) 2918, 2224, 2206, 1527, 1487, 1431, 1454, 1373, 1362, 1252, 1187, 1156, 1105, 1087, 864, 744, 700, 603, 574, 551, 502, 467 **Raman spectra** ( $\text{cm}^{-1}$ ) 2209vw, 1521m, 1489vs, 1433w, 1318m, 1303w, 1293vw, 1275m, 1192s, 1120m, 1047w, 1005w, 972w, 529m, 405w, 374m, 154w.

**Ni(Et<sub>2</sub>dazdt)(mnt) (5a)** [Ni(Et<sub>2</sub>dazdt)<sub>2</sub>](BF<sub>4</sub>)<sub>2</sub> (118 mg, 0.37 mmol) was dissolved in CH<sub>3</sub>CN (25 cm<sup>3</sup>) and (t-Bu<sub>4</sub>N)<sub>2</sub>[Ni(mnt)<sub>2</sub>] in CH<sub>3</sub>CN (20 cm<sup>3</sup>) was added dropwise. The mixture was refluxed for 10 min, yielding a deep green solution and a dark-blue precipitate. The precipitate was removed by centrifugation and to the filtrate. The crude product was recrystallised from CH<sub>3</sub>CN/ET<sub>2</sub>O. Yield: 90 mg, 91.7%. Analytical results are in accordance with the formula [Ni(Et<sub>2</sub>pipdt)(mnt)]. **CHNS**: Found (Calcd for C<sub>13</sub>H<sub>26</sub>N<sub>4</sub>NiS<sub>4</sub>) C% 36.70 (37.60); H% 3.67 (3.88); N% 13.09 (13.49); S% 29.34 (30.88). **FT-IR spectrum** ( $\text{cm}^{-1}$ ) 2976 w, 2934 w, 2870 w, 2803 s, 1523 vs, 1491 m, 1456 m, 1443 m, 1363 m, 1363 w, 1344 w, 1289 w, 1236 w, 1153 w, 1123 w, 984 w, 789 w, 735 w, 509 w. **DR spectrum** (KBr, nm) 817, 607, 412, 305.

**Pd(Et<sub>2</sub>dazdt)(mnt) (6b)** Complex [Pd(Et<sub>2</sub>dazdt)Cl<sub>2</sub>] (79,2 mg, 0.21 mmol) was dissolved in DMF (20 cm<sup>3</sup>) and Na<sub>2</sub>mnt (37,45 206 mg, 0.21 mmol) was added dropwise in MeOH (10 cm<sup>3</sup>) under stirring for 30 min (50°C). The MeOH was rotary-evaporated and a green precipitate formation was observed immediately after added of diethyl ether. The precipitate was removed by centrifugation and to the filtrate. The crude product was recrystallised from DMF/Et<sub>2</sub>O. Yield: 80,78 mg, 86,7 %. Analytical results are in accordance with the formula [Pd(Et<sub>2</sub>dazdt)(mnt)]. **CHNS:** Found (Calcd for C<sub>13</sub>H<sub>16</sub>N<sub>4</sub>PdS<sub>4</sub>) C% 33.43 (33.73); H% 3.67 (3.48); N% 13.09 (12.10); S% 27.47 (27,10). **FT-IR spectrum** (cm<sup>-1</sup>) 2356 m, 2336 m, 2200 m, 1526 s, 1456 m, 1385 s, 1362 w, 1148 w, 1123 w, 982 w, 789 w, 679 w, 509 w. **DR spectrum** (KBr, nm) 669, 487, 375, 270.

**Pt(Et<sub>2</sub>dazdt)(mnt) (6c)** This compound was prepared as described for **6b** starting from [Pt(Et<sub>2</sub>dazdt)Cl<sub>2</sub>] (70,00 mg; 0.14 mmol) in DMF and Na<sub>2</sub>mnt (27,5 mg; 0.14 mmol) in MeOH. Yield: 73,74 mg, 89.92%. **CHNS:** Found (Calcd for C<sub>13</sub>H<sub>16</sub>N<sub>4</sub>PtS<sub>4</sub>) C% 28.18 (40.89); H% 2.80 (2.99); N% 9.88 (8.30); S% 22.58 (18.95). **FT-IR spectrum** (cm<sup>-1</sup>) 2939 w, 2368 w, 2338 w, 2203 s, 1520 vs, 1454 s, 1364 s, 1344 m, 1285 s, 1238 s, 1155 s, 1121 w, 982 w. **DR spectrum** (KBr, nm) 700, 560, 380, 230

**Pt(Bz<sub>2</sub>pipdt)(dcbdt) (7)**. (Bu<sub>4</sub>N)<sub>2</sub>[Pt(dcbdt)<sub>2</sub>] (25,74 mg) in 25cm<sup>3</sup> of CH<sub>3</sub>CN (green solution) was added drop-wise to a dark red suspension of [Pt(Bz<sub>2</sub>pipdt)](Cl)<sub>2</sub> (16,50 mg) in 25cm<sup>3</sup> CH<sub>3</sub>CN, under stirring and reflux. After one day a blue solid was formed (17,82 mg ; yield: 89%). This solid

## Synthesis and characterisation

---

was filtered, washed with diethyl ether and then dried. Well formed crystals suitable for X-ray crystallography have been obtained through re-crystallization from DMF/diethyl ether.

---

# Chapter 4

*Optical Properties*

An L-shaped decorative line consisting of a vertical line on the left and a horizontal line on the bottom, both extending from the left edge of the page towards the right.

## 4.1 Introduction to second-order NLO materials

Non-linear optics represents the optical phenomenon, by which, after the interaction of an oscillating electromagnetic field (light) with specific molecules or bulk materials, a new electromagnetic wave (new light) is generated, which differs from the incident one not only in the frequency, but also in the phase or other optical properties<sup>[40,41]</sup>.

The interaction of an electromagnetic field with matter induces a polarization in the matter. In linear optics there is an instantaneous displacement (polarization) of the electron density of an atom by the electric field  $E$  of the light wave. The displacement of the electron density away from nucleus results in a charge separation (an induced dipole), with moment,  $\mu$ <sup>[40-42]</sup>.

With small fields, the strength of the applied fields is proportional to the displacement of charge from equilibrium position, and leads to the relation:

$$Polarization = \vec{\mu} + \alpha\vec{E} \quad \text{Eq. 4.1}$$

Where  $\alpha$  is the linear polarizability of the molecular atom.

When the applied electromagnetic field is interacting with a single molecule, the molecule's polarizability can change and be driven beyond the linear regime. Therefore, the now nonlinear molecular polarization is expressed by Eq. (4.2):

$$\vec{P} = \mu_0 + \alpha\vec{E} + \beta\vec{E}^2 + \gamma\vec{E}^3 + \dots \quad \text{Eq. 4.2}$$

where  $\mu_0$  is the molecular ground state electric dipole moment,  $\alpha$  the linear polarizability,  $\beta$  and  $\gamma$  the quadratic and cubic hyperpolarizabilities, respectively. The intensity of the emission decreases by increasing the order; usually above the third-order it is too low to observe a significant effect. In conclusion, non-linearity is a secondary process of emission of light related to the intensity of the incident light and to the electronic properties controlling the polarizability of molecules or of bulk materials.

Second order nonlinear optical effects occur when two incident waves, with  $\omega$  frequency interact with the molecule or the bulk material, characterized by a given value of quadratic hyperpolarizability ( $\beta$ ), a new wave or Second Harmonic (SH), with doubled frequency ( $2\omega$ ) is produced (see Fig. 4.1)<sup>[41]</sup>.

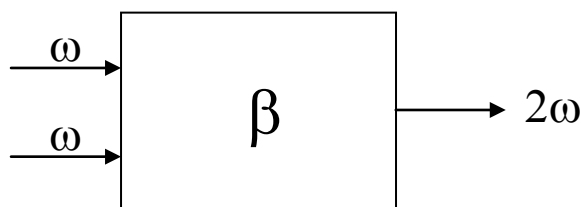


**Fig. 4.1:** Second Harmonic Generation (SHG).

To obtain molecular materials displaying significant second order NLO effects it is necessary to have high values of the molecular quadratic hyperpolarizability  $\beta$ .

In 1977, Oudar<sup>[43]</sup> produced a theoretical interpretation of the electronic origin of  $\beta$  and therefore of the main electronic factors acting on SHG, thus

providing a simple model for the design of second-order NLO molecular materials. Since NLO properties are related to the polarizability of the electrons under the effect of the electric field  $\vec{E}$  of the light, second-order NLO properties are dependent on electronic transitions with high charge-transfer character. Oudar assumed that in asymmetric NLO chromophores the second-order NLO response is dominated mainly by one major charge-transfer process, so that it is possible to infer that:

$$\beta_{zzz} = \frac{3}{2h^2c^2} \frac{v_{eg}^2 r_{eg}^2 \Delta\mu_{eg}}{(v_{eg}^2 - v_L^2)(v_{eg}^2 - 4v_L^2)} \quad \text{Eq 4.3}$$

where  $z$  is the direction of the charge-transfer,  $v_{eg}$  ( $\text{cm}^{-1}$ ) the frequency of the charge-transfer transition,  $r_{eg}$  its transition dipole moment,  $\Delta\mu_{eg}$  is the difference between the excited state and ground state molecular dipole moment ( $\mu_e - \mu_g$ ) and  $v_L$  is the frequency of the incident radiation.

The Eq. (4.3) is based on the so-called “two state” model, a simple way to estimate from spectroscopic data the frequency dependent quadratic hyperpolarizability  $\beta_{zzz}$  or  $\beta_{CT}$ , when a single charge-transfer dominates the NLO response.

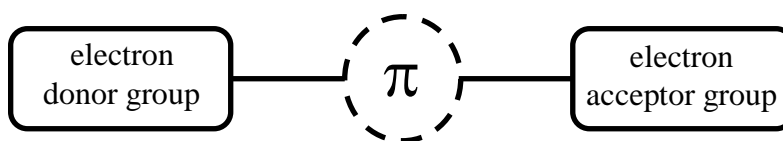
Extrapolation to zero frequency ( $v_L=0.0\text{eV}$ ;  $\lambda=\infty$ ) allows estimation of the static quadratic hyperpolarizability  $\beta_0$ , useful figure of merit to evaluate the basic second-order NLO properties of a molecular material, according to Eq. 4.4:



$$\beta_0 = \beta_\lambda \left[ 1 - \left( \frac{2\lambda_{\max}}{\lambda} \right)^2 \right] \left[ 1 - \left( \frac{\lambda_{\max}}{\lambda} \right)^2 \right] \quad \text{Eq 4.4}$$

where  $\beta_\lambda$  is the quadratic hyperpolarizability value at  $\lambda$  incident wavelength and  $\lambda_{\max}$  is the absorption wavelength of the considered charge-transfer transition<sup>1</sup>.

According to the two state model, molecules that possess large  $\beta$  values contain an electron Donor group connected to an electron Acceptor through a  $\pi$ -bridging moiety (see scheme 4.2)<sup>[40]</sup>.



**Scheme 4.2:** Scheme of a push-pull chromophore

Such polarizable molecules are characterized by low-energy Donor/Acceptor intramolecular Charge-Transfer transition. This kind of arrangement will give rise to a non-centrosymmetric molecule. In addition large  $\Delta\mu_{eg}$  and  $r_{eg}$  are required in order that large  $\beta$ -values are produced.

Suitable metal complexes can work as second-order NLO chromophores and if compared to organic chromophores, they can offer some favourable

<sup>1</sup> The first hyperpolarisability,  $\beta$ , can be expressed in either the cgs ( $\text{cm}^4 \text{statvolt}^{-1} = \text{esu}$ ) or the SI ( $\text{C}\cdot\text{m}^3\cdot\text{V}^{-2}$ ) unit systems. The conversion from the SI to the cgs system is given by the relation:  $10^{-50} \text{C}\cdot\text{m}^3\cdot\text{V}^{-2} = 2.694 \times 10^{-30} \text{esu}$ .

conditions such as increased stability, the introduction of additional functionality (for example introduction paramagnetic ions) etc.

In particular in  $d^8$  metal dithione-dithiolato complexes, the electronwithdrawing/donating properties of the two ligands may be tuned by variation of the substituents at the dithiolene core. These complexes are characterized by low energy excited states with excited-state dipole moments significantly different from their respective ground-state values. This will provide a substantial contribution to hyperpolarizabilities. They have great possibilities for redox changes, a property largely associated with the nature of the bonding in these complexes.

In addition to the electron features at molecular level described, the obtained products are required to crystallize in an acentric-crystal structure or to be incorporated into appropriate bulk arrangement in such a way that the NLO-properties are preserved<sup>[6]</sup>.

#### 4.1.2 Techniques for Measuring SHG in molecular materials

A variety of experimental techniques have been used for investigating the second-order NLO activity of molecular materials. The molecular first hyperpolarisability can be obtained by the *electric field induced second harmonic generation* (EFISH) technique and is useful for neutral, dipolar molecules. This technique allows the determination of the  $\mu\beta$  dot product when an electric field is applied to a solution of an NLO-active species. The  $\mu\beta$  value, *i.e.*, the vector component of the  $\beta_{ijk}$  tensor along the dipole

moment direction, can be thus extracted if the ground-state dipole moment,  $\mu_g$ , is known<sup>[44]</sup>. The schematic diagram of the setup for an EFISH experiment is reported in Appendix A4.

Alternatively, the *hyper-Rayleigh scattering* (HRS) technique involves detecting the incoherently scattered second harmonic generated from an isotropic solution and allows the determination of the 'whole'  $\beta$  tensor, or more exactly, the mean value of the  $\beta \times \beta$  tensor product. Analysis of the polarisation dependence of the second harmonic signal can provide information about single tensor  $\beta_{ijk}$  components. This method has the advantage that it can be used even for nondipolar or charged molecules. Frequency dependent  $\beta$ (EFISH) or  $\beta$ (HRS) values are eventually extrapolated to static  $\beta_0$  ones by means of the two-level model discussed above [eqns. 4.3 and 4.4]. In fact, the static hyperpolarisability represents the most important feature when comparing the molecular second-order NLO response of different chromophores. However, these estimated  $\beta_0$  data are generally approximate, especially when dynamic  $\beta$  data are resonantly enhanced or when the two-level model breaks down, that is, when many states, instead of one, contribute to NLO response. The above SOS method and the related two-state simplification represent, however, the most useful approaches for chemists to understand structure–hyperpolarisability relationships, in order to design new, highly efficient second-order NLO molecular materials<sup>[45]</sup>.

## 4.2 Optical studies

The d<sup>8</sup> mixed-ligand complexes based on push (R<sub>2</sub>pipdt or R<sub>2</sub>dazdt) and pull ligands (dmit, mnt) are characterized by an absorption of medium intensity in the Vis-NIR region of the spectrum. This absorption can be assigned to the HOMO→LUMO transition which has charge-transfer character<sup>[6]</sup>. In table 4.1 a summary of optical data are collected.

Complex		$\lambda_{\text{max}}$ (nm)	$\epsilon \times 10^{-3}$ (M <sup>-1</sup> cm <sup>-1</sup> )	$\mu\beta$ (10 <sup>-48</sup> esu)	$\mu\beta_0$ (10 <sup>-48</sup> esu)
[Ni(Bz <sub>2</sub> pipdt)(dmit)]	(2a)	858	10.6	-6000	-926
[Pd(Bz <sub>2</sub> pipdt)(dmit)]	(2b)	819	11.3	-5360	-1160
[Pt(Bz <sub>2</sub> pipdt)(dmit)]	(2c)	827	14.8	-10000	-2011
[Ni( <sup>i</sup> Pr <sub>2</sub> pipdt)(dmit)]	(3a)	829	12.1	-6200	-1218
[Pd( <sup>i</sup> Pr <sub>2</sub> pipdt)(dmit)]	(3b)	753	3.2	-6200	-1316
[Pt( <sup>i</sup> Pr <sub>2</sub> pipdt)(dmit)]	(3c)	790	13.3	-7350	-1909
[Ni(Bz <sub>2</sub> pipdt)(mnt)]	(4a)	751(660sh)	1.3	-1436	-463
[Pd(Bz <sub>2</sub> pipdt)(mnt)]	(4b)	651(560sh)	4.3	-1450	-684
[Pt(Bz <sub>2</sub> pipdt)(mnt)]	(4c)	685	10.1	-1950	-822
[Ni(Et <sub>2</sub> dazdt)(mnt)] <sup>a</sup>	(5a)	817	1.9	n.a.	n.a
[Pd(Et <sub>2</sub> dazdt)(mnt)]	(5b)	666	2.0	-400	-177
[Pt(Et <sub>2</sub> dazdt)(mnt)]	(5c)	679	2.4	-1300	-576

<sup>a</sup> Since **5a** is not stable in DMF, absorption spectra have been recorded in CH<sub>3</sub>CN solution.

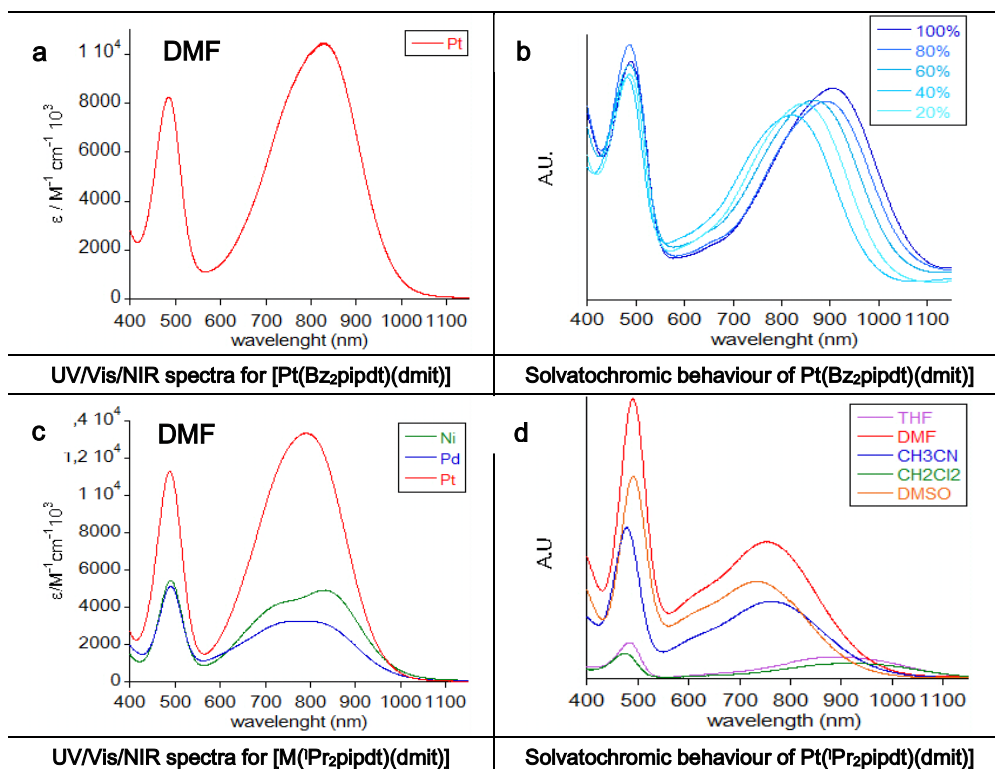
**Table 4.1:** Absorption maxima of compounds in DMF solution

In Figures 4.1 and 4.2, the electronic absorption spectra of the complexes in DMF solution are shown, moreover the solvatochromic behavior of the low-energy peak of Pt derivatives for each triads are reported.

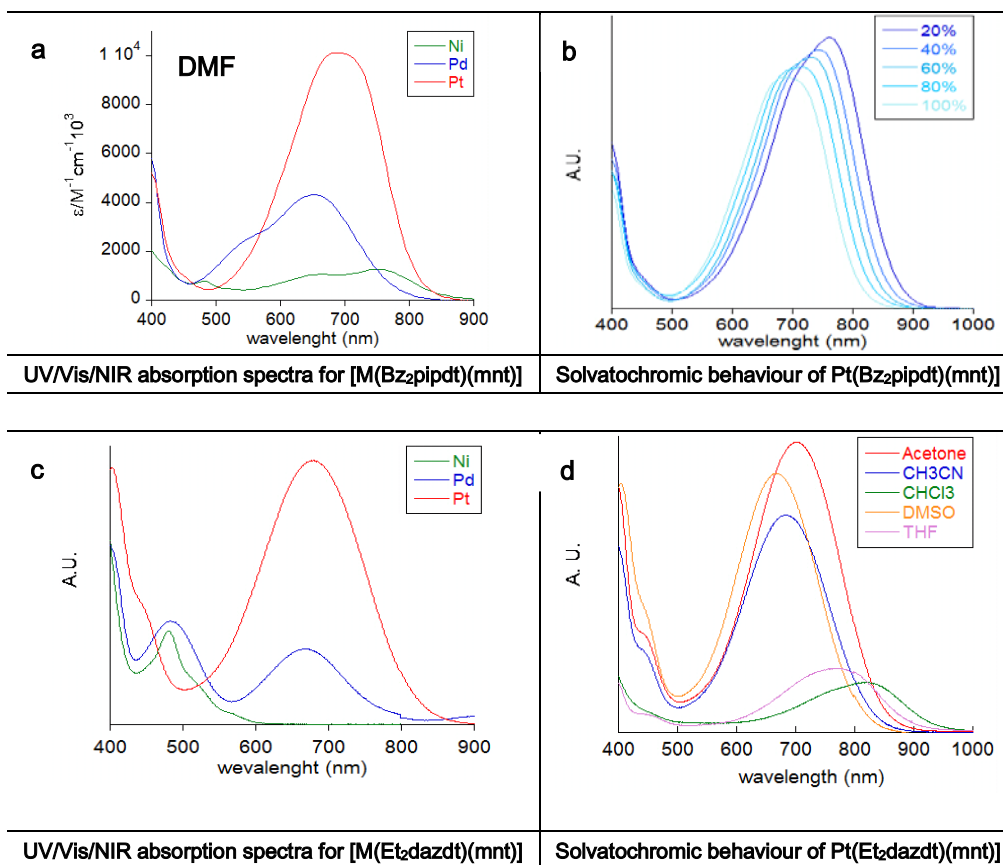
In the case of **2c** and **4c**, spectra were monitored for complexes' solutions with different ratio of DMF/CS<sub>2</sub> mixtures. Negative solvatochromism was found for low energy band on going from the DMF 100% solution to the 20% solution. In Appendix A5 the spectra of the other complexes are reported. Similar behavior has been observed in **3c** and **5c**.

Inspection of table 4.1 allows to point out:

- 1) The metal affects the energy of the CT band following the order  $\lambda_{\max}$  Pd < Pt < Ni.
- 2) The comparison of optical properties in complexes bearing the same metal and push ligand but varying the pull one, shows that the energy of the CT peak increases with the pull character (for example, in DMF solution, in the case of [Pt(Bz<sub>2</sub>pipdt)(L)], the CT band is found, respectively at: 827 nm for L = dmit; nm for L = 812 dsit ; 711 nm for L = dcbdt and 685 nm for L=mnt).
- 3) On the other hand in complexes bearing the same metal and pull ligand, the variation of the push ligand affects the energy of the CT peak which increases with the push character (for example, in DMF solution, in the case of [Pt(L)(mnt)], the CT band is found, respectively at: 685 nm for L = Bz<sub>2</sub>pipdt and 679nm for Et<sub>2</sub>dazdt).



**Figures 4.1:** Vis/NIR absorption spectra: (a) **2c** in DMF; (b) **2c** in DMF/CS<sub>2</sub> mixtures ranging from DMF 100% to 20%; (c) M(<sup>i</sup>Prpipdt)(dmit) in DMF; (d) of **3c** in the range of solvents shown in figure.



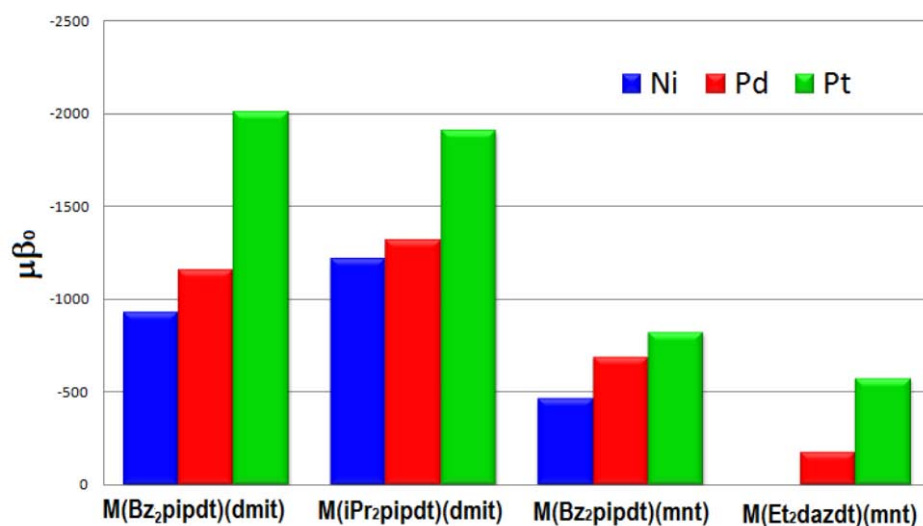
**Figures 4.2:** Vis/NIR absorption spectra: (a) of  $[M(\text{Bz}_2\text{pipdt})(\text{mnt})]$  in DMF; (b) of **4c** in DMF/CS<sub>2</sub> mixtures ranging from DMF 100% to 20%; (c) of  $[M(\text{Et}_2\text{dazdt})(\text{mnt})]$  in DMF; (d) of **5c** in the range of solvents shown in figure.

TD-DFT calculations have been performed on the [M(Bz<sub>2</sub>pipdt)(mnt)] triad to assign the observed transitions.

It is confirmed that the most intense absorption band in the low energy region and mostly due to the HOMO → LUMO transition has a mixed-metal-ligand-to-ligand charge transfer band character (MMLL'CT) [47,48,49]. This band is accompanied by a second one, which appears either as a shoulder in the high energy edge or just widens the main band. The contribution of MMLL'CT character to the main band is predominant (~83% in **3b** and **3c**) but it is not unique. A different behavior is observed in the case of the nickel compound. In fact in **3a** the main band shows a stronger multiconfigurational character, since two transitions contribute to the final state population. These are the HOMO→LUMO (mixed-metal-ligand-to-ligand character) and the HOMO→LUMO+2 (ligand-to-metal character). The strong shoulder present in the high energy side is calculated to own an analogous character to the main band. (see Appendix for more details).

The molecular quadratic optical non linearities, collected in Table 4.1, were determined by the EFISH technique. The used set up allows the determination of the scalar product  $\mu\beta$  ( $\mu$  = the dipole moment;  $\beta$  = the vector part of the quadratic hyperpolarizability tensor). In Graphic 4.1, the nonlinear optical data ( $\mu\beta_0$ ) of the complexes are compared.





**Graphic 4.1:** Nonlinear optical data of [M(Bz<sub>2</sub>pipdt)(dmit)], [M(iPr<sub>2</sub>pipdt)(dmit)], [M(Bz<sub>2</sub>pipdt)(mnt)] and [M(Et<sub>2</sub>dazdt)(mnt)] triade.

This comparison provides a pictorial view which allows to point out the most promising second-order NLO chromophores among the investigated compounds and inside the d<sup>8</sup> metal triad.

Accordingly it can be pointed out that:

- Pt(II) complexes have enhanced  $\mu\beta_0$  values when compared to corresponding complexes of Ni(II) and Pd(II).
- Complexes with dmit ligand exhibit enhanced  $\mu\beta_0$  values when compared to corresponding mnt ones;
- Data retrievable from EFISH measurements on some compounds investigated, seem to suggest that pipdt derivatives have enhanced NLO properties when compared to dazdt ones. For example, the  $\mu\beta_0$

value for [Pt(**Bz<sub>2</sub>pipdt**)(mnt)] ( $\mu\beta_0 = -822 \cdot 10^{-48} \text{esu}$ ), is significantly larger than that for [Pt(**Et<sub>2</sub>dazdt**)(mnt)] ( $\mu\beta_0 = -822 \cdot 10^{-48} \text{esu}$ ). However the limited number of cases investigated so far does not allow to draw reliable conclusions.

- R-substituents at the N-atoms of pipdt ring have smaller influence on the electronic properties of complexes. However they significantly affect the solid state properties. This is important to favour  $\pi$ - $\pi$  interactions.

The comparison of  $\mu\beta_0$  collected in Table 4.1 with literature data available so far suggests that these complexes exhibit negative second order polarizabilities, larger than those exhibited on the well known class  $d^8$  metal diimide dithiolate complexes<sup>[27,46]</sup>.

Cummings et al.<sup>[27]</sup> have reported the optimized second order efficiency for the palladium and platinum diimine dithiolate complexes shown below.

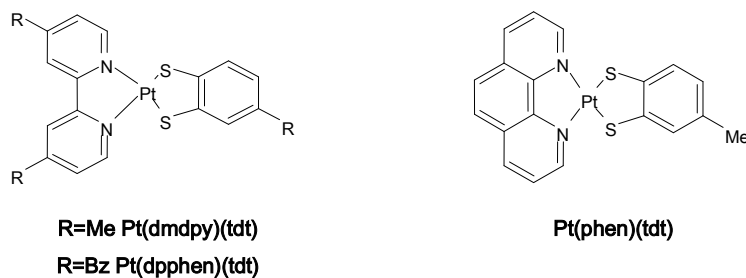


**Figure 4.8:** Selected examples of second order NLO chromophores

Second NLO Polarizabilities of Literature M(diimine)(dithiolate) complexes				
	$\lambda_{\max}$ ( $\epsilon$ )	$\mu$ (Debye)	$\beta_{\mu}(10^{-30}$ esu)	$\beta_0$
Pt(dmbpy)(tdt)	563 (7000)	9	-25	-15
Pt(phen)(tdt)	583 (7000)	9	-28	-16
Pt(dpphen)(tdt)	538 (4500)	9	-6	-4

**Table 4.2:** Experimental Molecular First Hyperpolarizability for some diimine-dithiolato complexes.

As shown by inspecting Table 4.2 the values  $\mu\beta_0$  for diimine-dithiolate complexes (with tdt donor ligand)<sup>[27]</sup> are lower than those found for dithione-dithiolate.

Optical data and dipole analysis on d<sup>8</sup> mixed-ligand dithiolene complexes previously obtained are reported in Table 4.3.

	$\lambda_{\max}$ (nm)	$\epsilon \times 10^{-3}$ (M <sup>-1</sup> cm <sup>-1</sup> )	$\mu_d$ (Debye)	$\beta_0 \times 10^{-30}$ (Esu)
Ni(Pr <sub>2</sub> pipdt)(dmit)	965	10.9	13	-130
Ni(EH <sub>2</sub> pipdt)(mnt)	829*	9.8*	16*	-37*
Ni(Pr <sub>2</sub> timdt)(mnt)	883	24.1	16	~0

\*Calculated values for the Ni complex with the H substituted piperazine ligand. (EH =2-ethylhexyl).

**Table 4.3:** Molecular First Hyperpolarizabilities for some diimine-dithiolato compounds.

A different NLO response is observed for push-pull unsymmetrical dithiolenes depending on the nature of the push ligand (five-membered (1,3-R<sub>2</sub>timdt), six-membered (1,4-R<sub>2</sub>pipdt) or epta-membered ring

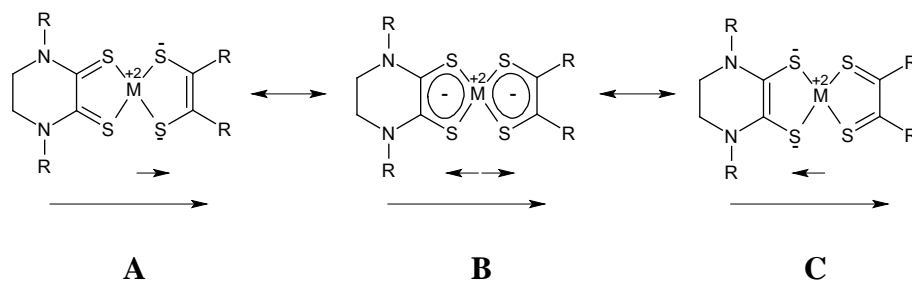
(1,4-R<sub>2</sub>dazdt) band the pull ligand (dmit, mnt). In particular, on varying the push ligand:

- a) in the case of [Ni(1,3-*i*-Pr<sub>2</sub>timdt)(mnt)] an almost null  $\beta_0$  value accompanied by a large dipole moment of the ground state, related to the presence of the dipole arising from the periphery of the molecule is observed; no variation of the dipole moment occurs due to the extensive  $\pi$ -delocalization inside the C<sub>2</sub>S<sub>2</sub>MC<sub>2</sub>S<sub>2</sub> core. ( ground state B in scheme 4.1 );
- b) for complexes with six membered and epta-membered push ligands a negative  $\beta_0$  with a comparable dipole moment of the ground state is found.

As far as the pull ligand is concerned, in the case of complexes with the dmit ligand the value of hyperpolarizability is higher than that of complexes with mnt ligand.

Chen and coworkers<sup>[25]</sup> ascribed the different behavior of unsymmetrical complexes to the  $\pi$ -localized (dithione–dithiolato) or overall  $\pi$ -delocalized (dithiolenes) nature of electron distribution. Two dipoles can be identified for the localized and delocalized forms:

- one arising from the periphery of the molecule (from the donor to the acceptor substituents);
- the other one originating from the metal to the dithiolato sulfurs, when the resonance form **A** is prevalent in the ground state.



Scheme 4.1

While the first component will remain essentially unchanged, the second dipole component will change upon excitation due to the charge-transfer transition from the dithiolate to the dithione ligand. Instead, in the case of 6complexes with a nearly symmetrical charge distribution at the  $(C_2S_2)M(S_2C_2)$  core, also the second component will remain almost unchanged.

DFT calculations on model compounds in figure 4.9, where hydrogen atoms replace the alkyl groups of 1,4- $R_2$ pipdt, provided more insight to explain the peculiarity of dmit ligands, in providing high values of second order NLO activity to these complexes

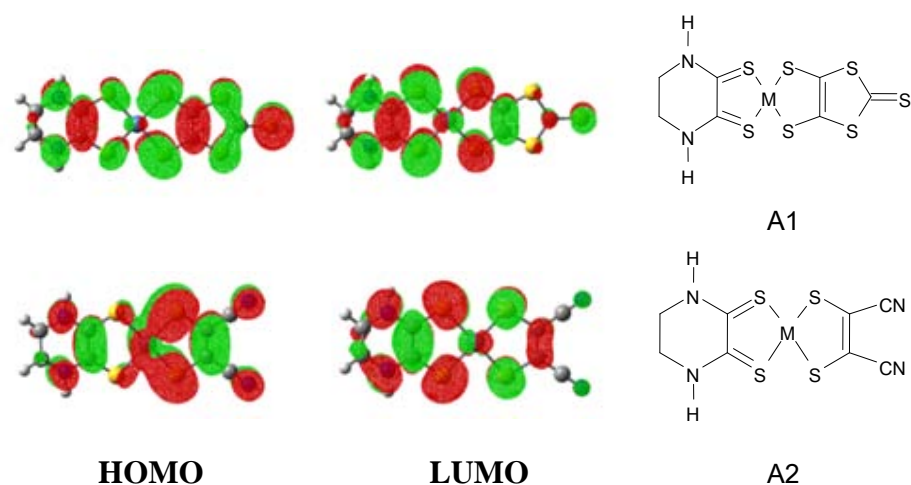


**Figure 4.9:** Frontier orbitals of model complexes A1–A2, where hydrogen atoms replace the alkyl groups of ligands 1,4-R<sub>2</sub>pipdt.

Analysis of the calculated first molecular hyperpolarizabilities and their components with the two-state approximation accounts for the various NLO responses in terms of the important following components: the transition dipole moment between the first excited and the ground states ( $\mu_{ge}^2$ ), the difference between the dipole moment of the ground and of the excited state ( $\mu$ ) and the energy of the absorption band. The derived picture highlights the different roles of the two push and pull ligands, but also the peculiar perturbation of the  $\pi$ -electron density induced by the terminal CS<sub>3</sub> group of the dmit ligand, which induces major differences between the ground and excited states. Similarly to symmetric complexes, the HOMOs and LUMOs of the models A1-A2 are still **i.p.** and **o.o.p.** combinations of the critical C<sub>2</sub>S<sub>2</sub>

frontier  $\pi$ -orbital but the atomic contributions are now unbalanced, particularly when the ligand 1,4-H<sub>2</sub>pipdt is present. In fact, the greater weight of the latter in the LUMO is evident from comparison of the HOMO and LUMO drawings of A1 and A2. Another important aspect is the scarce contribution of the terminal CS<sub>3</sub> moiety of dmit to the LUMO of the complex A1. Thus while the  $\rho_{\pi}$  orbital populations change more at the core than at the peripheral atoms, the terminal S atom of the dmit ligand is significantly less populated in the excited state. Therefore, also the dipole component arising from the periphery of the molecule will change upon excitation. The unique role of dmit ligand in perturbing the electron distribution at the dithiolene core and in inducing major differences between the ground and excited states explains the peculiarity of mixed-ligand complexes based on dmit. This shows that the simplifying assumption, that the variation of the dipolar component arising from the periphery of the molecule upon excitation is constant, is not generally applicable, and that mixed-ligand complexes based on dmit seem promising optimal candidates to induce NLO properties at the molecular level<sup>[6]</sup>.

These results on model complexes are in accordance with experimental results. Further theoretical studies are in progress to better understand the role of the ligands and of the metal.

Preliminary results on the [M(Bz<sub>2</sub>pipdt)(mnt)] triad are reported below.

As expected, the pull ligand (dithiolate, maleonitriledithiolate) contributes mostly to the HOMO and the push ligand (dithione, 1,4-dibenzylpiperazine-2,3-dithione) mostly to the LUMO.

The metal orbitals contribution to both HOMO and LUMO is not identical for the three compounds being most relevant in the case of platinum followed by nickel.

This trend can be attributed to the better metal–ligand overlap induced by the 5*d*-orbitals of Pt along with its contracted coordination sphere compared to 4*d*- of Pd and 3*d*-orbitals of Ni. Furthermore, **3c** owns the more delocalized highest occupied and lowest unoccupied orbitals along the series, followed by **3a** and **3b**.

An apparent discrepancy between the observed and calculated energy sequence of the low energy absorption is found. In fact while the calculated HOMO-LUMO gap in the gas phase, increases in the order: Pd < Ni < Pt, the experimental sequence follows the order  $\lambda_{\text{max}}$  Ni < Pt < Pd, putting Pd at the top of the list.



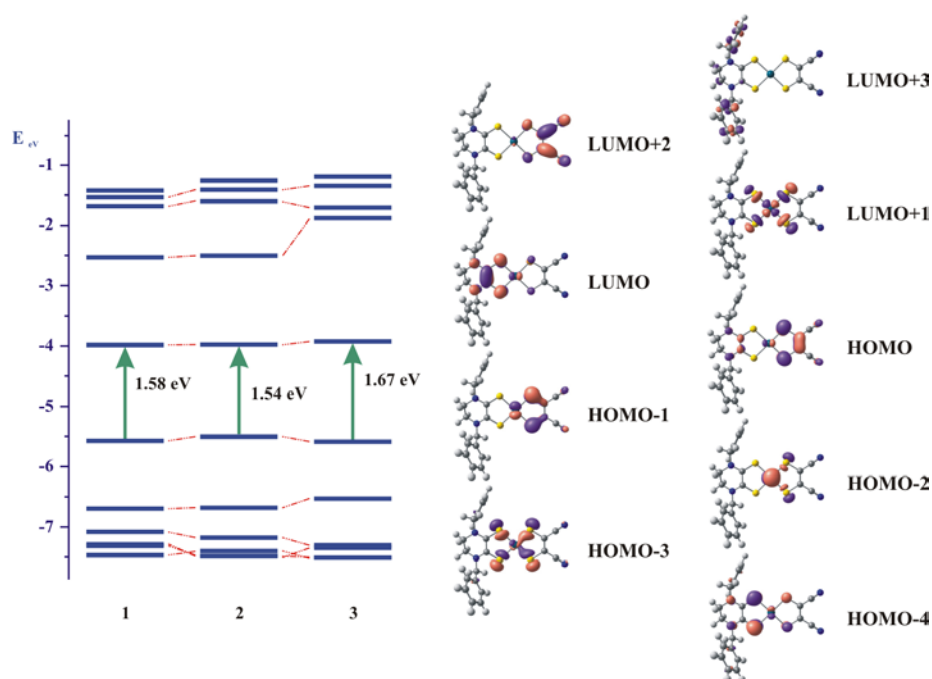


**Figure 4.10:** Energy level diagram of **3a** and **3c** along with 0.05 a.u. contour plots of the frontier orbitals of **3b**.

Further theoretical studies have shown that this difference can be ascribed to solvent and that the palladium complex should be the most affected by the *solvent-solute* interactions along the series, due to higher difference between in ground and excited state dipole moments<sup>[47]</sup>.

Further calculations worked out considering different polar solvent (acetonitrile and dimethylsulfoxide) are in agreement with the experimental trend. (see Appendix A6).

We observe that employing a polar solvent, which causes a relatively high electric field, enhances the HOMO-LUMO gap. This is true for all three compounds under study, and in the case of DMSO, the relative energy order becomes Pd > Pt  $\approx$  Ni. In other words the palladium compound, which owns the largest charge separation in the ground state is affected the most, as expected (*vide supra*).

In particular the effect of the polar solvent interaction is to stabilize heavily those orbitals that are localized on the dithiolate, and to destabilize those of dithione.

Moreover solvation seems to have a further impact on frontier orbital's character.

MO	E <sub>ev</sub>	Bz <sub>2</sub> pipdt	M	mnt	MO	E <sub>ev</sub>	Bz <sub>2</sub> pipdt	M	Mnt
<b>Ni(Bz<sub>2</sub>pipdt)(mnt)</b>									
<i>Unoccupied</i>					<i>Occupied</i>				
<b>64b</b>	-3.51	93.0	3.5	3.4	<b>63b</b>	-5.70	15.0	19.8	65.2
<b>Pd(Bz<sub>2</sub>pipdt)(mnt)</b>									
<i>Unoccupied</i>					<i>Occupied</i>				
<b>64b</b>	-3.47	93.8	2.8	3.5	<b>63b</b>	-5.72	9.7	12.3	78.0
<b>Pt(Bz<sub>2</sub>pipdt)(mnt)</b>									
<i>Unoccupied</i>					<i>Occupied</i>				
<b>64b</b>	-3.47	91.1	4.0	4.9	<b>63b</b>	-5.67	16.2	17.1	66.7

**Table 4.4:** Contribution of different fragments to complexes valence orbitals. HOMO and LUMO orbitals are shown.

From Table 4.4, we observe that within the followed model, dithione's character in LUMO is raised at dithiolate's expense, while metal

contribution in HOMO is also raised at dithione's expense. In other words, frontier orbitals in all compounds under study become more localized in polar solvents and as a result, an enhancement in the properties that are related to the main charge transfer band should be expected.

These changes that are expected to become more prominent in polar solvents as compared to non polar ones would have an impact in the visible spectra side features of these complexes, expressed mainly through changes in the character of the transitions that lie higher in energy.

**3a**'s HOMO is the most stabilized along the relative series and this fact is illustrated by its more positive  $E_{ox}$ . On the other hand, the almost identical piperazine contribution to LUMOs would lead to almost equal first reduction potentials for the three complexes, which is found to be the case. Changes in orbital's energy ordering from the gas phase (and in non polar solvents, if soluble) to DMSO field are pictorially depicted in Figure 4.11.

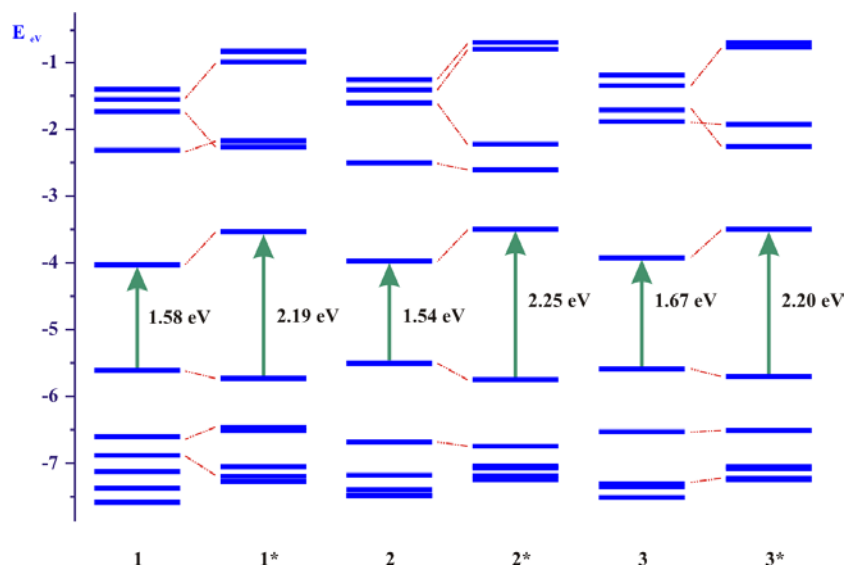


**Figure 4.11:** Energy level diagram that depicts the relation between the orbitals calculated in the gas phase with the ones calculated within the CPCM approximation employing DMSO as the solvent. The latter are denoted with the asterisk.

### 4.3 Spectroelectrochemistry

The peculiar redox activity and optical properties of these complexes prompted us to perform spectroelectrochemistry experiments to investigate the optical properties of the reduced species.

Electrochemistry can yield information about the potential at which a redox reaction occurs and its reversibility can not provide further data to the electrogenerated species<sup>[50,51]</sup>. The combination of reaction-oriented electrochemistry with species-focussed spectroscopy in what has become known as Spectroelectrochemistry (**SEC**)<sup>[51-55]</sup> can often solve this problem. Typical spectroscopy methods in spectroelectrochemistry include absorption spectroscopy in the ultraviolet (**UV**), the visible (**VIS**), the near-infrared (**NIR**) or the infrared (**IR**) region<sup>[52-54]</sup>.

In contrast to these essentially physical spectroscopic methods, which are well suited for species characterization, electrochemistry provides the advantage (and complication) of being a time dependent chemical process occurring at an interface, typically between a solution (electrolyte) and a solid (electrode). Typically, the spectroscopic response is monitored in situ while the electrochemistry reaction is carried out under controlled conditions. The construction design of spectroelectrochemical cells, can exhibit various degrees of sophistication<sup>[8]</sup>.

Metal dithiolenes have been shown to have multiple redox states, with distinct absorption properties and, as such, are particularly suited to be investigated by this technique. In section 3.2 the fundamentals of

electrochemistry have been discussed. For in situ analysis, several modifications must first be made to the electrochemical setup in order that the absorption properties can be studied. The most common technique for spectroelectrochemical analysis is Optically Transparent Thin Layer Electrochemistry (OTTLE) (for more details see Appendix A7), and it is this that shall be considered in this thesis. In the first instance, OTTLE provides a relatively simple method for in situ analysis<sup>[57]</sup>.

Through the study of the oxidised and reduced species information on the nature of the frontier orbitals can be obtained.

The change in absorption spectrum of **2b** upon reduction was studied in both 0.1 M TBABF<sub>4</sub>/DMF (Figure 4.5). In DMF the CT bands were seen to decrease in intensity and gradually one new bands grew in. Isosbestic points were maintained between the initial and final spectra.

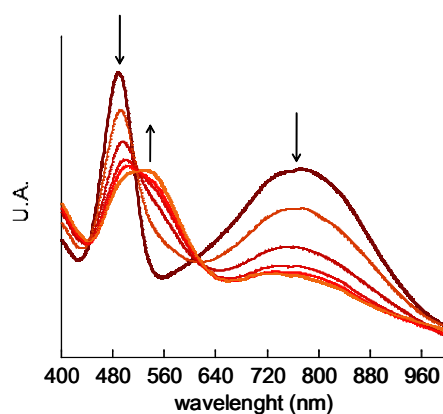


**Figure 4.5:** Spectroelectrochemical reduction of **2b**. Study carried out in 0.1 M TBABF<sub>4</sub>/DMF, at -40 °C, with an applied potential of -0.6 V (vs. Ag/AgCl).

A similar behaviour was observed for **2c**.

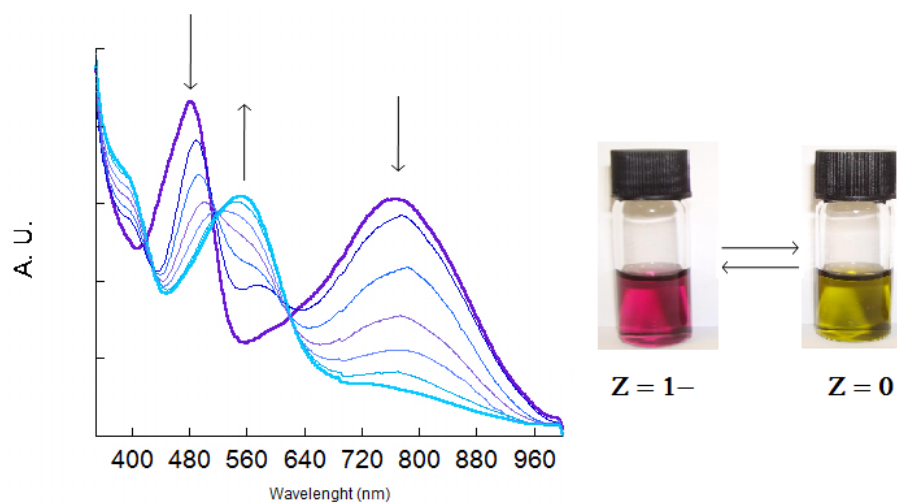


**Figure 4.6:** Spectroelectrochemical reduction of **2c**. Study carried out in 0.1 M TBABF<sub>4</sub>/DMF, at -40 °C, with an applied potential of - 0.6 V (*vs.* Ag/AgCl). Arrows indicate the growth or reduction of an absorption band with reduction.

The mono-reduced species shows collapse of the CT bands followed by the growth of new bands in their place. The  $\pi$ - $\pi^*$  intraligand band at about 560nm no completely collapses after oxidation.

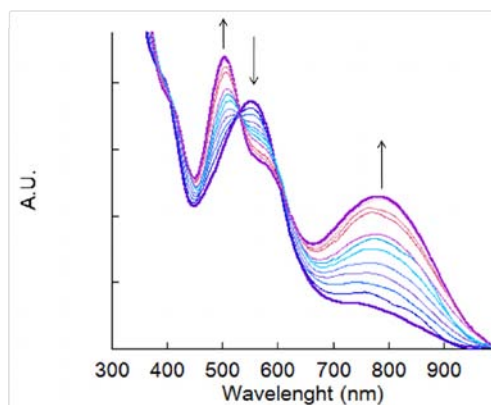


**Figure 4.7:** Spectroelectrochemical oxidation of **2c**. Study carried out in 0.1 M TBABF<sub>4</sub>/DMF, at -40 °C, with an applied potential of + 0.1 V (vs. Ag/AgCl). Arrows indicate the growth or reduction of an absorption band with oxidation.

In conclusion spectroelectrochemical experiments show that the solvatochromic peak of these complexes is reversibly bleacheable for mono-reduction.

Due their joint electrochemical and NLO-properties these complexes seem promising candidates for applications in redox-switching of molecular first hyperpolarizability.



---

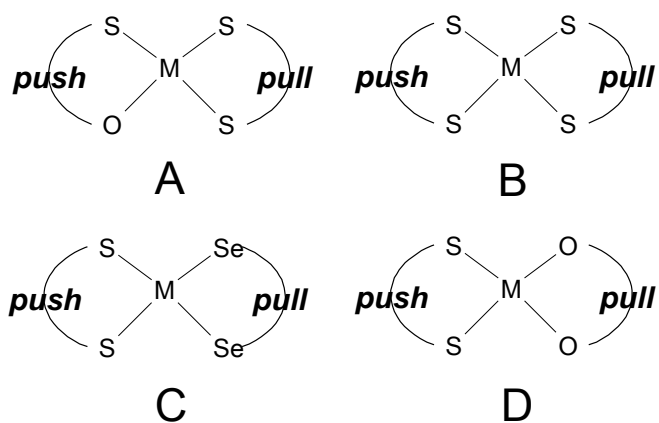
# Chapter 5

*Perspectives*



## 5.1 Introduction

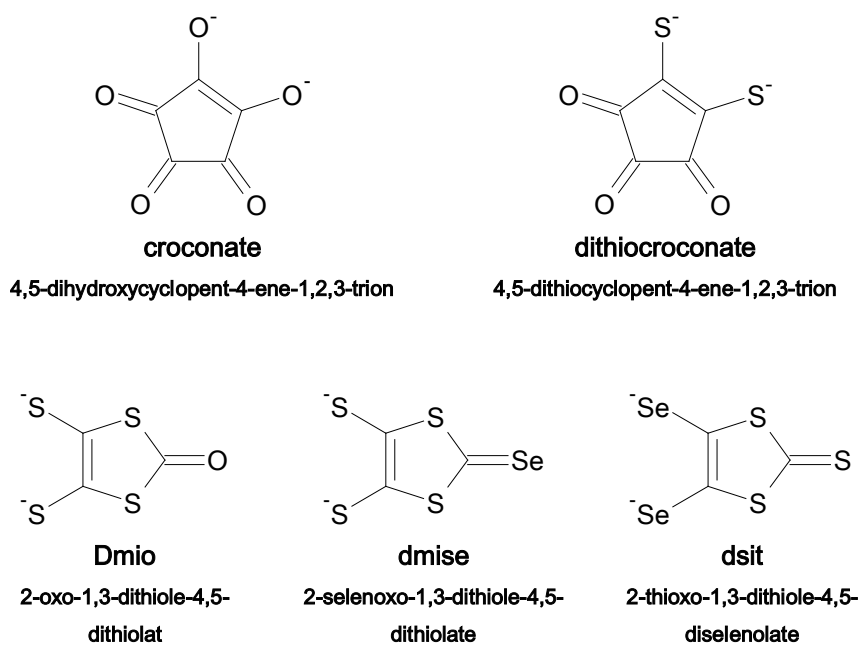
As a progress of these studies we intend to investigate the influence of the variation of the chalcogen atom (S vs Se or O) at the dithiolene core.



**Scheme 5.1:** Schematic drawing of the relative core of oxothione-dithiolato (**A**), dithione-dithiolato (**B**), dithione-diselenolato (**C**), dithione-dioxolato (**D**).

Therefore the progress of this work, is addressed to synthesize new complexes to investigate the influence of the variation of the donor atom at the dithiolene core on the nonlinear optical properties of  $d^8$  metal mixed-ligand.

In Scheme 5.2 some examples for the pull potential candidates are shown.



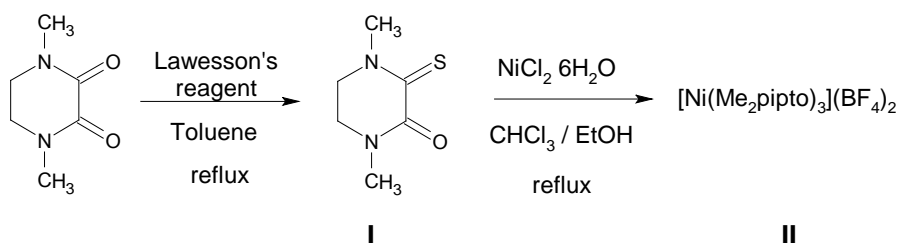
**Scheme 5.2:** Selected examples of pull ligands

Here we report the results obtained so far, and in particular:

1. Compounds where one of the sulfur donor atoms of the push ligand is replaced by an oxygen one; (see Scheme 5.1 **A**)
2. Compounds where the pull ligand have two selenium donor atoms (dsit) instead of the sulphur ones. (see Scheme 5.1 **C**)

## 5.2 Synthesis

The new ligand *N,N'*-dimethyl-piperazine-3-oxo-2-thione (Me<sub>2</sub>pipto) where one oxygen atom substitutes one sulphur in Me<sub>2</sub>pipdt have been synthesized as reported in Scheme 5.3.



**Scheme 5.3:** Reaction pathways for Me<sub>2</sub>pipto and [Ni(Me<sub>2</sub>pipto)](BF<sub>4</sub>)<sub>2</sub>

As shown in the scheme 5.3:

- I. *N,N'*-methyl-piperazine-2-,3-dione and Lawesson's reagent (molar ratio 1:0.6) were placed at reflux in toluene until the solution turned from pale yellow to light brown. The solvent was evaporated and the crude product washed several times with benzene 40/60 and dissolved with hot ethanol. A crystalline yellow precipitate appeared. The precipitation was completed by addition of diethyl ether and cooling (-18 °C for three hours). The product was collected by filtration and washed with cold EtOH and diethyl ether.

II. Me<sub>2</sub>pipto in 25 ml of CH<sub>2</sub>Cl<sub>2</sub> was added drop-wise to a solution of NiCl<sub>2</sub>·6H<sub>2</sub>O in 50 ml EtOH. After 1 hour of warming (60°C) and stirring, the solvent was evaporated and the crude product dissolved with ethanol (30 ml), then filtered. NaBF<sub>4</sub> in 50 ml of EtOH were added to the solution (molar ratio 1:2), after 1 hour under stirring 80 ml of diethyl ether were added. After 14 hours a crystalline green-yellow solid was obtained. The precipitate was collected by filtration and washed with a cold H<sub>2</sub>O/EtOH (1:1 v/v) mixture, acetone/diethyl ether (1:1 v/v) and diethyl ether.

### 5.2.1 Structural characterisation of Me<sub>2</sub>pipto

The X-ray structure of the Me<sub>2</sub>pipto is reported in Fig. 5.1

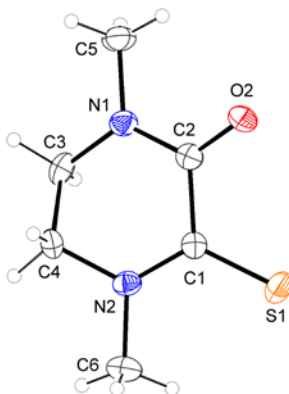


**Figure 5.1:** Ortep drawing of Me<sub>2</sub>pipto with thermal ellipsoids at the 30% probability level.

The short C-S (1.642(4) Å) and C-O (1.218(5) Å) bond distances are consistent with a double bond character. On the other hand, the trigonal planar geometry of the nitrogen atoms, the C(1)-C(2) long distance (1.538(6)), and the relatively short C-N distances (1.348(5) and 1.361(5) Å for C(1)-N(2) and C(2)-N(1), respectively) suggest a certain degree of delocalisation of the double bonds over the nitrogen atoms.

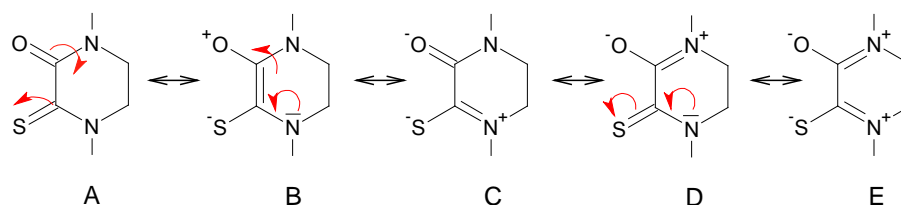
<b>Me<sub>2</sub>pipto</b>	
Empirical formula	C <sub>6</sub> H <sub>10</sub> N <sub>2</sub> OS
Formula weight	158.22
Crystal size, mm	0.43x0.40x0.30
Crystal system	Orthorhombic
Space group	<i>F</i> ha2 <sub>1</sub>
<i>a</i> , <i>b</i> , <i>c</i> , Å	9.758(4), 6.731(3), 11.686(6)
$\alpha$ , $\beta$ , $\gamma$ , deg.	90, 90, 90
<i>V</i> , Å <sup>3</sup>	767.5(6)
<i>Z</i>	4
<i>T</i> , K	293(2)
$\rho$ (calc), Mg/m <sup>3</sup>	1.369
$\mu$ , mm <sup>-1</sup>	0.354
$\theta$ range, deg.	3.49 to 26.99
No. of rflcn/obsv	962 / 565
Abs. struct. Param.	-0.09(15)
GooF	1.005
<i>R</i> 1	0.0431
<i>wR</i> 2	0.0738

**Table 5.1:** Summary of X-ray crystallographic data for Me<sub>2</sub>pipto

Selected bond lengths (Å) and angles for Me <sub>2</sub> pipto			
C(1)-S(1)	1.642(4)		
C(2)-O(2)	1.218(5)	S(1)-C(1)-C(2)	118.7(3)
C(1)-N(2)	1.348(5)	O(2)-C(2)-C(1)	121.3(4)
C(2)-N(1)	1.361(5)	S(1)-C(1)-N(2)	124.4(4)
C(1)-C(2)	1.538(6)	O(2)-C(2)-N(1)	122.3(4)
C(1)-S(1)	1.642(4)		

**Table 5.2:** Selected bond and angle for Me<sub>2</sub>pipto.

Resonance structures of R<sub>2</sub>pipto ligand show in Scheme 5.4.



**Scheme 5.4** Resonance structures of R<sub>2</sub>pipto

Electronic structure DFT-calculations on Me<sub>2</sub>pipto and Me<sub>2</sub>pipdt have been performed for comparison. The obtained frontier orbitals (FO), which are energetically well separated from the lower and higher lying orbitals, are reported in Fig. 5.2. As shown, the composition and energy of the FO in the two ligands are different, and related to the low contribution of the oxygen orbitals in Me<sub>2</sub>pipto. In particular, the higher  $\pi$ -delocalization and lower energy of the LUMO in the Me<sub>2</sub>pipdt compared to the corresponding orbital in Me<sub>2</sub>pipto, are in agreement.

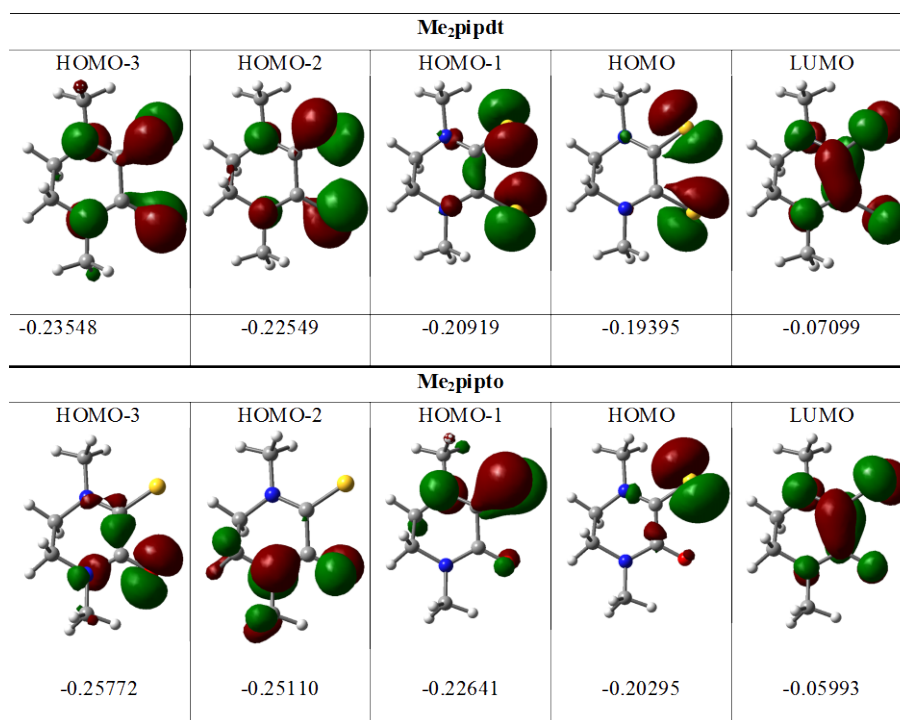


**Figure 5.2:** Molecular orbital diagrams of Me<sub>2</sub>pipto and Me<sub>2</sub>pipdt. The MO energies are reported in hartrees. The larger HOMO-LUMO gap for the Me<sub>2</sub>pipto is in agreement with the increased *hard* character of this ligand if compared to Me<sub>2</sub>pipdt<sup>[58]</sup>.

DFT calculations were carried out using the Gaussian 03 program suite<sup>[59]</sup>. Geometry optimisation were performed for the Me<sub>2</sub>pipto and Me<sub>2</sub>pipdt ligands starting from X-ray geometries. The calculation were performed with



the gradient-corrected hybrid density functional B3LYP<sup>[60,61]</sup> and with the 6-31G(d) basis set<sup>[62,63]</sup>. Molecular orbital diagrams were generated with the GaussView program<sup>[64]</sup>.

### 5.2.2 Coordination ability of Me<sub>2</sub>pipto

A preliminary study on the reactivity of the Me<sub>2</sub>pipdt toward transition metal ions, has been carried out. By reacting Me<sub>2</sub>pipto with a nickel salt, the pseudo-octahedral complex [Ni(Me<sub>2</sub>pipto)<sub>3</sub>](BF<sub>4</sub>)<sub>2</sub> (**8b**) has been obtained in spite of the square-planar complex [Ni(Me<sub>2</sub>pipdt)<sub>2</sub>](BF<sub>4</sub>)<sub>2</sub>, which was obtained working in the same experimental conditions with Me<sub>2</sub>pipdt.

The synthesis of [Ni(Me<sub>2</sub>pipto)<sub>3</sub>](BF<sub>4</sub>)<sub>2</sub> are reported in Scheme 5.3, and the molecular structure of the cation in **8b** is shown in Fig. 5.3.

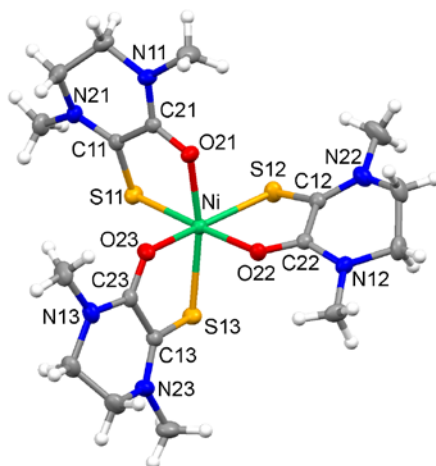


**Figure 5.3.:** Molecular drawing of  $[\text{Ni}(\text{Me}_2\text{pipto})_3]^{2+}$  with thermal ellipsoids at the 30% probability level; the  $\text{BF}_4^-$  anions have been removed for clarity.

The metal exhibits an octahedral geometry achieved by three bidentate SO donor ligands. The disposition of the sulphur and oxygen atoms is such that the complex is in the *fac* configuration. The C-S and C-O bond distances are in the range 1.669(2)-1.676(2) Å and 1.241(2)-1.246(2) Å, respectively, suggesting a double bond character for these moieties. Nevertheless, the planar nature of the thioamide-like or amide-like functions within each ligand and the short C-N bonds of these groups (range 1.308(2)-1.321(2) Å) point to a certain electron delocalization over the NCS or NCO atoms. As a consequence of the coordination, a decrease (increase) of CO and CS (CN) double bond character is observed with respect to the free ligand (see Scheme 5.4). This is reflected by the shift of the  $\nu(\text{CO})$  and  $\nu(\text{CN})$  stretching

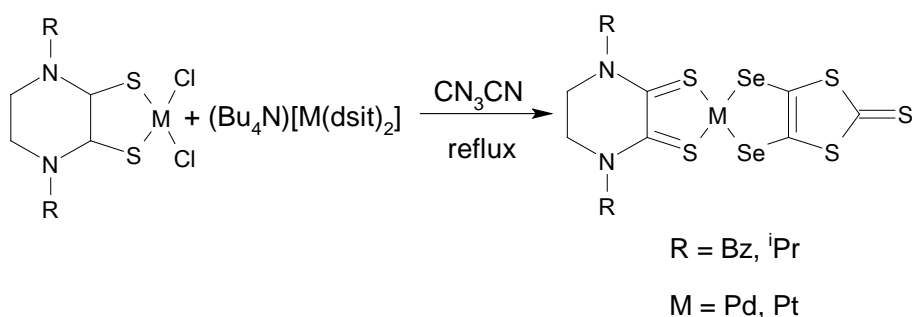
vibrations to lower (1642  $\text{cm}^{-1}$ ) and higher (1559  $\text{cm}^{-1}$ ) frequencies respectively with respect to the free ligand (1669 and 1527  $\text{cm}^{-1}$ ). The smaller stabilization's energy of the SO ligand compared to the dithione one, due to the reduced  $\pi$ -acceptor capability of the former, explains the different stoichiometry between the Ni complexes. In particular, in these cases, the  $\pi$ -back-donation from the  $d$ -metal orbitals to the empty sulphur's  $d$ -orbitals seems to play a crucial role. This is in agreement with the *fac* configuration of the complex, in fact, each sulphur is located in *trans*-position to an oxygen atom which can't compete for the metal's electrons.

Summary of X-ray crystallographic data for  $[\text{Ni}(\text{Me}_2\text{pipto})_3](\text{BF}_4)_2$  are reported in Appendix.

Currently experiments on the preparation of mixed-ligand complexes as potential nonlinear optic chromophores are carried out.

### 5.3 Synthesis of $[M(R_2\text{pipdt})(\text{dsit})]$ ( $M=\text{Pd}, \text{Pt}$ ; $R= \text{Bz}, \text{iPr}$ )

In Scheme 5.5 a summary of the synthetic procedures used to obtain mixed ligand dithiolene complexes is reported.



**Scheme 5.5:** Reaction pathways for  $[M(R_2\text{pipdt})(\text{dsit})]$

As shown in the Scheme 5.4 the mixed ligand metal dithiolene complexes  $[M(R_2\text{pipdt})(\text{dsit})]$  ( $M = \text{Pd}, \text{Pt}$ ), are obtained by mixing  $[M(\text{Bz}_2\text{pipdt})\text{Cl}_2]$  with  $(\text{Bu}_4\text{N})_2[M(\text{dsit})_2]$ . This reaction involves the facile displacement of two chloride ions by the chelating dsit dianion.

#### 5.3.1 Structural characterization of $[\text{Pt}(\text{Bz}_2\text{pipdt})(\text{dsit})]$

Crystals of  $[\text{Pt}(\text{Bz}_2\text{pipdt})(\text{dsit})]$  and  $[\text{Pd}(\text{iPr}_2\text{pipdt})(\text{dsit})]$  were grown by slow diffusion of diethyl ether into a concentrated solution of complexes in DMF. In both case the central atom is coordinated in an square planar environment by two S atoms for the *push* ligand ( $R_2\text{pipdt}$ ) and two Se atoms

for the *pull* ligand (dsit). M-S and M-Se coordination bonds broadly similar on both sides of the complex.

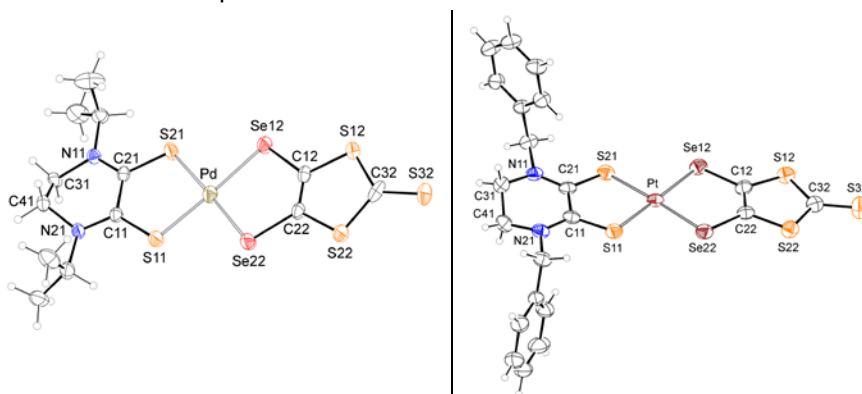


Figure 5.4: ORTEP drawing of **7a** with thermal ellipsoids drawn at the 30% probability level.

Figure 5.5 shows that, in the crystal lattice for **7a** complex, the complex units are almost parallel and head-to-tail with respect to each other.

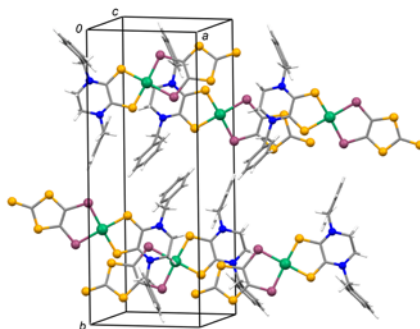


Figure 5.5: Single crystal X-ray data showing crystal packing of **7a** projected along the *c* axis.

Selected bond of dithiolene core lengths are reported in Table 5.3.

Bond lengths (Å) of [Pd( <i>Pr</i> <sub>2</sub> pipdt)(dsit)]		Bond lengths (Å) of [Pt( <i>Bz</i> <sub>2</sub> pipdt)(dsit)]	
Pt-S(11)	2.2401(18)	Pt-S(11)	2.2642(19)
Pt-S(21)	2.2407(18)	Pt-S(21)	2.276(2)
Pt-Se(12)	2.3578(9)	Pt-Se(12)	2.4034(9)
Pt-Se(22)	2.3504(9)	Pt-Se(22)	2.3939(9)

**Table 5.3:** Selected bond of the core for [M(*R*<sub>2</sub>pipdt)(dsit)]

A summary of X-ray crystallographic parameters are reported in Table 5.4.

	[Pd( <i>Pr</i> <sub>2</sub> pipdt)(dsit)]	[Pt( <i>Bz</i> <sub>2</sub> pipdt)(dsit)]
Empirical formula	C <sub>13</sub> H <sub>18</sub> N <sub>2</sub> PdS <sub>5</sub> Se <sub>2</sub>	C <sub>21</sub> H <sub>18</sub> N <sub>2</sub> PtS <sub>5</sub> Se <sub>2</sub>
Formula weight	626.91	811.68
Crystal size (mm)	0.41 x 0.08 x 0.04	0.18 x 0.17 x 0.11
Crystal system	Monoclinic	Monoclinic
Space group	P2 <sub>1</sub> /n	P2 <sub>1</sub> /n
a, b, c (Å)	6.341(1), 19.568(2), 16.480(2)	9.267(2), 23.189(5), 11.555(3)
α, β, γ (deg.)	90, 94.884(2), 90	90, 98.069(4), 90
V (Å <sup>3</sup> )	2037.4(5)	2458.5(10)
Z	4	4
T (K)	293(2)	293(2)
ρ(calc) (Mg/m <sup>3</sup> )	2.044	2.193
μ (mm <sup>-1</sup> )	4.995	9.107
θ range (deg.)	1.62 to 27.03	1.76 to 27.66
No. of rflcn/obsv >4σ(F)	23329 / 4429	32475 / 5703
GooF	1.015	1.017
R1 [a]	0.0751	0.0691
wR2 [b]	0.1415	0.1004

**Table 5.4:** Summary of X-ray crystallographic data for 7a and 7b. [a] R1 =  $\sum ||F_o| - |F_c|| / \sum |F_o|$ ; [b] wR2 =  $[\sum [w(F_o^2 - F_c^2)^2] / \sum [w(F_o^2)^2]]^{1/2}$ , w =  $1 / [\sigma^2(F_o^2) + (aP)^2 + bP]$ , where P =  $[\max(F_o^2, 0) + 2F_c^2] / 3$

## *Chapter 5*

---

In Appendix, additional selected bond distances and angles are given.  
Second-order NLO activity for these complexes will be performed by  
M. Pizzotti group at University of Milano.

## 5.4 Experimental Details

**Me<sub>2</sub>pipto (1d)**: 3.00 g (21.1 mmol) of *N,N'*-dialkyl-piperazine-2-,3-dione and 5.12 g (12.6 mmol) of Lawesson's reagent (molar ratio 1:0.6) were placed at reflux in 300 ml of toluene until the color of the solution turned from pale yellow to light brown. The solvent was evaporated and the crude product washed several times with benzene 40/60 and dissolved with hot ethanol. A crystalline yellow precipitate appeared the precipitation was completed by addition of diethyl ether and cooling (-18 °C for three hours). The product was collected by filtration and washed with cold EtOH (three times) and with diethyl ether (three times) (yield 1.98 g, 12.5 mmol; 59.3%). Analytical results are in accordance with the formula Me<sub>2</sub>pipto. *Elemental Analysis*: calculated for C<sub>6</sub>H<sub>10</sub>N<sub>2</sub>OS (158.22): C 45.55, H 6.37, N 17.71, S 20.27; found: C 45.32, H 6.77, N 17.73, S 20.55. *UV-vis* (in CH<sub>3</sub>CN solution): λ/nm (ε/mol·cm<sup>-1</sup>·dm<sup>-3</sup>) 310 (7.35·10<sup>3</sup>); 265 (4.65·10<sup>3</sup>). *FT-IR* (KBr): ν<sub>max</sub>/cm<sup>-1</sup> 2970(w); 2954(w); 2920(mw); 2878(w); 2859(w); 1669(vs); 1527(vs); 1487(s); 1453(s); 1453(s); 1429(ms); 1395(s); 1348(vs); 1260(s); 1199(s); 1151(m); 1046(mw); 1019(w); 955(s); 894(ms); 837(w); 762(s); 687(ms); 582(ms); 549(mw); 494(m); 420(ms).

**[Ni(Me<sub>2</sub>pipto)<sub>3</sub>](BF<sub>4</sub>)<sub>2</sub> (8b)**: 80.0 mg (0.51 mmol) of **1** in 25 ml of CH<sub>2</sub>Cl<sub>2</sub>, yellow solution, was added drop-wise to a solution of NiCl<sub>2</sub>·6H<sub>2</sub>O (58.3 mg, 0.25 mmol) in EtOH (50 ml). After 1 hour of warming (60°C) and stirring, the solvent was evaporated and the crude product dissolved with ethanol (30 ml)



and filtered, than 55,0 mg of NaBF<sub>4</sub> in 50 ml of EtOH were added to the solution, after 1 hour under stirring, 80 ml of diethyl ether were added. A crystalline green-yellow solid appeared 14 hours after, the precipitate was collected by filtration and washed with a cold H<sub>2</sub>O/EtOH (1:1) mixture (once), acetone/diethyl ether (1:1, two times) and diethyl ether (three times) (yield 34.2 mg, 4.8×10<sup>-2</sup> mmol; 38.7%). Analytical results are in accordance with the formula [Ni(Me<sub>2</sub>pipto)<sub>3</sub>](BF<sub>4</sub>)<sub>2</sub>. *Elemental Analysis*: calculated for C<sub>18</sub>H<sub>30</sub>N<sub>6</sub>O<sub>3</sub>S<sub>3</sub>NiB<sub>2</sub>F<sub>8</sub> (706.95): C 30.58, H 4.28, N 11.89, S 13.60; found: C 30.21, H 4.38, N 11.43, S 13.34. *UV-vis* (in CH<sub>3</sub>CN solution): λ/nm (ε/mol·cm<sup>-1</sup>·dm<sup>-3</sup>) 370 (sh); 310 (2.10·10<sup>4</sup>); 275 (1.90·10<sup>4</sup>). *FT-IR* (KBr): ν<sub>max</sub>/cm<sup>-1</sup> 2978(w); 2925(w); 1642(vs); 1559(vs); 1494(ms); 1443(mw); 1408(ms); 1368(s); 1263(ms); 1209(ms); 1159(ms); 1106(s); 1028(s); 963(m); 898(m); 830(w); 754(m); 696(m); 583(m); 562(m); 533(m); 521(m); 494(m); 448(m).

**Pt(Bz<sub>2</sub>pipdt)(dsit)] (7a)**: (Bu<sub>4</sub>N)<sub>2</sub>[Pt(dsit)<sub>2</sub>] (98,80 mg) in 25cm<sup>3</sup> of CH<sub>3</sub>CN (green solution) was added drop-wise to a dark red suspension of [Pt(<sup>i</sup>Pr<sub>2</sub>pipdt)](Cl)<sub>2</sub> (51,48 mg) in 25cm<sup>3</sup> CH<sub>3</sub>CN, under stirring and reflux. After one day a dark green solid was formed (67,50 mg ; yield: 96%). This solid was filtered, washed with diethyl ether and then dried. Well formed crystals suitable for X-ray crystallography have been obtained through re-crystallization from DMF/Et<sub>2</sub>O. **CHNS**: Found (Calcd for C<sub>21</sub>H<sub>18</sub>N<sub>2</sub>PdS<sub>7</sub>) C% 30,78 (31.07), H% 2,04 (2.24), N% 3,14 (3.45), S% 21,56 (19.75).

**Pd(*Pr*<sub>2</sub>pipdt)(*dsit*) (7b)**. (Bu<sub>4</sub>N)<sub>2</sub>[Pd(*dsit*)<sub>2</sub>] (50 mg) in 25cm<sup>3</sup> of CH<sub>3</sub>CN (green solution) was added drop-wise to a dark red suspension of [Pt(*Pr*<sub>2</sub>pipdt)](Cl)<sub>2</sub> (27 mg) in 25cm<sup>3</sup> CH<sub>3</sub>CN, under stirring and reflux. After one day a dark green solid was formed (28 mg ; yield: 85%). This solid was filtered, washed with diethyl ether and then dried. Well formed crystals suitable for X-ray crystallography have been obtained through re-crystallization from DMF/ Et<sub>2</sub>O.

---

*Conclusions*



## 6.1 Conclusion

New mixed-ligand dithiolene complexes have been prepared and fully characterized.

A convenient synthetic strategy has been successfully developed to obtain in high yields mixed-ligand complexes of the  $d^8$  triad ( $Ni^{II}$ ,  $Pd^{II}$  and  $Pt^{II}$ ). This has allowed for the first time to perform a study on the second order NLO properties on the whole  $d^8$  group metal complexes.

This achievement is relevant since mixed ligand complexes of palladium and platinum complexes are rare and the availability of the whole  $d^8$  metal complexes has allowed to investigate in particular the metal dependence of the observed properties which are here summarized.

The complexes are characterized by the following features:

1. show a peak in the visible-NIR spectral region of medium to low molar absorption coefficients with negative solvatochromism;
2. show high negative values of the molecular first hyperpolarizability, determined from electric-field-induced second harmonic generation experiments;
3. are redox active showing two quasi-reversible reduction processes, and an irreversible anodic oxidation;

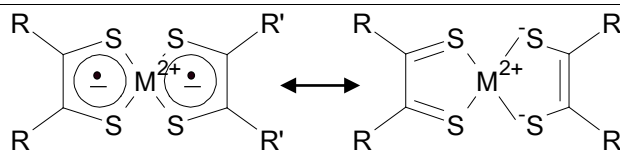
4. show reversible bleaching of the solvatochromic peak for mono- reduction;
5. show bond distances at the C<sub>2</sub>S<sub>2</sub>MS<sub>2</sub>C<sub>2</sub> core with longer C-C and shorter C-S bond distances of the dithione ligand when compared to dithiolate. This structural data are in accordance with the presence in the mixed-ligand complexes of two different unsaturated chelating ligands, one more easily reduced (acceptor, dithione), the other more easily oxidized (donor, dithiolate);

The availability of well characterized complexes on metal and ligand variations is providing an improved understanding of structure/properties relationship with the view to optimize the optical properties by suitable ligand and metal design.

Accordingly, the proper selection of the push/pull ligands and the metal will produce complexes describable as prevailing:  $\pi$ -delocalized systems or  $\pi$ -localized systems. In addition to structural data, spectroscopic and electrochemical features reflect the delocalized/localized  $\pi$  electron distribution, and suitable markers such as  $\lambda_{\max}$ ,  $\epsilon$ ;  $\nu(\text{C}=\text{C})$ ; reduction

potentials work well to distinguish the limiting forms and to predict the optical properties.

In following table, the different features of  $d^8$  metal mixed-ligand dithiolene complexes depending on the  $\pi$ -delocalization inside dithiolene core are reported.



	$\pi$ delocalized	$\pi$ Localized
<b>Prevailing resonance form in the ground state</b>	Similar push/pull character of ligands	Different <i>push</i> (R)/ <i>pull</i> (R') character of the ligands
<b>Predictable optical properties</b>	Electrochromic NIR dyes	Second Order NLO chromophores
<b>Suitable markers</b>		
$\lambda_{\max}$	Vis-NIR	Vis-NIR
$\epsilon$	High	Medium to low
<b>(C=C) distance</b>	Similar in the two ligands	Longer (R, push ligand) Shorter (R', pull ligand)
<b>N (C=C) typical of reduction potentials dependent on</b>	Dithiolenes Both ligands	Dithiolate Push ligand

**Table 6.1:** Summary of structure/properties relationship in square-planar  $d^8$  metal mixed-ligand dithiolene complexes.

Among the  $d^8$  metal complexes, platinum derivatives seem most promising as second-order NLO chromophores and among the complexes so far investigated the highest  $\mu\beta$  value has been achieved for [Pt(Bz<sub>2</sub>pipdt)(dmit)]. Moreover, the comparison of the observed properties with those of  $\pi$ -localized  $d^8$  metal diimine-dithiolato complexes so far reported in the literature allows to point out that mixed-ligand dithiolene complexes:

- 1) Show higher values of negative molecular quadratic optical nonlinearities
- 2) Show reversible reduction waves at less negative potential.
- 3) Do not exhibit photoluminescence as reported in Appendix A9.

A new ligand (Me<sub>2</sub>pipto), where one of the sulphur donor atoms of the push ligand is replaced by an oxygen one, has synthesized and characterised. The comparison with Me<sub>2</sub>pipdt ligand has allowed to point out that the composition and energy of the frontier orbitals in the two ligands are different, and relatable to the low contribution of the oxygen to the Frontier Orbitals.

The introduction of the selenium atom in the dithiolene core is expected also have an effect in the electronic distribution due to the increased size of orbital.

Further, experiments are in course to functionalize the periphery of the ligands to promote:

- A) the formation of non-centrosymmetric crystals. This is important both with the view to obtain crystals which a non-centrosymmetric space group which is crucial in order to maintain second order NLO activity in the bulk.
- B)  $\pi$ -stacking which can affect the electroconductive properties of the complexes;
- C) theoretical studies to achieve deep understanding of the factors which affect the structure/property relationship;
- D) the processing of materials for their possible use in optical devices. In particular the variation of groups at the periphery of the ligands is expected to improve solubility to introduce functional groups to favour the processing of the products in form of thin films, or sol gel glasses, or also anchored to TiO<sub>2</sub> surfaces

As most promising results for further work it can be cited the redox switching of the solvatochromic peak.

Indeed the methods for modulating molecular NLO responses are currently attracting great interest, and relevant results based mostly on ruthenium complexes have appeared only recently in the literature.



*Conclusions*

---

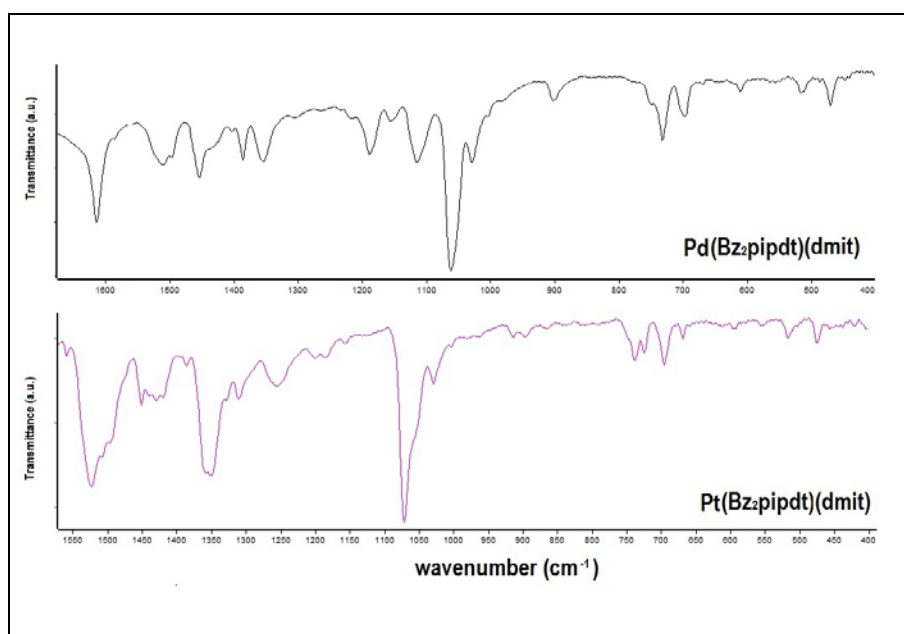
---

*Appendices*

An L-shaped bracket consisting of a vertical line on the left and a horizontal line on the bottom, both starting from the same point on the left and extending to the right.

## A.1 Vibrational spectra of $M(\text{Bz}_2\text{pipdt})(\text{dmit})$

The FT-IR spectra of the complexes  $[M(\text{R}_2\text{pipdt})(\text{dmit})]$  are shown in Figures A.1, where the spectra of compound **2b** and **2c** are reported for comparison. FT-IR spectra on KBr pellets were collected with a Bruker Equinox 55 spectrophotometer.



Figures A.1: FT-IR spectra of **2b** and **2c**

A.2 Crystallographic data for [Pt(Bz<sub>2</sub>pipdt)(dcbdt)]

Selected bond and angle of [Pt(Bz<sub>2</sub>pipdt)(dcbdt)] are reported in Table A.1.

Bond lengths (Å) and Angle (deg.) of [M(Bz <sub>2</sub> pipdt)(dmit)]			
S(2)-C(10)	1.751(4)	S(2)-Pt-S(2)'	89.88(5)
S(1)- C(1)	1.688(4)	S(2)-Pt-S(1)'	177.25(4)
C(10)- C(10)'	1.390(7)	S(2)'-Pt-S(1)'	90.99(4)
C(10)- C(11)	1.392(5)	S(2)-Pt-S(1)	90.99(4)
C(4)- C(9)	1.371(6)	S(2)'-Pt-S(1)	177.25(4)
C(4)- C(5)	1.386(7)	S(1)'-Pt-S(1)	88.27(5)
C(4)- C(3)	1.515(6)	C(10)-S(2)-Pt	103.73(13)
C(1)- N(1)	1.323(4)	C(1)-S(1)-Pt	105.76(14)
C(1)- C(1)'	1.484(8)	C(10)'-C(10)-C(11)	119.7(2)
C(12)- C(11)	1.380(6)	C(10)'-C(10)-S(2)	121.33(12)
C(12)- C(12)'	1.411(9)	C(11)-C(10)-S(2)	118.9(3)
C(13)- C(12)	1.443(6)	C(9)-C(4)-C(5)	119.1(5)
N(1)- C(2)	1.467(5)	C(9)-C(4)-C(3)	120.8(4)
N(1)- C(3)	1.470(5)	C(5)-C(4)-C(3)	120.0(4)
C(2)- C(2)'	1.424(9)	N(1)-C(1)-C(1)'	119.6(2)
C(13)- N(2)	1.125(6)	N(1)-C(1)-S(1)	120.6(3)
C(5)- C(6)	1.395(8)	C(1)'-C(1)-S(1)	119.87(14)
C(6)- C(7)	1.366(9)	C(11)-C(12)-C(12)'	119.5(3)
C(9)- C(8)	1.366(7)	C(11)-C(12)-C(13)	120.4(4)

**Table A.1:** Bond lengths [Å] and angles [deg] for [(Pt(Bz<sub>2</sub>pipdt))(dcbdt)]; Symmetry transformations used to generate equivalent atoms: 1' -x+1,y,-z+1/2

### A.3 Crystallographic data and experimental details for $[\text{Pt}(\text{Et}_2\text{dazdt})_2][\text{Pt}(\text{mnt})_2]$

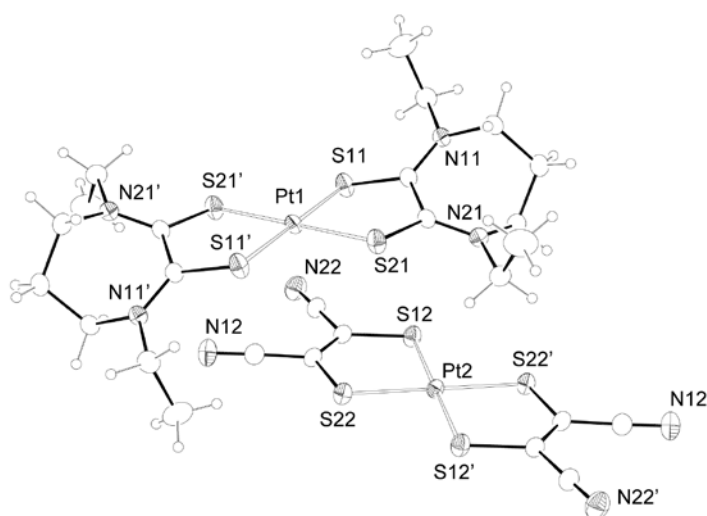


**Figure A.2:** Ortep drawing of  $[\text{Pt}(\text{Et}_2\text{dazdt})_2][\text{Pt}(\text{mnt})_2]$  with thermal ellipsoids drawn at the 30% probability level.

The anionic and cationic complexes form an irregular stack that lies in the  $bc$  crystallographic plane. This is generated through interactions between the metal centers and the ligand framework of adjacent molecules. The distance between the Pt atoms of the  $[\text{Pt}(\text{mnt})_2]^{2-}$  anion and the nitrogen atoms of the

cation complex is of 3.84Å, whereas the distance between the Pt atoms of [Pt(Et<sub>2</sub>dazdt)<sub>2</sub>]<sup>2+</sup> and the carbon atom of the anionic complex is of 3.56 Å.

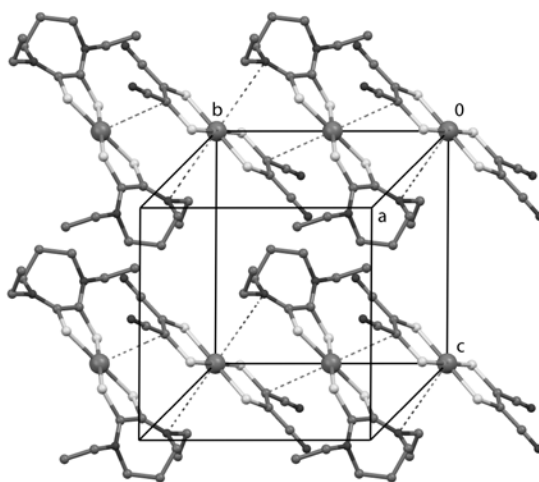


**Figure A.3:** Crystal packing of [Pt(Epta-Et)<sub>2</sub>][Pt(mnt)<sub>2</sub>]. Packing range  $a = 0-0.5$ ,  $b = 0-1.5$ ,  $c = 0-1$ . Hydrogen atoms were omitted for clarity.

### A.4 Schematic diagram of the setup for an EFISH experiment.

The schematic diagram of the setup for an EFISH experiment are reported below in Figure A4.

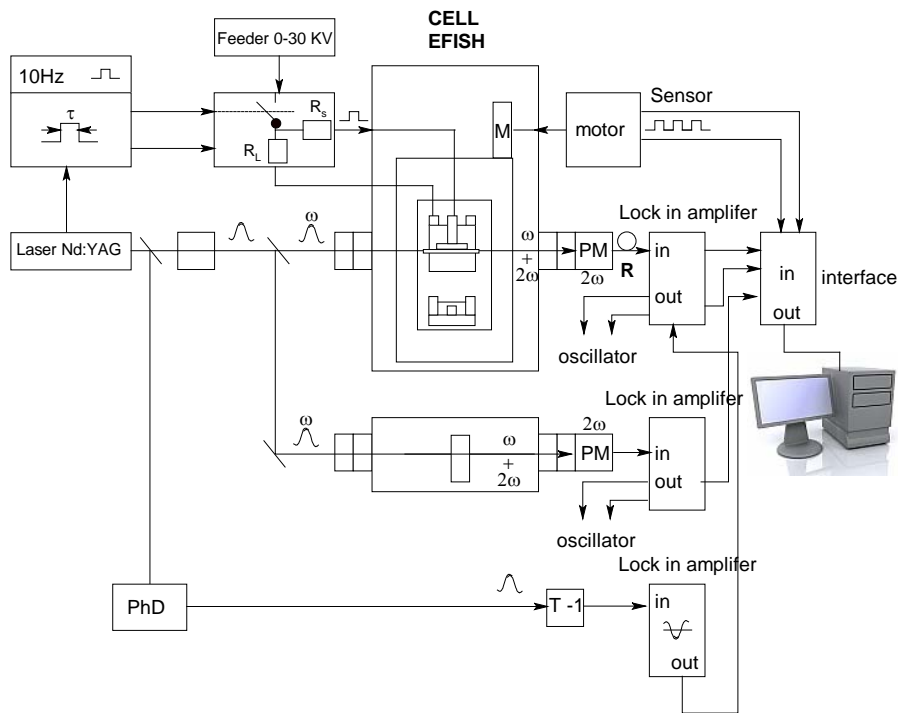
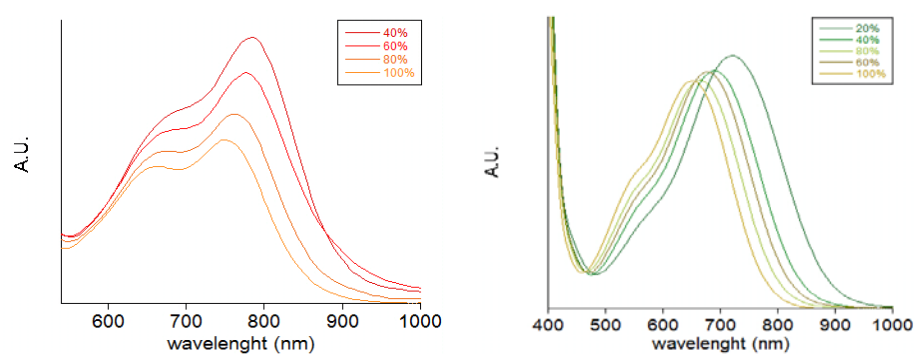
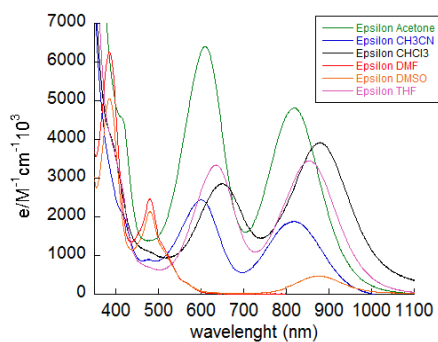


**Figure A4:** Schematic diagram of the setup for an Electric field induced second harmonic generation (EFISH) experiment.

## A.5 Solvatochromic studies

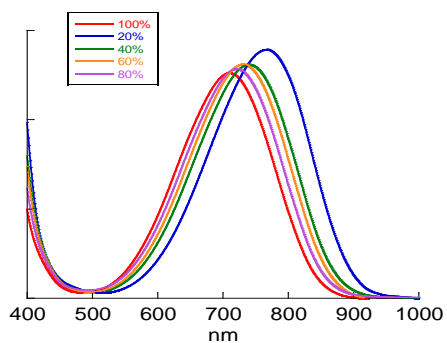


**Figures A.5:** solvatochromic studies of **4a** and **4b**, showing negative solvatochromism for the NIR absorption in DMF/CS<sub>2</sub> mixtures ranging from DMF 100% to 20%.



**Figures A.6:** solvatochromic studies of **5a**, showing negative solvatochromism for the NIR absorption in DMF/CS<sub>2</sub> mixtures ranging from DMF 100% to 20%.





**Figures A.7** solvatochromic studies of **6**, showing negative solvatochromism for the NIR absorption in DMF/CS<sub>2</sub> mixtures ranging from DMF 100% to 20%.

## A.6 DFT calculation for [M(Bz<sub>2</sub>pipdt)(mnt)] (M = Ni, Pd, Pt)

The calculated structures of **3a**, **3b** and **3c** are depicted in Figure A1 while the structural parameters obtained from the optimization procedures for all compounds under study are collected in Table A.2.

S.P.	Ni(Bz <sub>2</sub> pipdt)(mnt)		Pd(Bz <sub>2</sub> pipdt)(mnt)		Pt(Bz <sub>2</sub> pipdt)(mnt)	
	Exp.	Calc.	Exp.	Calc.	Exp.	Calc.
<i>Bonds</i>						
M-S (mnt)	2.134(2)	2.175	2.2748(7)	2.294	2.2689(9)	2.293
M-S (Bz <sub>2</sub> pipdt)	2.156(2)	2.204	2.2893(7)	2.329	2.2780(9)	2.314
S-C (mnt)	1.716(7)	1.743	1.734(3)	1.748	1.735(3)	1.746
S-C (Bz <sub>2</sub> pipdt)	1.690(6)	1.703	1.688(3)	1.699	1.691(3)	1.704
C-C (mnt)	1.392(6)	1.375	1.354(4)	1.373	1.343(6)	1.375
C-C (Bz <sub>2</sub> pipdt)	1.489(6)	1.473	1.499(3)	1.468	1.490(6)	1.453
C-N (Bz <sub>2</sub> pipdt)	1.316(7)	1.355	1.317(4)	1.360	<i>Na</i>	1.365
<i>Angles</i>						
S-M-S (mnt)	92.98(6)	92.4	90.35(2)	89.3	90.32(5)	89.2
S-M-S (Bz <sub>2</sub> pipdt)	91.37(6)	90.3	88.61(2)	86.9	88.19(5)	86.77
M-S-C (mnt)	103.7(2)	103.3	102.2(2)	103.4	<i>Na</i>	103.5
M-S-C (Bz <sub>2</sub> pipdt)	106.1(2)	105.8	105.3(1)	105.8	<i>Na</i>	106.17
S-C-C (mnt)	119.8(4)	120.4	122.7(2)	122.0	<i>Na</i>	121.91
S-C-C (Bz <sub>2</sub> pipdt)	118.2(4)	118.9	120.0(2)	120.6	<i>Na</i>	120.38

**Table A.2:** Main structural parameters for complexes **3a**, **3b** and **3c**.

The data provided in Table A3, we conclude that the general electronic properties of **3a**, **3b** and **3c**, regarding the nature of the MMLL' charge transfer should not differ significantly from those expected.

	MO	E <sub>ov</sub>	Bz <sub>2</sub> pipdt	M	mnt	MO	E <sub>ov</sub>	Bz <sub>2</sub> pipdt	M	Mnt
Ni	Unoccupied					Occupied				
	66b	-1.39	99.7	0.5	-0.2	<b>63b</b>	<b>-5.54</b>	<b>20.0</b>	<b>10.0</b>	<b>70.0</b>
	69°	-1.52	91.9	0.5	7.6	67°	-6.66	7.9	34.2	57.9
	68°	-1.66	8.9	2.1	89.0	66°	-7.05	9.9	75.8	14.3
	65b	-2.51	23.0	44.2	32.7	62b	-7.25	28.3	48.3	23.4
	<b>64b</b>	<b>-3.96</b>	<b>79.7</b>	<b>4.8</b>	<b>15.6</b>	65°	-7.27	66.0	9.2	24.8
						61b	-7.43	36.6	11.6	51.8
Pd	<i>Unoccupied</i>					<i>Occupied</i>				
	70°	-1.24	103.3	-4.9	1.6	<b>63b</b>	<b>-5.48</b>	<b>19.3</b>	<b>8.2</b>	<b>72.5</b>
	69°	-1.39	101.6	-1.8	0.2	67°	-6.64	10.7	26.2	63.1
	68°	-1.59	0.9	1.4	97.7	66°	-7.14	3.1	75.9	21.0
	65b	-2.48	26.7	34.4	38.9	62b	-7.35	52.0	8.4	39.6
	<b>64b</b>	<b>-3.94</b>	<b>80.4</b>	<b>4.7</b>	<b>14.8</b>	65a	-7.43	73.6	4.8	21.6
						61b	-7.44	37.8	30.9	31.3
Pt	<i>Unoccupied</i>					<i>Occupied</i>				
	70°	-1.18	100.1	-0.3	0.3	<b>63b</b>	<b>-5.56</b>	<b>26.1</b>	<b>10.4</b>	<b>63.5</b>
	69°	-1.32	95.9	4.4	-0.3	67a	-6.49	19.1	33.9	46.9
	68°	-1.69	0.2	1.5	98.3	66a	-7.26	18.4	63.6	18.0
	65b	-1.86	31.5	32.3	36.2	62b	-7.31	36.9	30.8	32.3
	<b>64b</b>	<b>-3.89</b>	<b>75.2</b>	<b>7.5</b>	<b>17.3</b>	65a	-7.46	75.7	1.7	22.5
						61b	-7.49	74.2	4.3	21.5

**Table A.3:** Contribution of different fragments to complexes valence orbitals. HOMO and LUMO orbitals are shown in bold.

In the case of compounds **3a**, **3b** and **3c**. The presence of two ligands of significantly different donor/acceptor ability leads to compounds that are best described by the donor-M<sup>II</sup>-acceptor scheme.

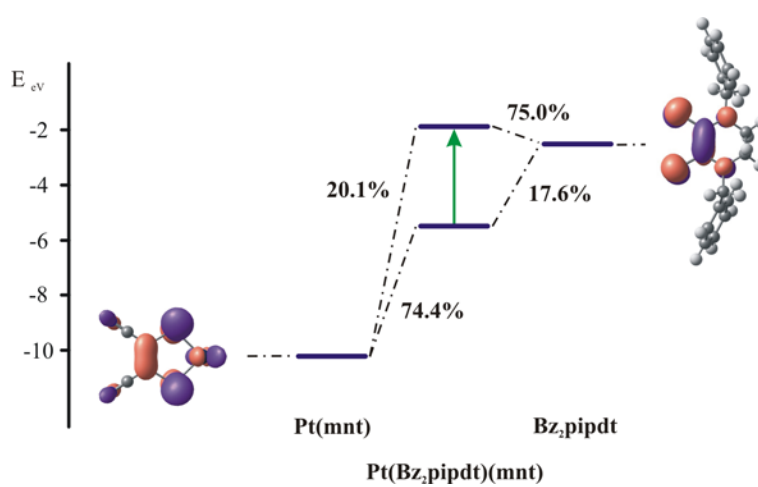


**Figure A.8:** Fragment molecular orbital analysis for **3c**.

In Table A.4, the contribution of different fragments (the two ligands and the central metal) to the complexes' frontier orbitals in the presence of a DMSO electric field is depicted.

	MO	E <sub>ov</sub>	Bz <sub>2</sub> pipdt	M	mnt	MO	E <sub>ov</sub>	Bz <sub>2</sub> pipdt	M	Mnt
Ni	<i>Unoccupied</i>					<i>Occupied</i>				
	66b	-0.81	100.1	0.2	-0.3	<b>63b</b>	<b>-5.70</b>	<b>15.0</b>	<b>19.8</b>	<b>65.2</b>
	69°	-0.97	92.5	0.5	7.0	67a	-6.43	20.8	61.5	17.7
	65b	-2.15	20.2	54.2	25.6	66a	-6.48	9.1	93.5	-2.6
	68°	-2.24	0.6	1.3	98.1	62b	-7.02	30.2	39.8	30.0
	<b>64b</b>	<b>-3.51</b>	<b>93.0</b>	<b>3.5</b>	<b>3.4</b>	65°	-7.16	83.3	1.4	15.3
Pd	<i>Unoccupied</i>					<i>Occupied</i>				
	70°	-0.68	36.8	19.1	44.1	<b>63b</b>	<b>-5.72</b>	<b>9.7</b>	<b>12.3</b>	<b>78.0</b>
	69°	-0.78	58.9	18.0	23.2	67a	-6.71	37.1	31.6	31.3
	68°	-2.20	0.1	1.3	98.6	66°	-7.01	87.4	11.4	1.2
	65b	-2.58	29.0	35.2	35.8	62b	-7.04	95.0	0.7	4.3
	<b>64b</b>	<b>-3.47</b>	<b>93.8</b>	<b>2.8</b>	<b>3.5</b>	65°	-7.15	17.5	67.6	14.9
Pt	<i>Unoccupied</i>					<i>Occupied</i>				
	70°	-0.68	27.9	26.0	46.1	<b>63b</b>	<b>-5.67</b>	<b>16.2</b>	<b>17.1</b>	<b>66.7</b>
	69°	-0.75	72.5	1.3	26.1	67°	-6.48	34.9	36.6	28.6
	65b	-1.90	29.7	33.6	36.7	66°	-7.02	96.5	2.7	0.8
	68°	-2.23	0.1	1.6	98.3	62b	-7.05	97.5	0.6	1.9
	<b>64b</b>	<b>-3.47</b>	<b>91.1</b>	<b>4.0</b>	<b>4.9</b>	65°	-7.19	53.7	37.7	8.6
					61b	-7.21	99.3	0.2	0.5	

**Table A.4:** Contribution of different fragments to complexes valence orbitals in the presence of a DMSO electric field. HOMO and LUMO orbitals are shown in bold.

### A.7.1. Absorption Spectroscopy

Selected low lying singlet and triplet excited states along with their vertical excitation energies and oscillator strengths for are displayed in Tables 3-5. In these Tables we use the following abbreviations: MMLL'CT = mixed metal-ligand to ligand charge transfer, MLCT = metal to ligand charge transfer, LMCT = ligand to metal charge transfer, LLCT = ligand to ligand charge transfer and IL = intra ligand charge transfer.

State	Composition <sup>a1</sup>	$\Delta E$ <sub>2</sub>	Exp. <sub>3</sub>	f <sub>4</sub>	Character	
b <sup>1</sup> A	HOMO → LUMO	44%	1.65	1.65	0.115 3	mnt/Ni/Bz <sub>2</sub> pipdt → Bz <sub>2</sub> pipdt (MMLL'CT)
	HOMO → LUMO+2	31%				mnt/Ni/Bz <sub>2</sub> pipdt → Ni/mnt/Bz <sub>2</sub> pipdt (LMCT)
	HOMO-3 → LUMO+2	9%				Ni/Bz <sub>2</sub> pipdt/mnt → Ni/mnt/Bz <sub>2</sub> pipdt(LMCT/ <i>deloc.</i> )
State	Composition	$\Delta E$	Exp.	F	Character	

<sup>1</sup> Compositions of electronic transitions are expressed in terms of contributing excitations between ground-state Kohn–Sham molecular orbitals. The calculation provided was done employing a 10MDF core potential for the nickel, since the latter show a slightly better behavior as compared to data extracted with 10MHF. Difference was ~ 0.1 eV.

<sup>2</sup> Transition energy from the a<sup>1</sup>A ground state in eV.

<sup>3</sup> Values for a DMF solution.

<sup>4</sup> Oscillator strength.

*Appendix*

c <sup>1</sup> A	HOMO → LUMO	39%	1.82	1.88s h	0.139 4	mnt/Ni/Bz <sub>2</sub> pipdt → Bz <sub>2</sub> pipdt (MMLL'CT)
	HOMO → LUMO+2,	36%				mnt/Ni/Bz <sub>2</sub> pipdt → Ni/mnt/Bz <sub>2</sub> pipdt (LMCT/LLCT)
d <sup>1</sup> A	HOMO-5 → LUMO,	77%	2.84	<b>3.18</b>	0.041 1	Bz <sub>2</sub> pipdt/mnt → Bz <sub>2</sub> pipdt (ILCT/LLCT)
	HOMO-9 → LUMO,	13%				Bz <sub>2</sub> pipdt/mnt → Bz <sub>2</sub> pipdt (LLCT/ILCTT)
e <sup>1</sup> B	HOMO-12 → LUMO+2,	61%	2.86		0.011 4	Ni/mnt → Ni/mnt/Bz <sub>2</sub> pipdt (MLCT)
	HOMO-4 → LUMO,	24%				Bz <sub>2</sub> pipdt/mnt → Bz <sub>2</sub> pipdt (IL/LLCT)
f <sup>1</sup> B	HOMO-4 → LUMO,	66%	2.89		0.027 6	Bz <sub>2</sub> pipdt/mnt → Bz <sub>2</sub> pipdt (IL/LLCT)
	HOMO-12 → LUMO+2,	21%				Ni/mnt → Ni/mnt/Bz <sub>2</sub> pipdt (MLCT)
e <sup>1</sup> A	HOMO-3 → LUMO,	35%	2.95		0.008 5	Ni/Bz <sub>2</sub> pipdt/mnt → Bz <sub>2</sub> pipdt (MLCT/LLCT)
	HOMO-3 → LUMO+2,	18%				Ni/Bz <sub>2</sub> pipdt/mnt → Ni/mnt/Bz <sub>2</sub> pipdt (LMCT/ <i>deloc.</i> )
	HOMO → LUMO+2,	16%				mnt/Ni/Bz <sub>2</sub> pipdt → Ni/mnt/Bz <sub>2</sub> pipdt (LMCT)

**Table A.5:** TDDFT calculated energies and compositions of the lowest lying singlet electronic transitions of **3a**. The principal singlet transition responsible for the main absorption band in the visible region is shown in bold.

State	Composition	$\Delta E$	Exp.	$F$	Character
<b>b<sup>1</sup>A</b>	<b>HOMO → LUMO, 84%</b>	<b>1.81</b>	<b>1.90</b>	<b>0.1532</b>	<b>mnt/Pd/Bz<sub>2</sub>pipdt → Bz<sub>2</sub>pipdt (MMLCT)</b>
a <sup>1</sup> B	HOMO → LUMO+1, 89%	2.11	2.21sh	0.0166	mnt/Pd/Bz <sub>2</sub> pipdt → mnt/Pd/Bz <sub>2</sub> pipdt
d <sup>1</sup> A	HOMO-2 → LUMO, 45% HOMO-4 → LUMO, 18% HOMO → LUMO+2, 14% HOMO-4 → LUMO+1, 13%	2.95	3.03	0.0515	Bz <sub>2</sub> pipdt/Pd → Bz <sub>2</sub> pipdt (IL/MLCT) Pd/Bz <sub>2</sub> pipdt/mnt → Bz <sub>2</sub> pipdt (MLCT/LLCT) mnt/Pd/Bz <sub>2</sub> pipdt → mnt (ILCT/MLCT) Pd/Bz <sub>2</sub> pipdt/mnt → mnt/Pd/Bz <sub>2</sub> pipdt (MLCT)
e <sup>1</sup> A	HOMO → LUMO+2, 14% HOMO-4 → LUMO, HOMO-4 → LUMO+1, HOMO-2 → LUMO, 12%	2.98		0.0132	mnt/Pd/Bz <sub>2</sub> pipdt → mnt (ILCT/MLCT) Pd/Bz <sub>2</sub> pipdt/mnt → Bz <sub>2</sub> pipdt Pd/Bz <sub>2</sub> pipdt/mnt → Bz <sub>2</sub> pipdt/Pd → Bz <sub>2</sub> pipdt (IL/MLCT)
e <sup>1</sup> B	HOMO-5 → LUMO, 58% HOMO-9 → LUMO, 35%	3.15	3.23	0.0088	Bz <sub>2</sub> pipdt → Bz <sub>2</sub> pipdt (IL) Bz <sub>2</sub> pipdt/mnt → Bz <sub>2</sub> pipdt (LLCT/ILCT)
f <sup>1</sup> A	HOMO-6 → LUMO, 97%	3.18		0.0041	Bz <sub>2</sub> pipdt → Bz <sub>2</sub> pipdt (IL)

**Table A6:** TDDFT calculated energies and compositions of the lowest lying singlet electronic transitions of **3b**. The principal singlet transition responsible for the main absorption band in the visible region is shown in bold.



Appendix

State	Composition	$\Delta E$	Exp.	$F$	Character
<b>b<sup>1</sup>A</b>	<b>HOMO → LUMO, 82%</b>	<b>1.84</b>	<b>1.81</b>	<b>0.2638</b>	<b>mnt/Pt/Bz<sub>2</sub>pipdt → Bz<sub>2</sub>pipdt (MMLL'CT)</b>
c <sup>1</sup> A	HOMO → LUMO+2, 95%	2.72		0.0021	mnt/Pt/Bz <sub>2</sub> pipdt → mnt/Pt/Bz <sub>2</sub> pipdt (LMCT/LLCT)
d <sup>1</sup> B	HOMO → LUMO+1, 64%	2.98	2.97	0.1064	mnt/Bz <sub>2</sub> pipdt/Pt → mnt/Pt/Bz <sub>2</sub> pipdt (LMCT)
	HOMO-2 → LUMO, 17%				
e <sup>1</sup> A	HOMO-5 → LUMO, 98%	3.18		0.0031	Bz <sub>2</sub> pipdt → Bz <sub>2</sub> pipdt (IL)
e <sup>1</sup> B	HOMO-6 → LUMO, 59%	3.18	3.21	0.0024	Bz <sub>2</sub> pipdt/Pt/mnt → Bz <sub>2</sub> pipdt (IL/MLCT)
	HOMO-4 → LUMO, 40%				
f <sup>1</sup> A	HOMO-9 → LUMO, 53%	3.32		0.0687	Bz <sub>2</sub> pipdt/mnt/Pt → Bz <sub>2</sub> pipdt (LLCT/IL)
	HOMO-7 → LUMO, 39%				Bz <sub>2</sub> pipdt/mnt/Pt → Bz <sub>2</sub> pipdt (LLCT/MLCT)

**Table A7:** TDDFT calculated energies and compositions of the lowest lying singlet and triplet electronic transitions of **3c**. The principal singlet transition responsible for the main absorption band in the visible region is shown in bold.

## **A.7 Optically Transparent Thin-Layer Cell (OTTLE)**

Various spectrophotometric methods are suitable for monitoring the spectral changes associated with the changes in the redox state of the system brought about by the applied potentials.

The use of an Optically Transparent Thin Layer Electrode (OTTLE) technique is ideal for Uv-vis spectral monitoring of redox profiles as it requires only a very small sample volume and allows for maximum exposure of the sample to the electrode surface.

This allows the detection and identification of an electrogenerated product by observing changes in absorption bands, such as position and intensity, as well as observation of new bands, after the application of a potential. With this information the character of the frontier orbitals of a complex can be inferred. Figure A.9 shows a typical OTTLE study for the oxidation of a metal dithiolene complex. The original neutral complex absorption spectrum is shown in black. Following application of a suitable potential to the OTTLE cell the absorption bands may grow or reduce in intensity depending on the nature of the absorption transition and the nature of the oxidised species being produced. The applied potential is usually chosen to be slightly past the peak potential of the redox process of interest.

Each successive scan takes ten minutes and scans are continually taken until the absorption spectra cease to change. At this point the potential is reversed and the reversibility of the study investigated.

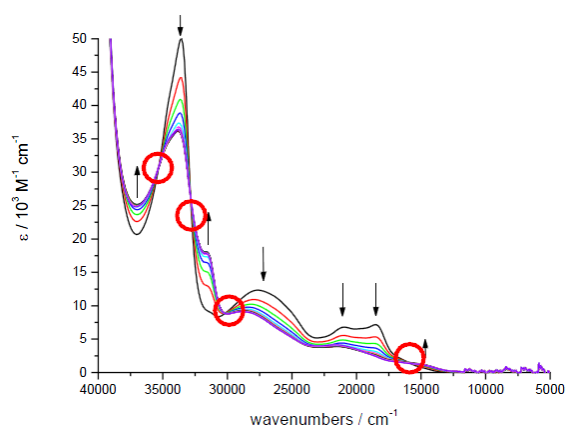


**Figure A.9:** Example OTTLE spectrum showing typical growth and collapse of absorption bands upon oxidation of the solution. Arrows indicate whether the band is growing or collapsing upon oxidation and isosbestic points are circled.

The original neutral spectrum should be reproduced indicating a fully reversible redox process, if the neutral spectrum is not reproduced then this indicates an irreversible redox process. Isosbestic points (indicated in Figure 4.3 by red circles) are important features in OTTLE spectra as they show a clean conversion between two absorbing chemical species in the study. If there is a third species involved, *i.e.* an irreversible redox process resulting in a third species, then the point at which the absorption spectra overlap will no longer be at a single wavenumber but will vary over progressively changing wavenumbers. Conclusions about the nature of the oxidised species being studied are drawn by comparison to spectroelectrochemical

studies of similar complexes or ligands carried out elsewhere in this thesis or to literature studies.

A quartz cell containing a Pt/Rh gauze working electrode was placed in a Teflon block with a quartz window (Figure A.10). The working electrode wire that extends into the cell reservoir was covered by a Teflon coat to prevent bulk electrolysis. The reservoir was itself covered with a Teflon cap and the electrodes fitted through this. Both the reference and the counter electrode were placed in salt bridges. The temperature of the cell was monitored using a thermocouple and reduced to -40 °C using pre-cooled nitrogen gas. To prevent frosting of the cell, room temperature nitrogen was also passed through the cell.

UV/Vis/n-IR spectra were recorded repeatedly before, during and after application of a potential to the cell. After application of a potential the true spectrum of the electrogenerated species is obtained when no further change in the spectrum was observed after numerous scans.

The original non-oxidised/reduced species was regenerated by returning the potential to a suitable value: in this work a potential of -0.2 V for an oxidative study and +0.1V for a reductive study were used.

The quartz cell used was 0.5 mm thick, the working electrode a Pt/Rh gauze, the counter electrode was a Pt wire and the reference electrode Ag/AgCl. A Perkin-Elmer Lambda 9 spectrophotometer, linked to a PC running UV/Winlab software was used to record the spectra. All samples were studied at 253 K in either 0.1 M TBABF<sub>4</sub>/DMF.

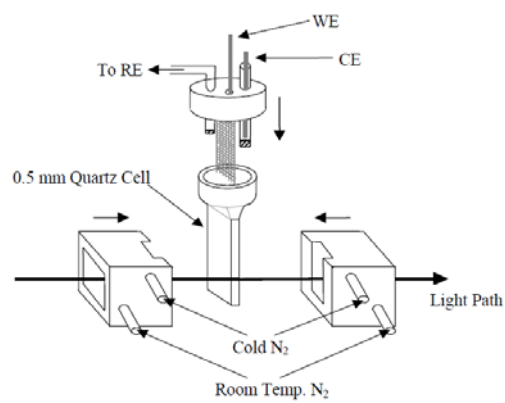


**Figure A.10:** A three electrode electrochemical cell setup used for in situ measurement of the electronic absorption spectra upon an applied potential (E). The working electrode (WE), counter electrode (CE) and reference electrode (RE) are housed in a quartz cell, and held in place by a Teflon cap.

## A.8 Coordination ability of Me<sub>2</sub>pipto with Fe(III)

A suspension of Fe<sub>2</sub>(SO<sub>4</sub>)<sub>3</sub> in CH<sub>3</sub>CN was added drop-wise to a solution of Me<sub>2</sub>pipto in the same solvent; after adding few drops of H<sub>2</sub>SO<sub>4</sub> 96% the solution turned orange. The addition of NaBF<sub>4</sub> turned the solution to red-violet during the stirring at reflux (3 h). The solvent was evaporated and the crude product dissolved with CH<sub>3</sub>CN (60 ml). The corresponding solution was filtered to separate a white solid which was dried with Na<sub>2</sub>SO<sub>4</sub>. The addition of THF caused the formation of a white precipitate that was removed before a drop-wise addition of diethyl ether; the lacquer formed became slowly a crystalline solid that was recrystallised from acetone/Et<sub>2</sub>O; the precipitate was collected by filtration and washed with diethyl ether.

To investigate further on the potential of this ligand in tuning the properties of selected metal complexes, due to soft/hard character of the donor atoms, it has allowed Me<sub>2</sub>pipto and Me<sub>2</sub>pipdt to react with FeCl<sub>3</sub> in CH<sub>3</sub>CN solution, in the same experimental conditions. The obtained products are [Fe(Me<sub>2</sub>pipto)<sub>2</sub>Cl<sub>2</sub>](BF<sub>4</sub>) and [Fe(Me<sub>2</sub>pipdt)<sub>3</sub>](BF<sub>4</sub>)<sub>2</sub> (**8a**).

Using as source of FeSO<sub>4</sub>, to avoid the presence of more coordinating Cl<sup>-</sup> anion, the [Fe(Me<sub>2</sub>pipto)<sub>3</sub>](BF<sub>4</sub>)<sub>2</sub> (**8a**) complex was obtained. The crystal structure of **8a** is shown in Fig. A.11.

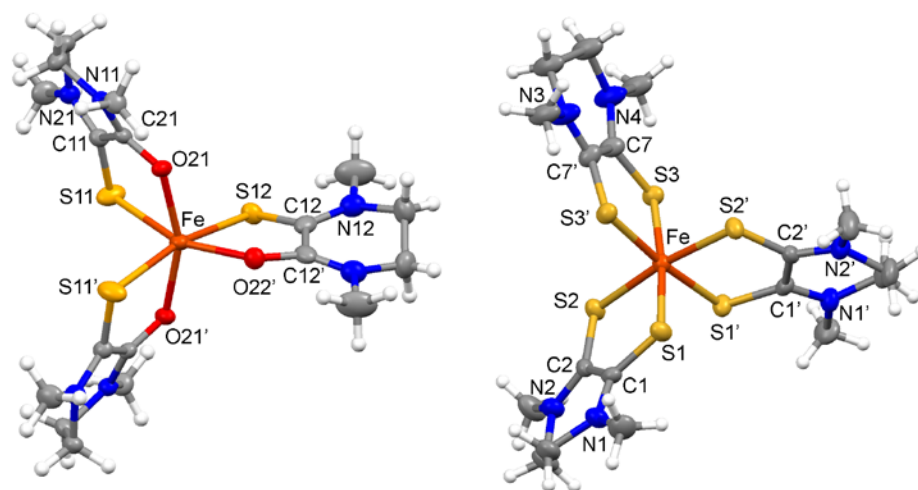


**Figure A11:** Molecular drawing of  $[\text{Fe}(\text{Me}_2\text{pipto})_3]^{2+}$  with thermal ellipsoids at the 30% probability level; the  $\text{BF}_4^-$  anions have been removed for clarity. Symmetry code ' =  $-x+1, y, -z+1/2$ . Molecular drawing of  $[\text{Fe}(\text{Me}_2\text{pipdt})_3]^{2+}$  with thermal ellipsoids at the 30% probability level; the  $\text{BF}_4^-$  anions have been removed for clarity. Symmetry code ' =  $1-x; y; 1/2-z$ .

Three bidentate SO donor ligands define the octahedral geometry of the metal. The complex lies on a binary axis so that one ligand is found disordered in two equivalent positions. For both of the images, the disposition of the sulfur and oxygen atoms is such that the complex exhibits a *mer* configuration. The considerations made for the ligand (bond distances reflected by related vibrational markers) in the nickel complex do apply also to the iron case.

Interestingly, the iron ion results to be reduced to the 2+ oxidation state and preliminary magnetic measurements on these complexes show that, in the same 400-5 K range, Fe(II) exhibits high spin state in **8a**, but low-spin magnetic behaviour in  $[\text{Fe}(\text{Me}_2\text{pipdt})_3](\text{BF}_4)_2$ . The different magnetic behaviour can be explained by the difference in the  $\pi$ -acceptor capability of the ligands. In fact, in the case of the dithione the  $\pi$ -back-donation, which stabilizes the  $t_{2g}$  orbitals of the metal ion, is stronger when the separation's energy between the  $d$  orbitals of the  $\text{Me}_2\text{pipto}$  is higher than  $10Dq$ . Consequently, the ligand is more stable in the low-spin state.

In  $[\text{Fe}(\text{Me}_2\text{pipto})_2\text{Cl}_2](\text{BF}_4)$  (see Figure A.12) the metal adopts a distorted octahedral geometry defined by two chloride anions in *cis* position and by two chelate S, O ligands.

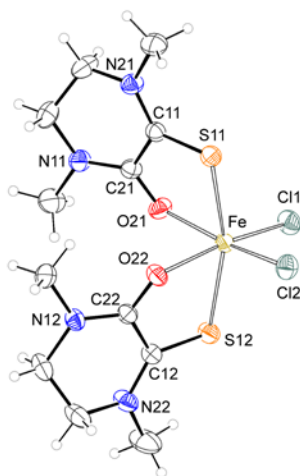


**Figure A12:** Ortep drawing of  $[\text{Fe}(\text{Me}_2\text{pipto})_2\text{Cl}_2]^+$  with thermal ellipsoids at the 30% probability level. The  $\text{BF}_4^-$  anion has been removed for clarity.



The sulfur atoms are located in *trans* position. The distortion from the ideal geometry is a consequence of the S,O ligands bite angles ( $\sim 80^\circ$ ) that results in the considerable decrease of the S(11)-Fe-S(12) ( $163.30(2)^\circ$ ), Cl(2)-Fe-O(21) ( $165.22(4)^\circ$ ), and Cl(1)-Fe-O(22) ( $166.04(4)^\circ$ ) angles.

The metal oxygen bond distances ( $\sim 2.08 \text{ \AA}$ ) are significantly shorter than the metal-chloride ( $\sim 2.26 \text{ \AA}$ ), or metal-sulfur ones ( $\sim 2.47 \text{ \AA}$ ). The arrangement of the ligands corresponds to the  $\Lambda$  configuration; in addition, the two ligands adopt different conformation of the ethylene bridge, so that the overall stereochemical descriptor for this molecular structure is  $\Lambda(\lambda\delta)$ . Since the space group is a non chiral one, both enantiomers are present in the unit cell:  $\Lambda(\lambda\delta)/\Delta(\delta\lambda)$ . As a consequence of metal coordination, the C=O and C=S bond distances are slightly longer than in the free ligand but they still exhibit a considerable double bond character.

Selected bond lengths (Å) and angles (°) for [Fe(Me2pipto) <sub>2</sub> Cl <sub>2</sub> ]BF <sub>4</sub>					
Fe-S(11)	2.5022(7)	C(12)-S(12)	1.679(2)	O(22)-Fe-S(12)	80.08(4)
Fe-S(12)	2.4595(6)	C(22)-O(22)	1.258(2)	O(21)-Fe-S(12)	87.37(4)
Fe-O(21)	2.101(1)	O(22)-Fe-O(21)	80.72(6)	Cl(2)-Fe-S(12)	105.15(3)
Fe-O(22)	2.071(2)	O(22)-Fe-Cl(2)	93.53(5)	Cl(1)-Fe-S(12)	87.13(2)
Fe-Cl(1)	2.2699(7)	O(21)-Fe-Cl(2)	165.22(4)	O(22)-Fe-S(11)	89.35(5)
Fe-Cl(2)	2.2592(6)	O(22)-Fe-Cl(1)	166.04(4)	Cl(2)-Fe-S(11)	88.26(2)
C(11)-S(11)	1.675(2)	O(21)-Fe-Cl(1)	93.23(5)	O(21)-Fe-S(11)	78.13(4)
C(21)-O(21)	1.248(2)	Cl(2)-Fe-Cl(1)	95.19(2)	Cl(1)-Fe-S(11)	101.78(3)

**Table A8:** Summary of X-ray crystallographic data for [Fe(Me2pipto)<sub>2</sub>Cl<sub>2</sub>]BF<sub>4</sub>.

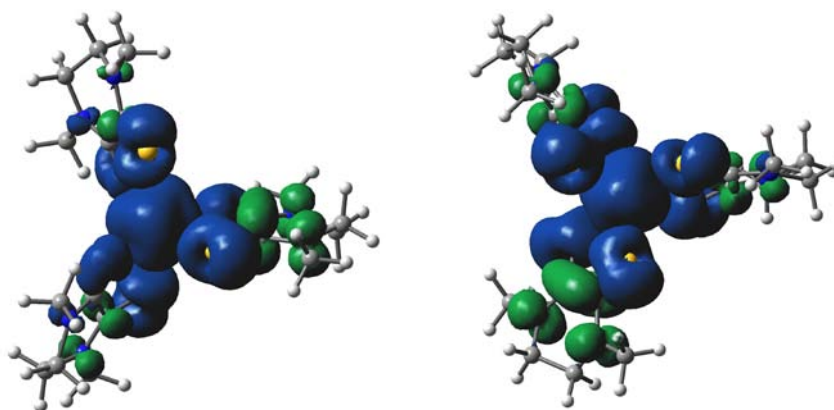
Crystallographic data for [Fe(Me <sub>2</sub> pipto) <sub>3</sub> ](BF <sub>4</sub> ) <sub>2</sub>			
Empirical formula	C <sub>18</sub> H <sub>30</sub> B <sub>2</sub> F <sub>8</sub> FeN <sub>6</sub> O <sub>3</sub> S <sub>3</sub>	<i>V</i> , Å <sup>3</sup>	2799(3)
Formula weight	704.13	<i>Z</i>	4
Crystal size, mm	0.55x0.45x0.30	<i>T</i> , K	293(2)
Crystal system	Monoclinic	$\rho$ (calc), Mg/m <sup>3</sup>	1.671
Space group	<i>C</i> 2/ <i>c</i>	$\mu$ , mm <sup>-1</sup>	0.851
<i>a</i> , Å	20.40(1)	$\theta$ range, deg.	2.25 to 26.00
<i>b</i> , Å	11.992(8)	No. of rflcn/obsv	13694 / 2731
<i>c</i> , Å	16.20(1)	Abs. struct. Param.	-
$\alpha$ , deg.	90	Goof	1.075
$\beta$ , deg.	129.60(2)	<i>R</i> 1	0.0547
$\gamma$ , deg.	90	<i>wR</i> 2	0.1429

Table A9: Summary of X-ray crystallographic data for [Fe(Me<sub>2</sub>pipto)<sub>3</sub>](BF<sub>4</sub>)<sub>2</sub>

## A 8.1 DFT calculations

DFT calculations were carried out using the Gaussian 03 program suite. The geometry optimizations of [Fe(Me<sub>2</sub>pipto)<sub>3</sub>]<sup>2+</sup> and [Fe(Me<sub>2</sub>pipdt)<sub>3</sub>]<sup>2+</sup> were performed starting from the X-ray geometries for both the singlet (S=0) and quintet (S=2) states, using the pure density functional OLYP and the 6-31G(d) basis set. Vibrational frequencies were calculated at the same level of theory to ensure that the stationary points were true minima. Single point calculations were performed with the OLYP and B3LYP density functionals and with the 6-311G(d) basis set.

To support our conclusions concerning the magnetic properties of the  $[\text{Fe}(\text{Me}_2\text{pipto})_3]^{2+}$  complex, a DFT study was performed, for comparison, on both  $[\text{Fe}(\text{Me}_2\text{pipto})_3]^{2+}$  and  $[\text{Fe}(\text{Me}_2\text{pipdt})_3]^{2+}$  complexes using two different density functionals: pure OLYP and hybrid B3LYP.



**Figure A13:** Spin density contour plot for  $[\text{Fe}(\text{Me}_2\text{pipto})_3]^{2+}$  (above) and  $[\text{Fe}(\text{Me}_2\text{pipdt})_3]^{2+}$  (below) in the quintet spin state ( $S=2$ ). The isodensity value is 0.0008 a.u. (OLYP/6-311G(d)).

The geometries were optimized with the OLYP functional for the singlet ( $S=0$ ) and quintet ( $S=2$ ) states (supporting information). The choice of this functional was made on the basis of the good performances in predicting the ground states of a number of iron complexes. From a comparison of the experimental and calculated bond distances, the preferred ground states for  $[\text{Fe}(\text{Me}_2\text{pipto})_3]^{2+}$  and  $[\text{Fe}(\text{Me}_2\text{pipdt})_3]^{2+}$  complexes are the  $S=2$  and  $S=0$ , respectively. With the OLYP functional,  $[\text{Fe}(\text{Me}_2\text{pipto})_3]^{2+}$  exhibits an energy

preference for the S=2 state over the S=0 one of 60.14 kJ/mol, whereas  $[\text{Fe}(\text{Me}_2\text{pipdt})_3]^{2+}$  favours the S=0 state over the S=2 one by 31.88 kJ/mol. The spin density of  $[\text{Fe}(\text{Me}_2\text{pipto})_3]^{2+}$  in the quintet state is located primarily on the iron atom and to a minor extent over the sulphur and oxygen atoms, Figure A.13. A different scenario is encountered when using the B3LYP functional, since it decisively favours the S=2 state for both compounds. This is nevertheless in line with the property of this density functional that tends to overstabilize high spin states.

## A 8.2 Experimental Details

**$[\text{Fe}(\text{Me}_2\text{pipto})_3](\text{BF}_4)_2$  (8a).** *Synthesis:* 316.0 mg (2.0 mmol) of **1** in 40 ml of  $\text{CH}_3\text{CN}$ , yellow solution, was added drop-wise to a suspension of  $\text{Fe}_2(\text{SO}_4)_2$  (133.0 mg, 0.34 mmol) in the same solvent (50 ml); after adding of few drops of  $\text{H}_2\text{SO}_4$  96% the solution turned orange. After the addition of 240 mg of  $\text{NaBF}_4$  (2.2 mmol) the solution turned red-violet during the stirring at reflux (3 h). The solvent was evaporated and the crude product dissolved with  $\text{CH}_3\text{CN}$  (60 ml) and the corresponding solution was filtered, to separate a white solid, and then made anhydrous with  $\text{Na}_2\text{SO}_4$ . The addition of THF caused the formation of a white precipitate that was removed before a drop-wise addition of diethyl ether; the lacca formed, became slowly a crystalline solid that was recrystallized from acetone/ $\text{Et}_2\text{O}$ ; the precipitate was collected by

filtration and washed with diethyl ether (three times) (yield 55.4 mg, 0.078 mmol; 23.4%). Analytical results are in accordance with the formula  $[\text{Fe}(\text{Me}_2\text{pipto})_3](\text{BF}_4)_2$ . *Elemental Analysis:* calculated for  $\text{C}_{18}\text{H}_{30}\text{N}_6\text{O}_3\text{S}_3\text{FeB}_2\text{F}_8$  (704.11): C 30.70, H 4.29, N 11.94, S 13.66; found: C 31.00, H 3.91, N 11.94, S 13.30. *UV-vis* (in  $\text{CH}_3\text{CN}$  solution):  $\epsilon/\text{nm}$  ( $\epsilon/\text{mol}\cdot\text{cm}^{-1}\cdot\text{dm}^{-3}$ ) 530 (400); 430 (500); 310 ( $1.73\cdot 10^4$ ); 270 ( $1.63\cdot 10^4$ ). *FT-IR* (KBr):  $\nu_{\text{max}}/\text{cm}^{-1}$  2930(w); 2859(vw); 1639(vs); 1558(vs); 1507(w); 1489(w); 1439(w); 1404(mw); 1369(m); 1262(w); 1208(mw); 1160(w); 1083(ms); 1054(s); 961(w); 896(w); 830(vw); 755(w); 695(w); 668(vw); 584(mw); 521(w); 501(vw); 418(m).

## A.9 Photoluminescence studies

Photoluminescence measurements have been performed by Prof. Alberto Juris of the University of Bologna. Photoluminescence spectra of all the complexes in DMF solution at room temperature, show a broad band centred at about 1070 nm. However this band is very weak if compared to the signal of the reference, and therefore cannot be reliably attributed to complexes emission. Photoluminescence spectra acquired at 77K do not show any emission.

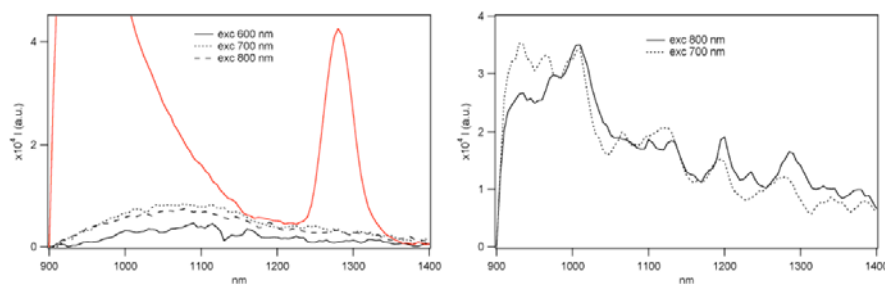


**Figure A14:** Pholuminescence spectra of [Pt(Bz<sub>2</sub>pipdt)(dmit)] at RT (left) and at 77K (right).

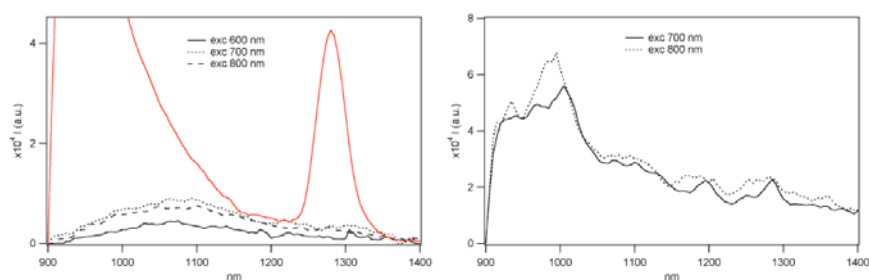


**Figure A15:** Pholuminescence spectra of [Pt(Bz<sub>2</sub>pipdt)(dsit)] at RT (left) and at 77K (right).

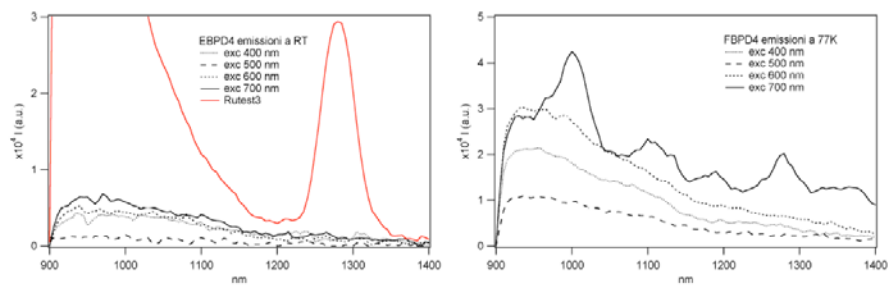


**Figure A16:** Photoluminescence spectra of [Pt(IPr<sub>2</sub>pipdt)(mnt)] at RT (left) and at 77K (right).





---

## *Bibliography*



- [1] (a) C. Faulmann, P. Cassoux, in: E.I. Stiefel (Ed.), *Dithiolene Chemistry: Synthesis, Properties, and Applications*, Progress in Inorganic Chemistry, vol. 52, Wiley, Chichester, 2004, p. 399; (b) H. Tanaka, Y. Okano, H. Kobayashi, W. Suzuki, A. Kobayashi, *Science* 291(2001) 285.
- [2] A.T. Coomber, D. Beljonne, R.H. Friend, J.K. Bredas, A. Charlton, N. Robertson, A.E. Underhill, M. Kurmoo, P. Day, *Nature* 380 (1996) 144.
- [3] U.T. Mueller-Westerhoff, in: G. Wilkinson (Ed.), *Comprehensive Coordination Chemistry*, Pergamon, Oxford, 1987, p. 595.
- [4] a) W.L. Tan, W. Ji, J.L. Zuo, J.F. Bai, X.Z. You, Y.H. Lim, S. Yang, D.J. Hagan, E.W. Van Stryland, *Appl. Phys. B70* (2000) 809; (b) B.J. Coe, in: J.A. McCleverty, T.J. Meyer (Eds.), *Comprehensive Coordination Chemistry II*, vol. 9, Elsevier–Pergamon, Oxford, 2004, p. 621.
- [5] J.M. Tunney, J. McMaster, C.D. Garner, in: J.A. McCleverty, T.J. Meyer (Eds.), *Comprehensive Coordination Chemistry II*, vol. 8, Elsevier–Pergamon, Oxford, 2004, p. 459.
- [6] a) S. Curreli, P. Deplano, C. Faulmann, A. Ienco, C. Mealli, M.L. Mercuri, L. Pilia, G. Pintus, A. Serpe & E.F. Trogu. Electronic factors affecting second-order NLO properties: case study of four different push-pull bis-dithiolene nickel complexes. *Inorg. Chem.*, vol. 43, no. 16, pages 5069-5079, 2004; b) P. Deplano, L. Pilia, D. Espa, M.L. Mercuri & A. Serpe. Square-planar d<sup>8</sup> metal mixed-ligand dithiolene complexes as second order nonlinear optical chromophores: structure/property relationship. *Coord. Chem. Rev.*, vol. 254, pages 1434-1447, 2010.
- [7] N. Robertson & L. Cronin. Metal bis-1,2-dithiolene complexes in conducting or magnetic crystalline assemblies. *Coord. Chem. Rev.*, vol. 227, pages 93-127, 2002.
- [8] a) J.-Y. Cho, B. Domercq, S.C. Jones, J. Yu, X. Zhang, Z. An, M. Bishop, S. Barlow, S.R. Marder & B. Kippelen. High electron mobility in nickel bis(dithiolene) complexes. *J. Mater. Chem.*, vol. 17, pages 2642-2647, 2007.
- [9] J.P.M. Nunes, M.J. Figueira, D. Belo, I.C. Santos, B. Ribeiro, E.B. Lopes, R.T. Henriques, J. Vidal-Gancedo, J. Veciana, C. Rovira & M. Almeida. Transition metal bisdithiolene complexes based on extended ligands with fused tetrathiafulvalene and

- thiophene moieties: new single-component molecular metals. *Chem. Eur. J.*, vol. 13, pages 9841-9849, 2007.
- [10] P. Cassoux. Molecular (super)conductors derived from bis-dithiolate metal complexes. *Coord. Chem. Rev.*, vol. 185-186, pages 213-232, 1999.
- [11] a) U.T. Mueller-Westerho, B. Vance & D.I. Yoon. The synthesis of dithiolenes with strong near-IR absorption. *Tetrahedron*, vol. 47, no. 6, pages 909-932, 1991.  
b) P. Deplano, M.L. Mercuri, A. Serpe, L. Pilia, in: J. Zabicky (Ed.), *Structure and Properties of d8-Metal Dithiolenes*: Chapter 16 in *The Chemistry of Metal Enolates*, Wiley & Sons, Ltd, 2009, p. 879.
- [12] J. Fabian, H. Nakazumi & M. Matsuoka. Near-infrared absorbing dyes. *Chem. Rev.*, vol. 92, pages 1197-1226, 1992.
- [13] S.M. Kuebler & R.G. Denning. Population gratings in degenerate four-wave mixing studies of a nickel dithiolenes at 1064 nm. *Chem. Phys. Lett.*, vol. 250, pages 120-127, 1996.
- [14] C. Faulmann & P. Cassoux. Solid-state properties (electronic, magnetic, optical) of dithiolenes complex-based compounds. *Prog. Inorg. Chem.*, vol. 52, pages 399-489, 2004.
- [15] (a) C. Zhan, W. Xu, D. Zhang, D. Li, Z. Lu, Y. Nie, D. Zhu, *J. Mater. Chem.* 12 (2002) 2945; (b) C.S. Winter, S.N. Oliver, J.D. Rush, C.A.S. Hill, A.E. Underhill, *J. Appl. Phys.* 71 (1992) 512.
- [16] (a) G. Periyasamy, N.A. Burton, I.H. Hillier, M.A. Vincent, H. Disley, J. McMaster, C.D. Garner, *Faraday Discuss.* 135 (2007) 469; (b) M.L. Kirk, R.L. McNaughton, M.E. Helton, in: E.I. Stiefel (Ed.), *Dithiolenes Chemistry: Synthesis, Properties, and Applications*, *Progress in Inorganic Chemistry*, vol. 52, Wiley, Chichester, 2004, p. 111, and references therein.
- [17] K. Jørgensen, *Coord. Chem. Rev.* 1 (1966) 164.
- [18] M.D. Ward, J.A. McCleverty, *J. Chem. Soc.: Dalton Trans.* (2002) 275.
- [19] F. Bigoli, P. Deplano, M.L. Mercuri, M.A. Pellinghelli, L. Pilia, G. Pintus, A. Serpe, E.F. Trogu, *Inorg. Chem.* 41 (2002) 5241.

- [20] S. Curreli, P. Deplano, C. Faulmann, A. Ienco, C. Mealli, M.L. Mercuri, L. Pilia, G. Pintus, A. Serpe, E.F. Trogu, *Inorg. Chem.* 43 (2004) 5069.
- [21] R.K. Szilagy, B.S. Lim, T. Glaser, R.H. Holm, B. Hedman, K.O. Hodgson, E.I. Solomon, *J. Am. Chem. Soc.* 125 (2003) 9158.
- [22] (a) Z.S. Herman, R.F. Kirchner, G.H. Loew, U.T. Mueller-Westerhoff, A. Nazal, M.C. Zerner, *Inorg. Chem.* 21 (1982) 46; (b) J. Weber, C. Daul, A. Van Zelewsky, A. Goursot, E. Penigault, *Chem. Phys. Lett.* 88 (1982) 78; (c) C. Lauterbach, J. Fabian, *Eur. J. Inorg. Chem.* (1999) 1995; (d) C. Aragoni, M. Arca, F. Demartin, F.A. Devillanova, A. Garau, F. Isaia, F. Lejl, V. Lippolis, G. Verani, *J. Am. Chem. Soc.* 121 (1999) 7098; (e) T.-M. Yao, J.-L. Zuo, F. You, X.Z. You, *Polyhedron* 14 (1995) 1487.
- [23] B.S. Lim, D.V. Fomitchev, R.H. Holm, *Inorg. Chem.* 40 (2001) 4257.
- [24] F. Bigoli, P. Cassoux, P. Deplano, M.L. Mercuri, M.A. Pellinghelli, G. Pintus, A. Serpe, E.F. Trogu, *J. Chem. Soc.: Dalton Trans.* (2000) 4639.
- [25] F. Bigoli, C.-T. Chen, W.-C. Wu, P. Deplano, M.L. Mercuri, M.A. Pellinghelli, L. Pilia, G. Pintus, A. Serpe, E.F. Trogu, *Chem. Commun.* (2001) 2246.
- [26] C.-T. Chen, S.-Y. Liao, K.-J. Lin, L.-L. Lai, *Adv. Mater.* 3 (1998) 335.
- [27] (a) S.D. Cummings, R. Eisenberg, E.I. Stiefel (Eds.), *Dithiolene Chemistry: Synthesis, Properties, and Applications*, *Progress in Inorganic Chemistry*, vol. 52, Wiley, Chichester, 2004, p. 315; (b) J.A. Weinstein, M.T. Tierney, E. Stephen Davies, K. Base, A.A. Robeiro, M.A. Grinstaff, *Inorg. Chem.* 45 (2006) 4544.
- [28] (a) J.S. Pap, F.L. Benedito, E. Bothe, E. Bill, S. De Beer George, T. Weyhermuller, K. Wieghardt, *Inorg. Chem.* 46 (2007) 4187; (b) B.W. Smucker, J.M. Hudson, M.A. Omary, K.R. Dunbar, *Inorg. Chem.* 42 (2003) 4714.
- [29] (a) C. Makedonas, C.A. Mitsopoulou, F.J. Lahoz, A.I. Balana, *Inorg. Chem.* 42 (2003) 8853; (b) C. Makedonas, C.A. Mitsopoulou, *Inorg. Chim. Acta* 360 (2007) 3997; (c) E.A.M. Geary, N. Hirata, J. Clifford, J. Durrant, S. Parson, A. Dawson, L.J. Yellowlees, N. Robertson, *Dalton Trans.* (2003) 3757; (d) E.A.M. Geary, L.J. Yellowlees, L.A. Jack, S. Parson, N. Hirata, J. Durrant, N. Robertson, *Inorg. Chem.* 44 (2005) 242.
- [30] J. Zhang, P. Du, J. Schneider, P. Jarosz, R. Eisenberg, *J. Am. Chem. Soc.* 129 (2007) 7726.

- [31] C.-T. Chen, S.-Y. Liao, K.-J. Lin, C.-H. Chen, T.-Y.J. Lin, *Inorg. Chem.* **38** (1999) 2734.
- [32] S.D. Cummings, L.-T. Cheng, R. Eisenberg, *Chem. Mater.* **9** (1997) 440.
- [33] J.L. Oudar, *J. Chem. Phys.* **67** (1977) 446.
- [34] A. Davison, J. A. McCleverty, E. T. Shawl and E. J. Wharton, *J. Am. Chem. Soc.*, **89**, 830 (1967).
- [35] a) R. Kato, Y. Kashimura, H. Sawa and Y. Okano, *Chem. Lett.*, 921 (1997);  
b) Y. Kashimura, Y. Okano, J.-I. Yamaura and R. Kato, *Synth. Met.*, **103**, 2123 (1999).
- [36] S. Dalglish, C.A. Morrison, D.S. Middlemiss, A.R. Mount, A. Collins, L. Pilia, P. Deplano, M.L. Mercuri, A. Serpe, P.J. Murphy, N. Robertson, *J. Mater. Chem.* **19** (2009), 6194–6200.
- [37] L. Pilia, F. Artizzu, C. Faulmann, M.L. Mercuri, A. Serpe, P. Deplano, *Inorg. Chem. Commun.* **12** (2009) 490.
- [38] F. Bigoli, C.-T. Chen, P. Deplano, M.L. Mercuri, M.A. Pellinghelli, G. Piras, A. Serpe, E.F. Trogu, *Atti del XXVII Congresso di Chimica Inorganica*, Como 27 Giugno–1 Luglio, 1999, p. O56.
- [39] Pd(CH<sub>3</sub>CN)Cl<sub>2</sub> is provided by Sigma Aldrich, [Pt(DMSO)<sub>2</sub>Cl<sub>2</sub>] is prepared according to Kukushkin, Y. N.; Viez'menskii, Y. E.; Zorina, L. I.; *Russ. J. Inorg. Chem.* **1968**, 835.
- [40] S. Di Bella, *Chem. Soc. Rev.* **30** (2001) 355.
- [41] Cariati, E.; Pizzotti M.; Roberto D.; Tessore F.; Ugo R.; *Coord. Chem. Rev.* **2006**, 250, 1210-1233.
- [42] (a) H.S. Nalwa, *Appl. Organomet. Chem.* **5** (1991) 349; (b) J. Zyss, *Molecular Nonlinear Optics*, Academic Press, New York, 1994; (c) N.J. Long, *Angew Chem. Int. Ed. Engl.* **34** (1995) 21; (d) J. Heck, S. Dabek, T. Meyer-Friedrichsen, H. Wong, *Coord. Chem. Rev.* **190–192** (1999) 1217; (e) D.M. Roundhill, J.P. Fackler, *Optoelectronic Properties of Inorganic Compounds*, Plenum Press, New York, 1999; (f) J. Heck, S. Dabek, T. Meyer-Friedrichsen, H. Wong, *Coord. Chem. Rev.* **190–192** (1999) 1217; (g) H. Le Bozec, T. Renouard, *Eur. J. Inorg. Chem.* (2000) 229; (h) P.G. Lacroix, *Eur. J. Inorg. Chem.* (2001) 339; (i) B.J. Coe, in: J.A. McCleverty, T.J. Meyer (Eds.), *Comprehensive Coordination Chemistry II*, vol. 9, Elsevier Pergamon, Oxford, UK, 2004, pp. 621–687; (k) B.J. Coe, N.R.M. Curati, *Comments Inorg. Chem.* **25** (2004) 147.

- [43] (a) J.L. Oudar, D.S. Chemla, *J. Chem. Phys.* 66 (1977) 2664; (b) J.L. Oudar, *J. Chem. Phys.* 67 (1977) 446; (c) J.L. Oudar, H. Le Person, *Opt. Commun.* 15 (1975) 258.
- [44] (a) B.F. Levine, C.G. Bethea, *Appl. Phys. Lett.* 24 (1974) 445; (b) K.D. Singer, A.F. Garito, *J. Chem. Phys.* 75 (1981) 3572; (c) I. Ledoux, J. Zyss, *Chem. Phys.* 73 (1982) 203.
- [45] (a) J. Zyss, I. Ledoux, *Chem. Rev.* 94 (1994) 77; (b) R.W. Terhune, P.D. Maker, C.M. Savage, *Phys. Rev. Lett.* 14 (1965) 681; (c) P.D. Maker, *Phys. Rev.* 1 (1970) 923; (d) K. Clays, A. Pearson, *Phys. Rev. Lett.* 66 (1991) 2980.
- [46] Base, K.; Tierney, M. T.; Fort, A.; Muller, J.; Grinstaff, M. W. *Inorg. Chem.* 1999, 38, 287.
- [47] Makedonas, C.; Mitsopoulou, C. A. *Inorg. Chim. Acta* 2007, 360, 3997-4009
- [48] a) Makedonas, C.; Mitsopoulou, C. A. *Eur. J. Inorg. Chem.* 2007, 4176-4189; b) Makedonas, C.; Mitsopoulou, C. A.; Lahoz, F. J.; Balana, A. I. *Inorg. Chem.* 2003, 42, 8853-8865;
- [49] a) Cummings, S. D.; Cheng, L. T.; Eisenberg, R. *Chem. Mater.* 1997, 9, 440-450; b) Cummings, S. D.; Eisenberg, R. *J. Am. Chem. Soc.* 1996, 118, 1949-1960; c) Cummings, S. D.; Cheng, L. T.; Eisenberg, R. *Chem. Mater.* 1997, 9, 440-450.
- [50] A. M. Bond, *Broadening Electrochemical Horizons*, Oxford University Press, Oxford, 2002.
- [51] P. Zanello, *Inorganic Electrochemistry*, Royal Society of Chemistry, Cambridge, 2003.
- [52] *Spectroelectrochemistry*, ed. W Kaim and A. Klein, Royal Society of Chemistry, Cambridge, 2008, and references therein.
- [53] R. Holze, *J. Solid State Electrochem.*, 2004, 8, 982.
- [54] K. Ashley and S. Pons, *Chem. Rev.*, 1988, 88, 673
- [55] M. Dias, P. Hudhomme, E. Levillain, L. Perri, Y. Sahin, F.-X Sauvage and C. Wartelle, *Electrochem. Commun.*, 2004, 6, 325.
- [56] P. D. Prenzler, R. Bramley, S. R. Downing and G. A. Health, *Electrochem Commun.*, 2000, 2, 516.
- [57] S. Dalglish. *Novel Deposition Methods for Metal Dithiolenes*. PhD thesis, University of Edinburgh, Department of Chemistry, 2010.

- [58] Pearson, R.G., Proc. Natl. Acad. Sci. USA, 1986, 83, 8440-8441
- [59] Gaussian 03, Revision C.02, Frisch, M. J.; Trucks, G. W.; Schlegel, H. B.; Scuseria, G. E.; Robb, M. A.; Cheeseman, J. R.; Montgomery, Jr., J. A.; Vreven, T.; Kudin, K. N.; Burant, J. C.; Millam, J. M.; Iyengar, S. S.; Tomasi, J.; Barone, V.; Mennucci, B.; Cossi, M.; Scalmani, G.; Rega, N.; Petersson, G. A.; Nakatsuji, H.; Hada, M.; Ehara, M.; Toyota, K.; Fukuda, R.; Hasegawa, J.; Ishida, M.; Nakajima, T.; Honda, Y.; Kitao, O.; Nakai, H.; Klene, M.; Li, X.; Knox, J. E.; Hratchian, H. P.; Cross, J. B.; Bakken, V.; Adamo, C.; Jaramillo, J.; Gomperts, R.; Stratmann, R. E.; Yazyev, O.; Austin, A. J.; Cammi, R.; Pomelli, C.; Ochterski, J. W.; Ayala, P. Y.; Morokuma, K.; Voth, G. A.; Salvador, P.; Dannenberg, J. J.; Zakrzewski, V. G.; Dapprich, S.; Daniels, A. D.; Strain, M. C.; Farkas, O.; Malick, D. K.; Rabuck, A. D.; Raghavachari, K.; Foresman, J. B.; Ortiz, J. V.; Cui, Q.; Baboul, A. G.; Clifford, S.; Cioslowski, J.; Stefanov, B. B.; Liu, G.; Liashenko, A.; Piskorz, P.; Komaromi, I.; Martin, R. L.; Fox, D. J.; Keith, T.; Al-Laham, M. A.; Peng, C. Y.; Nanayakkara, A.; Challacombe, M.; Gill, P. M. W.; Johnson, B.; Chen, W.; Wong, M. W.; Gonzalez, C.; and Pople, J. A. *Gaussian, Inc.*, Wallingford CT, **2004**.
- [60] Becke, A. D. Density-functional exchange-energy approximation with correct asymptotic behavior. *Physical Review A: Atomic, Molecular, and Optical Physics* 38, 3098-3100. 1988.
- [61] Becke, A. D. Density-Functional Thermochemistry .3. the Role of Exact Exchange. *Journal of Chemical Physics* **1993**, 98 (7), 5648-5652.
- [62] R. Ditchfield, W. J. Hehre, and J. A. Pople, *J. Chem. Phys.* **54**, 724 (1971).
- [63] V. A. Rassolov, M. A. Ratner, J. A. Pople, P. C. Redfern, and L. A. Curtiss, *J. Comp. Chem.* **22**, 976 (2001).
- [64] GaussView, Version 3.09, R. Dennington II, T. Keith, J. Millam, K. Eppinnett, W. L. Hovell and R. Gilliland, Semichem, Inc., Shawnee Mission, KS, 2003.

*Bibliography*

---



---

*List of publications*



*List of publications*

---

Davide Espa, Luca Pilia, Luciano Marchiò, Maria Laura Mercuri, Angela Serpe, Alberto Barsella, Alain Fort, Simon J. Dalgleish, Neil Robertson and Paola Deplano *"Redox Switchable Chromophores based on Metal (Ni, Pd, Pt) Mixed-Ligand Dithiolene Complexes Showing Molecular Second-order NLO Activity"*. Inorganic Chemistry; Available online DOI:10.1021/ic102343g

L. Pilia, F. Artizzu, D. Espa, L. Marchiò, M. L. Mercuri, A. Serpe and P. Deplano, *New sulfur-oxygen mixed-donor ligand N,N-dimethyl-piperazine-3-oxo-2-thione (Me<sub>2</sub>pipto) and its Ni(II) and Fe(II) complexes*. Dalton Transactions, 39, 8139-8142, 2010. ISSN: 0300-9246.

P. Deplano, L. Pilia, D. Espa, M. L. Mercuri, A. Serpe, *Square-planar d<sup>8</sup> metal mixed-ligand dithiolene complexes as second order nonlinear optical chromophores: Structure/property relationship*. Coordination Chemistry Reviews, 254, 1434-1447, 2010. ISSN: 0010-8545.

*List of publications*

---

---

# Acknowledgement

Firstly, I wish to thank very much all the research group when I performed my PhD thesis. Thanks to my supervisor, Prof. Paola Deplano, for having proposed me this interesting subject and for her precious guide. Thanks to Prof. Maria Laura Mercuri, Dr. Angela Serpe, Prof. Emanuele Trogu and to Dr. Luca Pilia, Drs. Flavia Artizzu and Elisa Sessini for their constant support and the valuable advice.

I wish also to acknowledge Dr. Luciano Marchiò who performed the structural characterization and Prof. Santo Lanza for helpful suggesting to synthesize of suitable precursor such as  $[M(\text{DMSO})_2\text{Cl}_2]$ .

I would like to thank Dr. Neil Robertson for allowing me the opportunity to work with him at the University of Edinburgh. I would also like to thank Dr. Martina Congiu, Dr. Simon Dalgleish, Dr. Max Reinhardt for their help, and for making me feel so welcome during my stay in Edinburgh.

I am grateful to Dr. Alberto Barsella and Alain Fort who gave me the opportunity to spend a research stay to perform EFISH measurement in their lab at the CNRS of Strasbourg.

I would also like to thank Prof. Cristiana Mitsopoulou of the University of Athenes for the valuable collaboration and her tireless help with computational chemistry.

I am deeply grateful to my friends Luca, Flavia, Danilo, Francesca and Elisa for the detailed and constructive comments, and for their important support and guidance of great value in this study.

My deepest gratitude goes to my big family and Maria for their unflagging love and support throughout my life; this thesis would be simply impossible without them.